Large bandwidth excitation of Rydberg atoms in thermal vapor:

Fast dynamics and strong interaction effects

Von der Fakultät Mathematik und Physik der
Universität Stuttgart zur Erlangung der Würde eines
Doktors der Naturwissenschaften (Dr. rer. nat.)
genehmigte Abhandlung

vorgelegt von

Alban Urvoy

aus Saint-Brieuc (Frankreich)

Hauptberichter:	Prof. Dr. Tilman Pfau
Mitberichter:	Prof. Dr. Peter Michler
Prüfungsvorsitzender:	Prof. Dr. Maria Daghofer
Tag der mündlichen Prüfung:	22.04.2016

5. Physikalisches Institut
Universität Stuttgart

2016

Contents

Zusammenfassung

Mit der Formulierung der Theorie zur Quantenmechanik, begann man die Struktur der Materie auf der atomaren Skala zu verstehen. Die theoretische Beschreibung gilt für Systeme, die beliebig groß sind und beliebig viele Teilchen enthalten. Wenn Wechselwirkungsterme zwischen den Teilchen beachtet werden müssen, werden die internne und externen Freiheitsgrade miteinander gekoppelt. Dies hat zwar zur Folge, dass neue komplexe Phänomene vorkommen, wie zum Beispiel Supraflüssigkeit, Supraleitung [1], Quantenmagnetismus [2] oder die Physik der weichen Materie [3]. Solche Phänomene sind heutzutage von großem Interesse, da sie viele fundamentale und technische Perspektiven erlauben. Es sind aber Systeme, die noch nicht vollständig verstanden sind. Die Größe des Hilbert Raums wächst exponentiell mit der Anzahl an Teilchen, was die volle Berechnung vom System schon bei wenigen zehn Teilchen verbietet.

Der aktuelle elegante Umweg um diese Limitierung ist die Durchführung von Quantensimulationen. Das Prinzip von der Quantensimulation ist folgendes: mithilfe von einem experimentellen Aufbau - der von der Außenwelt isoliert ist, mehrere Teilchen enthält und deren Eigenschaften bekannt und einstellbar ist - kann man eine Emulation von einem Mehrteilchen-System durchführen. Die Entwicklung von Methoden und Technologien zur Kühlung von Atomen und Ionen ist über die letzten 40 Jahren so weit gekommen, dass jetzt in diesem Umfang Quantensimulationen möglich sind [4]. Zum Beispiel mit Ensemblen von ultrakalten Ionen kann jetzt Quantenmagnetismus simuliert werden [5], was letztendlich neue Erkenntnisse über Hochtemperatursupraleiter bringen könnte. Ein weiteres Beispiel sind Bose-Einstein Kondensate mit inter-atomaren Wechselwirkungen, die supraflüssige Eigenschaften zeigen [6, 7].

Für neutrale Atome, die kein permanentes Dipolmoment besitzen, erhält man die stärkstmögliche inter-atomare Wechselwirkung, wenn sich die Atome in einem sogenannten Rydberg Zustand befinden. Der Begriff "Rydberg Zustand" beschreibt Zustände, in denen ein (oder mehrere) Elektron hochangeregt ist (typischerweise $n \gtrsim 20$, wobei n die Hauptquantenzahl ist). Aufgrund der räumliche Trennung des Elektrons vom Innenteil des Atoms besitzen Rydberg Atome (Atome in einem Rydberg Zustand) ein großes elektrisches Dipolmoment und wechselwirken daher miteinander. Mithilfe dieser Wechselwirkung wurden in ultrakalten Ensembles Mehrteilchen-Dynamik und räumliche geordnete Strukturen [8] beobachtet. Neue experimentelle Methoden erlauben außerdem präzise Kontrolle von einzelnen Atomen, die die Realisierung von einem vielseitigen Quantensimulator ermöglichen könnten [9].

In den zuvor erwähnte Beispielen mit Rydberg Atomen ist entscheidend, dass die Atome in kohärenter Art und Weise manipuliert werden können. Auch im Gegenfall dazu, d.h. mit dominanter Dissipation, kann Mehrteilchen-Dynamik mit Rydberg Atomen

beobachtet werden. In diesem Fall verhält sich das Ensemble von Atomen üblicherweise wie klassische Spin-1/2 Teilchen. Es hat dazu geführt, dass ein Phasenübergang in einer Dampfzelle beobachtet werden konnte, zusammen mit superradianten Zerfällen von Rydberg Atomen (beide Prozesse sind grundsätlich Mehrteilchen Effekte). Außerdem wurde die Erzeugung von Aggregaten, die von großem Interesse im Gebiet der Physik der weichen Materie sind, demonstriert [10, 11]. Solche Aggregate sind Ensembles von Rydberg Atomen, die nur kurzweitige räumliche Ordnung besitzen. Die kurzweitige räumliche Ordnung sorgt für eine erhöhte Komplexität vom System [12].

Insgesamt können Rydberg Atome jetzt experimentell mit großer Genauigkeit manipuliert werden, und zeigen auch in Dampfzellen Mehrteilchen-Dynamik bei einer Temperatur über Raumtemperatur. Allerdings muss im Fall einer Dampfzelle der großen Geschwindigkeit thermischer Atome entgegengewirkt werden. Dies erfolgt durch eine Parameterauswahl die für schnelle Anregungsdynamik sorgt, sodass Dekohärenz durch die Bewegung der Atome minimiert wird [13]. Außerdem wird dadurch eine sehr schnelle Modulation von Zuständen erlaubt.

Im Rahmen dieser Arbeit wurden zwei unterschiedliche Experiment zur Untersuchung von der Anregung von Cäsium Atome zu Rydberg Zustände in einer Glas-Dampfzelle über Raumtemperatur ($T > 100\,^{\circ}\mathrm{C}$) aufgebaut. Der größte Vorteil von einer Dampfzelle ist, dass es ein viel kleineres System als eine Vakuumkammer für ultrakalte Atome. Außerdem sind sie kompatibel mit industriellen Methoden der Integration [14]. Trotz dem Einfluß von der Geschwindigkeit der Atome, wurden mehrere Meilensteine mit Rydberg Anregungen in Dampfzellen erreicht, wie die Möglichkeit der kohärente Anregung [13], die kohärente Emission von Licht durch einen Vierwellenmischen Prozess [15, 16], und der Auftritt der üblichen van-der-Waals Wechselwirkung zwischen Rydberg Atomen [17].

In den Experimenten die in dieser Arbeit beschrieben werden, wurden Rydberg Atome mithilfe eines Zweiphotonen-Schemas angeregt. Die Anregungsbandbreite ist vergleichbar mit frühere Experimenten mit kohärenter Anregung von Rydberg Atomen in Dampfzellen [13], sodass im Prinzip eine hohe Population im Rydberg Zustand erreicht werden kann. Die atomare Dichte ist auch im ersten Experiment so gewählt, dass die Wechselwirkung zwischen Rydberg Atomen signifikant hoch ist. Die hohe Bandbreite erlaubt im zweiten Experiment die Übertragung von einer Hochfrequenzmodulation (über 1 GHz) auf die Amplitude von einem transmittierten Lichtfeld.

Das erste Kapitel dieser Arbeit beschäftigt sich mit der theoretische Beschreibung von Rydberg Atomen. Zuerst werden die grundlegenden Eigenschaften von Rydberg Atomen wie die energetische Struktur oder die Dipolmomente erwähnt, sowie deren Skalierungsverhalten mit der Hauptquantenzahl. Der Einfluss von elektrischen Feldern auf Rydberg Zustände, der sogenannte Stark Effekt, wird dann vorgestellt. Am Ende wird der Formalismus der Wechselwirkung zwischen Rydberg Atomen beschreiben. Dies bezieht sich sowohl auf der Dipol-Dipol-Wechselwirkung, als auch auf höhere Ordnungen.

In einem Experiment mit einer Dampfzelle erfüllen die Lichtfelder einen doppelten Zweck: sie sorgen zum einen für die Anregung der Atome, zum anderen deren In-

tensität nach dem Durchgang durch die Zelle gemessen um die Information über die Anregung zu extrahieren. Deswegen ist die Wechselwirkung zwischen Licht und Atomen hier besonders wichtig. Der Formalismus dafür wird im Kapitel 2 detailliert beschrieben. Der Dichtematrix Formalismus für die Beschreibung der Zustände wird eingeführt, und die Wechselwirkung mit dem Lichtfeld durch die optische Bloch Gleichungen beschrieben.

Die endliche und große Geschwindigkeit der Atome führt zu inhomogene Verbreiterungsmechanismen [18], die prinzipiell nicht direkt mit dem Formalismus vom Kapitel 2 betrachtet werden können. Im Kapitel 3 werden die zwei Hauptkonsequenzen der atomare Bewegung vorgestellt, nämlich der Einfluss vom Doppler Effekt und der Einfluss der endlichen Durchflugszeit der Atome durch die Lichtfelder.

Kapitel 4 bezieht sich auf das erste Experiment, das im Zuge dieser Arbeit durchgeführt wurde. Hier sind Rydberg Atome bei einer hohen atomaren Dichte und mit hohen Verstimmungen und Rabi Frequenzen angeregt worden. Die Anregungsdynamik wurde durch einen schnellen Photodetektor zeitaufgelöst gemessen. Die experimentelle Ergebnisse haben ein Sättigungsverhalten in der Anzahl an Rydberg Atomen, die angeregt werden können, gezeigt. Zudem wurde eine Dichte-Abhängigkeit der Signalform festgestellt, die zusammen mit dem Sättigungsverhalten auf Mehrteilchen-Dynamik Effekte und Wechselwirkungseffekte. Insbesondere war die Betrachtung von Dipol-Quadrupol Wechselwirkungstermen entscheidend für das Verständnis der Daten. Eine charakteristische Zeitskala konnte aus den experimentellen Daten gewonnen werden. Diese Zeitskala war eine Funktion von folgenden Parametern im Experiment: die Verstimmung, die Rabi Frequenz, die atomare Dichte und die Hauptquantenzahl vom Rydberg Zustand. Die Abhängigkeiten an diesen Parametern konnten mittels Potenzgesetze angepasst werden. Die experimentelle Ergebnisse wurden mit einem Modell für die Aggregation von Rydberg Atomen verglichen [19, 20]. Die Grundidee von diesem Modell ist, dass wenn die Anregungslaser vom Rydberg Zustand verstimmt sind und Rydberg Atome miteinander stark wechselwirken, die Anregung zum Rydberg Zustand in der Nähe eines vorher angeregten Rydberg Atoms bei einem bestimmten Abstand resonant wird. Dieser Prozess wird als "fazilitierte" Anregung bezeichnet. Des weiteren entsteht eine räumliche Korrelation zwischen den Rydberg Anregungen, die ähnlich in der Physik der weiche Materie auftreten. Die resultierenden Ensembles von Rydberg Atomen, die räumliche Korrelationen zeigen, bilden sogenannte Aggregate von Rydberg Anregungen. Eine notwendige Bedingung für die Gültigkeit dieses Modell ist, dass die Anregung in einem stark dissipativen Regime stattfinden. Durch die atomare Bewegung und die resultierende Dekohärenz wird dies im Experiment erfüllt. Aus Simulationen mit dem theoretischen Modell bei den selben Parametern wie im Experiment wurde auch eine charakteristische Zeitskala extrahiert. Die absoluten Werte sowie die Potenzskalierungen von der Zeitskala mit den Parametern stimmt mit den Messungen überein. Diese Übereinstimmung ist besonders bemerkenswert, da es fundamentale Unterschiede zwischen dem Experiment und dem Modell gibt. Insbesondere wird im Modell ein gefrorenes Gas von Atomen angenommen, während im Experiment die atomare Bewegung sehr wichtig ist und der Grund für inhomogene Dekohärenz. Außerdem sind die Wechselwirkungspotentiale in der Tat deutlich Komplexer als die in dem Modell

angenommenen Potentiale. All dies ist ein starkes Zeichen dafür, dass die unterliegenden physikalischen Prozesse sehr robust sind. Sobald es ein Wechselwirkungspotential gibt, entsteht eine Resonanzbedingung die die "fazilitierte" Anregung erlaubt. Zudem wurde mit diesem Experiment gezeigt, dass kollektive Anregungsprozesse durch starke Wechselwirkungen auch in einer Dampfzelle möglich sind.

Das zweite Experiment wird im Kapitel 5 beschrieben. Hier handelt es sich um eine andere Art von Messung. Ein oszillierendes elektrischen Feld im Radiofrequenzbereich (RF, bei mehreren GHz) wirkt auf Rydberg Atome durch den Stark Effekt. Hintergrund von diesem Projekt ist eine fundamentale Fragestellung: was passiert wenn Rydberg Atome mit schnell oszillierenden Felder moduliert werden? Interessant ist aber auch eine technische Fragestellung: kann die RF-Modulation von Rydberg Atomen die Intensität von einem Lichtfeld effizient modulieren? Durch den Stark Effekt vom elektrischen Feld wird der Rydberg Zustand verschoben, und aufgrund von der Rückwirkung von Atomen auf die Intensität des anregenden Lichtfeldes wird diese Verschiebung als eine Modulation der Intensität vom Lichtfeld übertragen. Die zeitliche Entwicklung von dem System konnte simuliert werden. Mit einem Vergleich zu einer Floquet Theorie wurden die Ergebnisse der Simulation als Übergänge zwischen "RF-dressed" Zuständen identifiziert. Das Einsetzen vom oszillierenden elektrischen Feld erfolgt im Experiment über eine Platine, die mit Methoden der modernen Nachrichtentechnik entwickelt und hergestellt wurde. Insbesondere wurde darauf geachtet, dass die Schaltung kompatibel mit den hohen RF Frequenzen ist. Für die Detektion von der Amplitudenmodulation vom Lichtfeld wurde eine heterodyne Methode benutzt. Mithilfe eines zweiten Laserfeld wurde die Modulationsfrequenz zu einem Bereich konvertiert, in dem effiziente Photodetektoren benutzt werden konnten. Im Experiment wurde eine Modulation vom Lichtfeld bis zu einer Frequenz des elektrischen Felders von 3.6 GHz gemessen (d.h. 7.2 GHz auf dem Lichtfeld durch den quadratischen Stark Effekt). Dieser Wert kommt aus einer technischen Grenze. Es zeigte sich eine grobe qualitative Übereinstimmung zwischen theoretischen und experimentellen Ergebnissen. Die theoretisch erwartete Signal konnten in den experimentellen Ergebnissen erahnt werden, allerdings mit starken Verzerrungen. Dies deutet auf den möglichen Einfluss von Wechselwirkungseffekten hin, möglicherweise durch Ladungen in der Zelle. Außerdem war die Amplitude der Modulation mehrere Größenordnungen kleiner als von der Theorie vorhergesagt. Es konnten noch Verbesserungsvorschläge erarbeitet werden, unter anderen eine Verbesserung von der Platine, die zu homogeneren elektrischen Feldern führen könnte.

Insgesamt stellen diese zwei Experimente eine gute Basis für zukünftige zeitaufgelöste Experimente mit Rydberg Atome in Dampfzellen dar. Sowohl Mehrteilchen Dynamik aus dem Gleichgewicht [21], als auch schnellere Modulation vom Licht, möglicherweise durch eine Miniatisierung von der Dampfzelle und der Platine können in zukunft untersucht werden.

Introduction

The internal structure of matter at the atomic scale is very well described and understood since the formulation of quantum mechanics. For a system consisting of more than one atom, the internal degrees of freedom of the atoms are coupled to the external degrees of freedom by inter-particle interactions. These interactions complexify the description of systems composed of several atoms. If the dominant energy scale in the system is given by the strength of the interaction these systems are referred to as strongly interacting and/or strongly correlated many-body systems. The study of strongly interacting many-body systems led to the discovery of many novel phenomena such as superfluidity, superconductivity [1], quantum magnetism [2] or soft matter physics [3]. However, understanding these systems is still challenging to date because the sizes of the Hilbert space required for the description of these systems are exceptionally large, causing substantial difficulties in the calculations. In particular, this is the case for the systems out-of-equilibrium, which show rich physics and will be a major theme of this thesis.

In the last 40 years the development of lasers and the experimental techniques associated with this invention have revolutionized the study of atoms and ions, allowing for a tremendous control of their interactions between the atoms/ions, but also with well engineered environment. Right now this methodology developed in the context of quantum degenerate gases is also expanded to molecular states. They are now essentially platforms isolated from the environment with coherent excitation and tunable interactions. This enables to emulate and study many-body physics [4] and making Feynman's dream of a quantum simulator come true.

There are several experimental techniques that allow for the controlled realization of many-body systems. One remarkable platform is an array of trapped ions, which hold the record number of 14 qubits for a quantum computer [22], enough to compute the factorization $15 = 3 \times 5$. The outstanding experimental single particle control, and by this over the whole ensemble, in these experiments has also allowed for the simulation of quantum magnetism [5]. As for atoms, since their first observation, Bose-Einstein condensates (BEC) have been the subject of a large number of studies. In particular for non-negligible interactions between the atoms, the BEC show a superfluid behavior [6], and even shed light on the underlying principles of superfluidity [7].

The strongest possible interaction between neutral atoms (non dipolar) is the interaction between Rydberg atoms [23]. Atoms, in which at least one of the electrons is in a highly excited state ($n \gtrsim 20$, where n is the principal quantum number) are called Rydberg atoms, and they interact strongly because of the large electric dipole moment caused by the charge separation of the electronic cloud from the ionic core. In the

past decade there has been a large experimental effort to make use of this interaction for the creation of strongly interacting many-body systems. One consequence of the interaction between Rydberg atoms is the blockade effect [24], where the excitation of more than one Rydberg atom inside a certain volume is prohibited by the interaction potential. This can lead to the observation of spatially ordered structures in small ensembles [8], very much alike crystallization in solid-state systems. It should also result in a crystalline structure for larger systems [25]. Furthermore there have been significant results towards the use of systems of Rydberg atoms for quantum computation [23] and quantum simulation [26]. New techniques of single atom manipulation are now aiming at the same single particle control as in trapped ion systems, with a much larger flexibility in the geometry of the ensemble. These systems are promising candidates for the implementation of highly versatile quantum simulators [9].

Strongly interacting many-body excitation dynamics have also been studied with Rydberg atoms under the presence of strong dissipation, meaning that the system essentially behaves as an ensemble of classical spins. For instance, a nonequilibrium phase transition associated with superradiant collective fluorescence was observed for an ensemble of Rydberg atoms in a vapor cell [27]. A related effect is the emergence of aggregates, ensemble of Rydberg atoms which exhibit short-range order, was demonstrated in cold atomic clouds [10,11] and for the first time also in thermal vapor [28], as reported in this thesis . These results illustrate the potential of ensembles of Rydberg atoms to emulate soft-matter type collective systems [12], whose complexity arises from the spatial order being only present at short range.

All these examples illustrate the power and versatility of systems of Rydberg atoms due to their inter-atomic interactions. At the same time, the Rydberg atoms are very sensitive to the environment, especially to electric fields. This presents some experimental challenges, as the electric fields have to be very precisely under control. But it also offers opportunities such as tuning of inter-atomic (Förster) resonances [23], as a sensing tool for electric fields [29–31].

This thesis

In this thesis we present results of the excitation of Rydberg states in a vapor cell above room temperature (up to 200 °C). Despite the lack of control of the motional degrees of freedom of the atoms in a thermal gas above room temperature, several important results have previously been achieved, motivating the study of Rydberg atoms in such an environment. Vapor cells are small compared to cold atom experiments, they can be miniaturized [14] and they sustain coherent excitation to Rydberg states [32]. It was also demonstrated that light can be coherently emitted from an ensemble of Rydberg atoms via four-wave mixing [15, 16], which, combined with the observation of van-der-Waals interaction [17], paves the way towards a Rydberg-based single-photon source in a vapor cell.Finally, as mentioned before, many-body interaction effects and superradiance were observed in a vapor cell [27].

In the following thesis, we present results on the excitation of cesium atoms to Rydberg states in a very different parameter range than in previous work, and including methodological and fundamental differences. In a first experiment the atomic densities and the dephasing rates are up to 2 orders of magnitude larger than in previous work [10, 11], and the dominant dephasing mechanism is complex and based on the atomic motion. In a second experiment we have applied an oscillating electric field at frequencies of several GHz, off-resonant with atomic transitions in contrast to previous work of this kind [29–31]. Furthermore we focus on a the time-resolved observation in contrast to the detection of an average signal.

This thesis is organized as follows.

First, in chapter 1 we present the properties of Rydberg atoms that are relevant for the experiments presented in this thesis. We describe the general properties of Rydberg atoms and their scaling with principal quantum number. Then we discuss the interaction of Rydberg atoms with their environment: the effect of an external electric field on Rydberg states is examined, followed by the different aspects of the interaction between Rydberg atoms. Chapter 2 is devoted to the theoretical basics of the interaction between atoms and light fields and to the formalism that will be used in the rest of the thesis. In chapter 3 an implementation of the atomic motion into the theoretical model is discussed.

As for the experimental part, chapter 4 is dedicated to the measurement of the strongly correlated excitation of Rydberg aggregates. We present the excitation dynamics of Rydberg atoms in a vapor cell at large atomic densities. The analysis of the measured signal reveals many-body dynamics that rely on complex inter-atomic interactions. The scaling properties of the experimental data against all accessible experimental parameters is evaluated, and compared to simulation results from a theoretical model for Rydberg aggregation. In chapter 5 the experimental realization of the modulation of a light field amplitude is detailed. We first examine in a theoretical model the interplay between an oscillating electric field and the excitation of atoms to a Rydberg state. Then we present the setup used to generate a fast electric field modulation of Rydberg states. Finally, we examine the experimental results, with the focus on the maximum frequency at which the amplitude of a light field can be modulated using this scheme.

A brief of the results and a discussion of future prospects for both experiments are given at the end of the thesis.

Part I

Theoretical Concepts and Conventions

1 Rydberg Atoms

An atom is considered a "Rydberg atom" when one or several of its electrons are excited to a state with a high principal quantum number n (typ. $n \gtrsim 15$). The excited atom is then in a "Rydberg state". A consequence of such a high lying state is that the excited electron is weakly bound and its wavefunction is strongly delocalized from the cloud of the remaining core of electrons. This gives rise to exaggerated properties [23,33], which mostly has an impact as an extreme sensitivity to the electromagnetic environment, such as DC and AC external fields or the almost free electron of another Rydberg atom. Hence numerous applications of Rydberg atoms in current research arise, spanning from quantum optics [23] to many-body interacting systems [26] or precision sensing [29]. Although these properties of Rydberg states are very general, we will here restrict ourselves to the case of alkali atoms, i.e. atoms with only one valence electron which is then in the highly excited state, and in the course of this thesis only show data corresponding to cesium atoms.

To start with this chapter summarizes the properties of Rydberg atoms that are relevant for the work presented in this thesis. First we detail some general properties of single Rydberg atoms. Then we briefly address Rydberg atoms in an electric field. Finally we describe in more detail the interaction between Rydberg atoms.

1.1 General Properties

As discovered by Johannes Rydberg, the energies the Hydrogen levels from the ionization limit follow a simple formula: $-\mathrm{R}_\infty/(n^2(1+m_\mathrm{e}/m_\mathrm{p}))$, where R_∞ is the Rydberg constant, m_e is the electron mass, m_p is the proton mass, and n is the principal quantum number [33].

Because the spatial probability distribution of the electron of a Rydberg atom is strongly delocalized from the inner core (a ground state Cs^+ ion in the case of cesium), the atomic nucleus of charge $+Z$ is shielded by the $Z-1$ inner electrons. Thus the Rydberg electron essentially sees the core ion as a point charge and the level structure is in many aspects hydrogen-like. At a closer look this is not exactly true for S, P, D and F states, i.e. states of azimuthal quantum number $L < 4$. For these states the wavefunction of the electron still 'leaks' into the ionic core, partly experiencing the Coulomb potential of the atomic nucleus of charge Z. The shielding is not complete anymore and the degeneracy over the azimuthal quantum number is lifted. It was

property	**scaling**	**typ. value** ($32S_{1/2}$)
binding energy	$(n^*)^{-2}$	17.4 meV
level spacing	$(n^*)^{-3}$	296 GHz
orbital radius	$(n^*)^2$	$781\,a_0$
dipole moment $\langle R_{7P}\|er\|R_{nS}\rangle$	$(n^*)^{-3/2}$	$0.062\,ea_0$
dipole moment $\langle R_{nS}\|er\|R_{nP}\rangle$	$(n^*)^2$	$904\,ea_0$
polarizability	$(n^*)^7$	$-2.06\,\mathrm{MHz/(V/cm)^2}$
C_3 coefficient (for one nS and one nP atom)	$(n^*)^4$	$792\,\mathrm{MHz}\cdot\mu\mathrm{m}^3$
C_6 coefficient	$(n^*)^{11}$	$36\,\mathrm{MHz}\cdot\mu\mathrm{m}^6$

Table 1.1: Scaling laws for important properties of Rydberg atoms [23,33]. The typical values are given for the 32S state of Cs and were obtained using Ref. [34] and the database of our institute (similar to [35]). Note that the dipole moments here are the purely radial part of the dipole matrix element. Moreover there is a significant error bar associated with $\langle R_{7P}|er|R_{nS}\rangle$, as the dipole matrix elements including the 7P states typically involve strong relativistic effects [36]. More details on properties of Rydberg atoms can be found in [37].

empirically determined by Johannes Rydberg that the S, P, D and F series of the alkali atoms follow the slightly modified Rydberg formula [37]:

$$\mathcal{E}_{nlj} = -\frac{\mathrm{R}_\infty}{(n^*)^2(1+m_\mathrm{e}/m_+)} \tag{1.1}$$

where m_+ is the mass of the nucleus and $n^* = n - \delta_{nlj}$ has been introduced as the effective principal quantum number.[1]. δ_{nlj} is the quantum defect and follows the also empirically determined (modified) Rydberg-Ritz formula [34]:

$$\delta_{nlj} = \delta_0 + \frac{\delta_2}{(n-\delta_0)^2} + \frac{\delta_4}{(n-\delta_0)^4} + \dots \tag{1.2}$$

It is worth pointing out that the $(\delta_{2k})_{k\in\mathbb{N}}$ series is specific to each set of quantum numbers l and j. For instance for $S_{1/2}$ states [34],

$$\begin{aligned}\delta_0 &= 4.0493527\\ \delta_2 &= 0.238100\\ \delta_4 &= 0.24688\\ \delta_6 &= 0.06785\\ \delta_8 &= 0.1135\end{aligned} \tag{1.3}$$

Additionally to the energies of the Rydberg states, almost all properties of Rydberg atoms follow scaling laws versus the effective principal quantum number. Some of them, of relevance for this thesis, are shown in Table 1.1. Also shown in Table 1.1 are the values of these parameters for the $32S_{1/2}$ state of cesium.

[1]For simplification purposes, the hyperfine structure is neglected in this chapter. The notation for generic atomic states is $|nlj(m)\rangle$ with generic principal, azimuthal, total angular momentum and magnetic quantum numbers n, l, j and m respectively.

1.2 Stark effect

In the presence of an external electric field $\boldsymbol{E} = E\,\underline{\boldsymbol{\epsilon}}$, where $\underline{\boldsymbol{\epsilon}}$ is the unit polarization vector of the electric field, the Hamiltonian of the atom has the additional term

$$H_{\mathrm{E}} = -\hat{\boldsymbol{d}} \cdot \boldsymbol{E} = -E\hat{\boldsymbol{d}} \cdot \underline{\boldsymbol{\epsilon}} \tag{1.4}$$

where $\hat{\boldsymbol{d}} = e\,\hat{\boldsymbol{r}}$ is the electric dipole operator and $\hat{\boldsymbol{r}}$ the position operator of the electron. Diagonalization of the full Hamiltonian $H = H_0 + H_{\mathrm{E}}$, where H_0 is the unperturbed atomic Hamiltonian, yields new, shifted states. This effect is known as the Stark effect.

Quadratic Stark effect

Let us first consider the case of small electric fields, where the terms of H_{E} are smaller than the energy spacings between the atomic levels. Then H_{E} can be treated as a small perturbation of the system. Moreover, in the basis of the bare atomic states $|nljm\rangle$ (defined with $\underline{\boldsymbol{\epsilon}}$ as the quantization axis), H_{E} does not have diagonal terms, as $\langle nljm|\hat{\boldsymbol{d}} \cdot \underline{\boldsymbol{\epsilon}}|nljm\rangle = 0$ because of the dipole selection rules. Therefore one can use second order perturbation theory (for $L < 4$), and the energy shift has to be quadratic in E:

$$\mathcal{E}^{(2)}_{nljm} = e^2E^2 \sum_{n'l'j'm' \neq nljm} \frac{\left|\langle nljm|\hat{\boldsymbol{d}} \cdot \underline{\boldsymbol{\epsilon}}|n'l'j'm'\rangle\right|^2}{\mathcal{E}_{nlm} - \mathcal{E}_{n'l'j'm'}} \tag{1.5}$$

$$= \frac{1}{2}\alpha_{nljm}E^2 \tag{1.6}$$

where the polarizability α_{nljm} is given by

$$\alpha_{nljm} = 2e^2 \sum_{n'l'j'm' \neq nljm} \frac{\left|\langle nljm|\hat{\boldsymbol{d}} \cdot \underline{\boldsymbol{\epsilon}}|n'l'j'm'\rangle\right|^2}{\mathcal{E}_{nlm} - \mathcal{E}_{n'l'j'm'}} \tag{1.7}$$

Note that the quadratic Stark effect only applies to states with $L < 4$. The states of higher azimuthal quantum numbers are degenerated, and their Stark shift is linear with the electric field, as can be seen in Figure 1.1.

Stark map

For large enough fields the perturbation theory cannot be used and a full diagonalization of the Hamiltonian H has to be performed. In practice, full diagonalization means that enough states have to be included in the calculation, typically several hundreds. The results of such a calculation are typically presented in a so-called Stark map. Such a Stark map for Cesium is shown in Figure 1.1. It is interesting to note in Figure 1.1 that the Stark shift of the 32S state remains quadratic over the almost entire range of electric field shown here, despite numerous crossings with manifold lines.

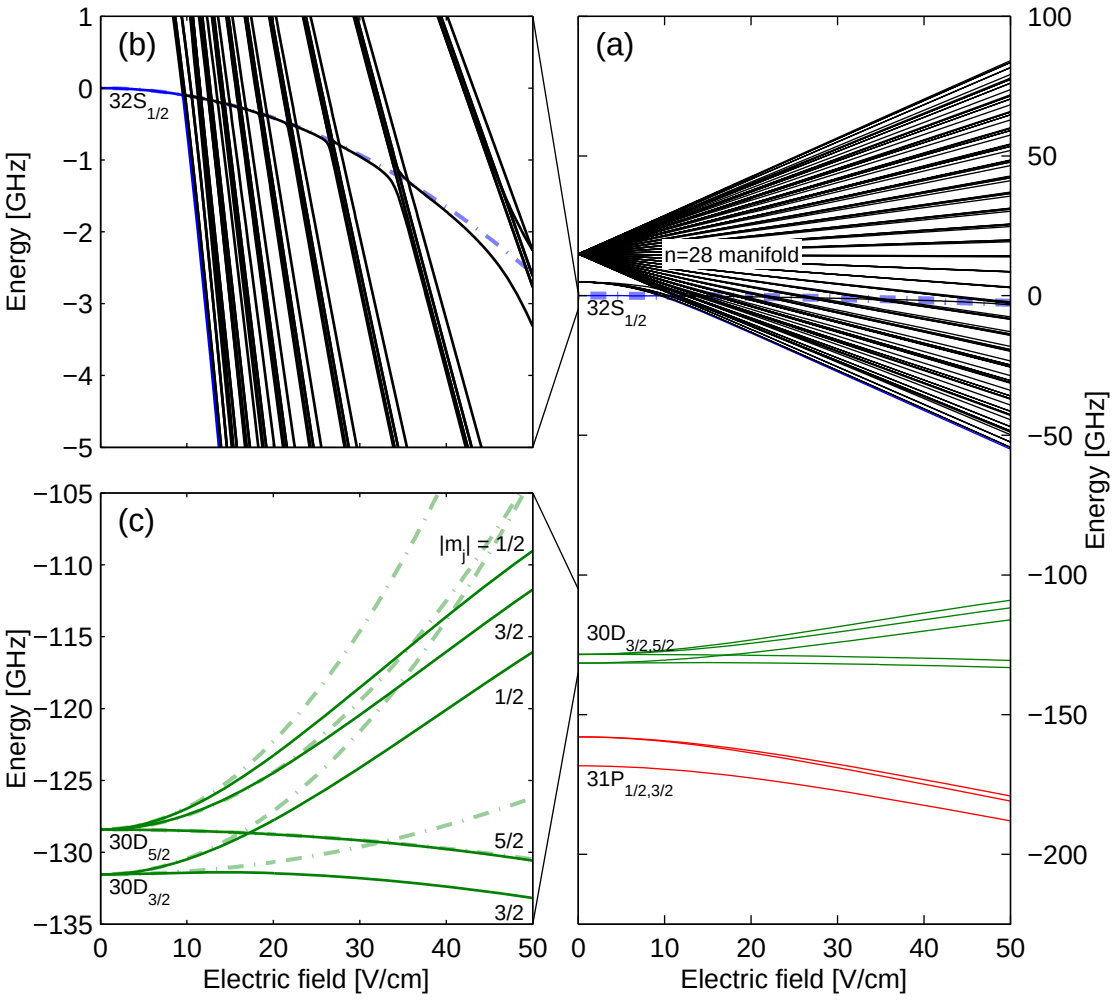

Figure 1.1: Stark map for Cs around the 32S state obtained by full diagonalization of the Hamiltonian $H = H_0 + H_E$ (with 484 states). The method used here to compute this Stark map is similar to the one described in [35]. In (a) we show the dependence on the electric field of all the nearest L-states (solid lines). The domains around the S and D state are zoomed in in (b) and (c) respectively. The solid lines represent the exact dependence on the electric field. The dash-dotted lines are the extrapolation of the low-field quadratic Stark effect from perturbation theory (following equation (1.6)) to the whole range of electric fields.

1.3 Interactions between Rydberg atoms

The interaction between Rydberg atoms is usually reduced to a binary interaction, i.e. the interaction between two Rydberg atoms. Note that Rydberg atoms are typically treated quantum mechanically as hydrogen-like systems consisting of an ionic core and an electron. The radial part of the Hamiltonian for one Rydberg atom consists of a Coulombic term $\propto 1/r$ and a centrifugal term $\propto 1/r^2$ [37], r being the norm of the position operator $\hat{\boldsymbol{r}} = r \times \underline{\boldsymbol{r}}$ of the electron, and $\underline{\boldsymbol{r}}$ is the corresponding unit vector. In Figure 1.2 we show schematically a system of two Rydberg atoms 1 and 2 composed of one ionic core and one electron in a Rydberg state. The two atoms are separated by a distance R. If we want to describe this system of the two atoms (with single atoms Hamiltonians H_1 and H_2) one has to add to the unperturbed pair state Hamiltonian $H_1 \otimes H_2$ an interaction potential of the form

$$\hat{V}_{\text{int}} = \frac{e^2}{4\pi\epsilon_0}\left(\frac{1}{R} + \frac{1}{R'} - \frac{1}{r_{12}} - \frac{1}{r_{21}}\right) \tag{1.8}$$

This interaction term consists of the Coulomb interaction between the ionic cores and electrons of the different atoms. Here R, R', r_{12} and r_{21} are the norms of the position operators between the different electrons and ionic cores as defined in Figure 1.2. At large interatomic distance R (1.8) can be rewritten as

$$\hat{V}_{\text{int}} = \frac{e^2}{4\pi\epsilon_0}\sum_{L_1,L_2=1}^{\infty}\sum_{M=-L_<}^{L_<}\frac{f_{L_1,L_2,M}}{R^{L_1+L_2+1}}\hat{Q}_{L_1,M}(\hat{\boldsymbol{r}}_1)\hat{Q}_{L_2,-M}(\hat{\boldsymbol{r}}_2) \tag{1.9}$$

where $\hat{Q}_{L,M}(\hat{\boldsymbol{r}})$ is the multipole operator for each atom, defined with regard to the spherical harmonics $Y_{L,M}$ as

$$\hat{Q}_{L,M}(\hat{\boldsymbol{r}}) = \left(\frac{4\pi}{2L+1}\right)^{1/2} r^L\, Y_{L,M}(\underline{\boldsymbol{r}}) \tag{1.10}$$

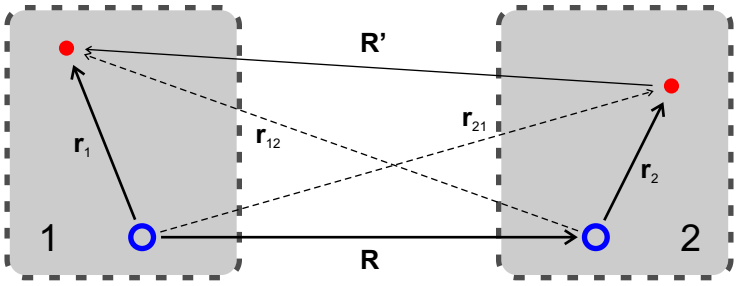

Figure 1.2: Schematic representation of a system of two Rydberg atoms 1 and 2 (from [38]). Red dots represent the electrons in Rydberg states and blue circles represent the ionic cores.

and where

$$f_{L_1,L_2,M} = \frac{(-1)^{L_2}(L_1+L_2)!}{[(L_1+M)!(L_1-M)!(L_2+M)!(L_2-M)!]^{1/2}} \quad \text{and } L_< = \min(L_1, L_2)$$

The L in (1.10) defines the order of the multipole operator. For instance $\hat{Q}_{1,M}$ are dipole operators. This is confirmed by the spherical harmonics $Y_{1,M}$ which are exactly the angular dependence of the classical dipole pattern. $\hat{Q}_{0,0}$ is the monopole operator (absent here because the atoms are neutral), $\hat{Q}_{2,M}$ are the quadrupole operators, $\hat{Q}_{3,M}$ the octopole operators, etc.

The multipole expansion (1.9) can be understood as the Taylor expansion of $\frac{1}{R'}$, $\frac{1}{r_{12}}$ and $\frac{1}{r_{21}}$ in powers of $\frac{1}{R}$ and $\hat{\boldsymbol{r}}$. More formally, this expansion is valid if the electronic wavefunctions of the two atoms do not overlap, such that exchange and overlap interactions are negligible [39]. In other words the interaction energy is treated as a perturbation on the system of the two individual Rydberg atoms. This condition is met if R is larger than the LeRoy-radius R_{LR} [40]:

$$R_{\mathrm{LR}} = 2\left(\langle n_1 l_1 j_1 m_1|\hat{\boldsymbol{r}}_1^2|n_1 l_1 j_1 m_1\rangle^{1/2} + \langle n_2 l_2 j_2 m_2|\hat{\boldsymbol{r}}_1^2|n_2 l_2 j_2 m_2\rangle^{1/2}\right) \tag{1.11}$$

where $\langle n_1 l_1 j_1 m_1|\hat{\boldsymbol{r}}_1^2|n_1 l_1 j_1 m_1\rangle^{1/2}$ is the standard deviation of the position operator $\hat{\boldsymbol{r}}_1$ for atom 1 (resp. 2). It is therefore a measure of the size of the Rydberg electron wavefunction. Note also that at large R, the aforementioned centrifugal interaction terms between the two atoms ($\propto 1/R^2$) are negligible with regard to the Coulomb terms. Thus spin-orbit (and also spin-spin) interactions between the two atoms are also neglected.

A full diagonalization of the pair state Hamiltonian with interactions $H^{(2)} = H_1 \otimes H_2 + \hat{V}_{\mathrm{int}}$ over the basis of pair states $|n_1 l_1 j_1 m_1, n_2 l_2 j_2 m_2\rangle$ yields new, shifted eigenstates. The result of such a diagonalization is shown in Figure 1.3. The projection of each eigenstate $|\Psi\rangle$ onto the unperturbed pair states yields the admixture of the unperturbed pair states

$$\varepsilon^{|\Psi\rangle}_{n_1 l_1 j_1 m_1, n_2 l_2 j_2 m_2} = \langle .n_1 l_1 j_1 m_1, n_2 l_2 j_2 m_2|\Psi\rangle \tag{1.12}$$

Dipole-dipole interaction

The expansion nature of (1.9) implies that a truncation is often possible, provided that the interatomic distance R is large enough. Such a truncation allows to gain insight in the physical meaning of the different terms. We focus here on first term in (1.9), which is due to dipole-dipole coupling between the two atoms. It can be rewritten in the usual form of dipole-dipole interaction [38]:

$$\hat{V}_{\mathrm{dd}} = \frac{\hat{\boldsymbol{d}}_1 \cdot \hat{\boldsymbol{d}}_2 - 3(\hat{\boldsymbol{d}}_1 \cdot \underline{\boldsymbol{R}})(\hat{\boldsymbol{d}}_2 \cdot \underline{\boldsymbol{R}})}{4\pi\epsilon_0 R^3} \tag{1.13}$$

where $\hat{\boldsymbol{d}} = e\hat{\boldsymbol{r}}$ are the respective dipole operators.

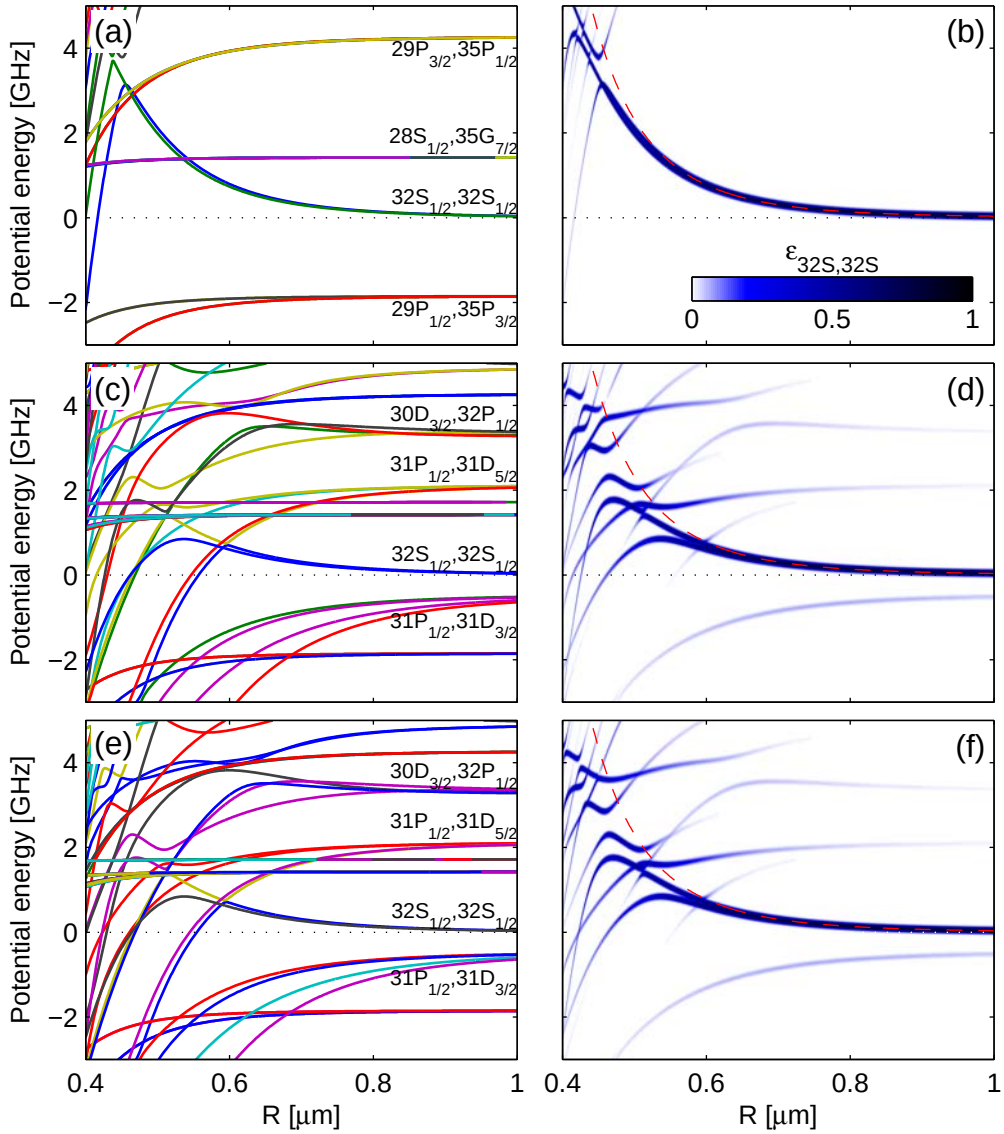

Figure 1.3: Sequence of pair state potentials and state mixing around the 32S,32S pair state ($m_j = 1/2$ and $-1/2$) against the interatomic distance R, including interaction terms up to dipole-dipole, dipole-quadrupole and quadrupole-quadrupole interaction (top to bottom). (a)-(c)-(e) show the pair state potentials lines of the relevant pair states around the 32S,32S pair state (eigenvalues of $H^{(2)}$). (b)-(d)-(f) are density plots showing the projection ($\varepsilon_{32S,32S}$, see definition in the text) of the shifted states (eigenvectors of $H^{(2)}$) onto the unperturbed 32S-32S pair state. Also shown here is the van-der-Waals potential $U^{\mathrm{vdW}}_{32S,32S}$ (1.14) from [39] (dashed red line). (a)-(b) are computed using only dipole-dipole interaction ($H^{(2)}_{\mathrm{dd}}$ is diagonalized). In (c)-(d) the next order (dipole-quadrupole) is added to $\hat{V}_{\mathrm{int}}$. Finally (e)-(f) include quadrupole-quadrupole interaction. Note that dipole-octopole interaction has the same order but couldn't be included. As can be seen in the figure, this term is anyways negligible in this range, which is the relevant one for this thesis. The computation method used here is similar to the one described in [35].

The pair state Hamiltonian with dipole-dipole interactions is $H_{\mathrm{dd}}^{(2)} = H_1 \otimes H_2 + \hat{V}_{\mathrm{dd}}$. In the basis of pair states $|n_1 l_1 j_1 m_1, n_2 l_2 j_2 m_2\rangle$, $\hat{V}_{\mathrm{dd}}$ is an off-diagonal operator because of dipole selection rules. Let us first consider the case where the terms of $\hat{V}_{\mathrm{dd}}$ are smaller than the energy spacings between pair states. Then, as in Section 1.2, we can determine the energy shift on the pair states using second order perturbation theory.

$$U^{\mathrm{vdW}}_{n_1 l_1 j_1 m_1, n_2 l_2 j_2 m_2} = \sum_{\substack{n_1' l_1' j_1' m_1' \neq n_1 l_1 j_1 m_1 \\ n_2' l_2' j_2' m_2' \neq n_2 l_2 j_2 m_2}} \frac{\left| \langle n_1 l_1 j_1 m_1, n_2 l_2 j_2 m_2 | \hat{V}_{\mathrm{dd}} | n_1' l_1' j_1' m_1', n_2' l_2' j_2' m_2' \rangle \right|^2}{\mathcal{E}_{n_1 l_1 j_1 m_1} + \mathcal{E}_{n_2 l_2 j_2 m_2} - \mathcal{E}_{n_1' l_1' j_1' m_1'} - \mathcal{E}_{n_2' l_2' j_2' m_2'}} \tag{1.14}$$

which can be rewritten using (1.13) to clearly show the van-der-Waals character of this perturbative interaction:

$$U^{\mathrm{vdW}}_{n_1 l_1 j_1 m_1, n_2 l_2 j_2 m_2} = \frac{C_6}{R^6} \tag{1.15}$$

The C_6 coefficient is usually not isotropic because the electronic wavefunctions are not rotationally symmetric (except for S states) [41]. The various angles relative to the quantization axis determine the angular dependence of the C_6 coefficient, such as the angle of the interatomic axis and the "atomic orientation" through the azimuthal and magnetic quantum numbers l and m. The values for the C_6 coefficients for S, P and D states, calculated in a basis of molecular states, can be found in [39]. The van-der-Waals potential for the 32S,32S pair state is shown in Figure 1.3 (b). There the perturbative character of the van-der-Waals interaction potential becomes clear, since at small interatomic distance R the deviation from the full diagonalization is visible.

If the interaction energy $\langle n_1 l_1 j_1 m_1, n_2 l_2 j_2 m_2 | \hat{V}_{\mathrm{dd}} | n_1' l_1' j_1' m_1', n_2' l_2' j_2' m_2' \rangle$ between two pair states is larger than the energy spacing between these two pair states, then the previous treatment is not valid anymore and the new pair states become strongly mixed and separated by

$$U^{\mathrm{dd}}_{n_1 l_1 j_1 m_1, n_2 l_2 j_2 m_2} = \langle n_1 l_1 j_1 m_1, n_2 l_2 j_2 m_2 | \hat{V}_{\mathrm{dd}} | n_1' l_1' j_1' m_1', n_2' l_2' j_2' m_2' \rangle = \frac{C_3}{R^3} \tag{1.16}$$

As for the C_6 coefficient, the C_3 coefficient is not isotropic. Moreover it is crucial that C_3 does not have a constant sign over space, like any dipole-dipole coupled system. Otherwise the integrated interaction energy over space would diverge.

Higher order terms

The restriction of binary interaction between Rydberg atoms to dipole-dipole interaction $\hat{V}_{\mathrm{dd}}$ is in most experiments so far satisfying. The excitation linewidths are typically small compared to the interaction potentials and level spacings, and thus the typical interatomic distances are large enough to neglect higher order terms in (1.9). This has been experimentally demonstrated in the group of Antoine Browaeys [42, 43] and made use of in numerous works based on Rydberg blockade [23] or spatially correlated excitation [19] among others. In some cases however it has been critical to

include dipole-quadrupole [44] and even quadrupole-quadrupole [45] terms. This has been especially true for cesium atoms. The quantum defects in cesium are very close to integers ($\delta_{n\mathrm{S}} \approx 4.05$) or half-integer ($\delta_{n\mathrm{P}} \approx 3.5$, $\delta_{n\mathrm{P}} \approx 2.5$) and thus lots of pair-states are bunched together. For instance in Ref. [44] the $23\mathrm{P}_{3/2}$,$23\mathrm{P}_{3/2}$ pair state lies very close to both the $23\mathrm{S}_{1/2}$,$18\mathrm{F}_J$ and $22\mathrm{S}_{1/2}$,$19\mathrm{F}_J$ pair states, with which significant dipole-quadrupole interaction is observed.

In this thesis, as detailed in chapter 4, we excite cesium atoms to S states. As shown in Figure 1.3(c) for the 32S,32S pair state, the 31P,31D and 32P,30D pair states are very close in energy to the 32S,32S pair state, and are coupled by dipole-quadrupole interaction with strong dipole and quadrupole moments (because the principal quantum numbers are very close). The influence of these states is clearly visible in Figure 1.3(c)-(d), where the dipole-quadrupole interaction term is included in $H^{(2)}$, compared to Figure 1.3(a)-(b), where only dipole-dipole interaction is taken into account. Also one can notice in Figure 1.3(e)-(f) that the higher order terms like quadrupole-quadrupole interaction have negligible contributions in this range of parameters.

For a pair state $|n_1 l_1 j_1 m_1, n_2 l_2 j_2 m_2\rangle$ the electronic parity is defined as $(-1)^{l_1+l_2}$ [44]. Pairwise interaction between two pair states usually conserve the electronic parity (cf. dipole-dipole or quadrupole-quadrupole interaction). This condition is violated for dipole-quadrupole interaction. The total parity of the system should actually be conserved by any interaction between two pair states. Therefore the rotational parity has to be also violated such that the total parity (product of electronic and rotational parities) is conserved. In practice this means that the rotational angular momentum L also changes. As demonstrated in [44] pair state interaction actually occurs during a collision between two atoms with impact parameter b, relative velocity v and reduced mass μ. The maximum rotational angular momentum is $\hbar L_{\max} = \mu b v$ and the energy splitting between two neighboring rotational states with angular momenta $L-1$ and L reads $\Delta E_{\mathrm{rot}} = L\hbar^2/(\mu b^2)$. Thus the maximum energy splitting between neighboring states is $\Delta E_{\mathrm{rot,max}} = \hbar v/b$. If this maximum rotational energy splitting is smaller than the experimental linewidths, the rotational levels can be considered as degenerate and there is no further interaction term to take into account. In the present case, by setting $v \sim 200\,\mathrm{m.s^{-1}}$ (at around 400 K) and $b = 1\,\mu\mathrm{m}$, since the dipole-quadrupole interaction starts playing a role at this interatomic distance (see Figure 1.3(d)), one obtains $\Delta E_{\mathrm{rot,max}} \sim 2\pi \times 50\,\mathrm{MHz}$. Thus neighboring rotational states are degenerate with regard to the experimental linewidths (see chapter 4) and no rotational coupling needs to be considered.

2 Atom-Light Interaction

Due to the loose binding of the electron in a Rydberg atom, the overall energy required to excite an atom to a Rydberg state is on the order of the ionization energy of the ground state atom. For Alkali atoms, as considered in this thesis, this ionization energy corresponds to ultraviolet light, which is hard to produce in the lab. The simplest method to excite Alkali atoms to a Rydberg state in a controlled manner is therefore to use multi-photon transitions with wavelengths in the visible domain. In contrast to ultracold atoms, we observe the relevant physics by analyzing the transmission properties of a probe beam, which requires a careful analysis of the optical response of a gas driven by several laser fields. This chapter is devoted to describing the interaction of coherent light fields with an atom, in order to describe both the response of atoms to a light field and the back-action of these atoms on the light field. As the light fields used in the experiments are fairly intense, i.e. well above the single photon level, they can be treated as classical, such that the semi-classical description of atom-light interaction is well-suited to describe the physical phenomena at stake.

This chapter contains first the general formalism of atom-light interaction. Then we focus on the specific case of a three-level ladder system with two driving fields, which is of relevance for this thesis. The subject of atom-light interaction is extensively described in numerous textbooks [46, 47], as well as in several theses [48, 49] with a formalism identical to the one used here. Therefore we present here the main concepts only in a reduced manner, i.e. without the derivation which can be found in the aforementioned literature. Newer and more essential concepts will be introduced more in-depth.

2.1 General concepts

Density matrix

An isolated atom, with discrete electronic states with energies $\hbar\omega_i$, is described by the Hamiltonian H_0. This Hamiltonian has $\hbar\omega_i$ as its eigenvalues, and $|i\rangle$ as its eigenstates, and it can be expressed in the form

$$H_0 = \sum_i \hbar\omega_i |i\rangle\langle i| \tag{2.1}$$

In the semi-classical model the Hamiltonian accounting for the interaction of a light field with the atom is simply the potential energy of the atomic electric dipole in the

electric field of the light field $\boldsymbol{E}_{\mathrm{L}}$

$$H_{\mathrm{AL}} = -\hat{\boldsymbol{d}} \cdot \boldsymbol{E}_{\mathrm{L}} \tag{2.2}$$

where $\hat{\boldsymbol{d}} = e\,\hat{\boldsymbol{r}}$ is the electric dipole operator of the atom, as previously defined in chapter 1. The Hamiltonian for the atomic system in the light field is

$$H = H_0 + H_{\mathrm{AL}} \tag{2.3}$$

The usual and practical way of treating the problem is to consider the density matrix of the system ρ. The diagonal elements of the density matrix ρ_{ii} represent the population of state $|i\rangle$, and the off-diagonal elements ρ_{ij} are the coherence between states $|i\rangle$ and $|j\rangle$. The density matrix is Hermitian ($\rho^\dagger = \rho$), and verifies $\mathrm{tr}(\rho) = 0$ because the population is conserved and normalized. This approach has the advantage of being practical for treating ensembles of atoms, and allows to consider decoherence mechanisms. Without decoherence, the equation of motion of the density matrix is called the Von Neumann equation and is a direct derivation from the Schrödinger equation

$$\frac{\partial \rho}{\partial t} = -\frac{i}{\hbar}\,[H, \rho] \tag{2.4}$$

Homogeneous decoherence mechanisms

In a real environment atoms experience decoherence, additionally to the coherent evolution described by equation (2.4). We focus here only on homogeneous decoherence, meaning that the mechanisms are the same for every atom, independently of external properties. Homogeneous decoherence results from stochastic processes (typically vacuum fluctuations) and can be separated into two categories: the non-energy-conserving decoherence or decay, and the energy conserving one or dephasing. The new equation of motion for the density matrix including decoherence processes is called the Liouville-von Neumann equation [50] or master equation:

$$\frac{\partial \rho}{\partial t} = -\frac{i}{\hbar}\,[H, \rho] + \hat{L}(\rho) \tag{2.5}$$

where $\hat{L}(\rho)$ is called the Lindblad operator [51]. We can separate the Lindblad operator into two terms $\hat{L}(\rho) = \hat{L}_1(\rho) + \hat{L}_2(\rho)$, with $\hat{L}_1(\rho)$ accounting for decay processes and $\hat{L}_2(\rho)$ accounting for dephasing processes. The general expression for $\hat{L}_1(\rho)$ is [50]

$$\hat{L}_1(\rho) = \sum_{i,j} \Gamma_{ij} \left(\hat{C}_{ij} \rho \hat{C}_{ij}^\dagger - \frac{1}{2} \left(\hat{C}_{ij}^\dagger \hat{C}_{ij} \rho + \rho \hat{C}_{ij}^\dagger \hat{C}_{ij} \right) \right) \tag{2.6}$$

where Γ_{ij} is the decay rate from $|i\rangle$ to $|j\rangle$ and $\hat{C}_{ij} = |j\rangle\langle i| = \hat{C}_{ji}^\dagger$ is the corresponding transition operator. Equation (2.6) can be rewritten in the form

$$\begin{aligned} \hat{L}_1(\rho) = &\sum_{i,j} \left(\Gamma_{ji} \rho_{jj} - \Gamma_{ij} \rho_{ii} \right) |i\rangle\langle i| \\ &- \frac{1}{2} \sum_{i \neq j} \left(\sum_k \Gamma_{ik} + \Gamma_{jk} \right) \rho_{ij} |i\rangle\langle j| \end{aligned} \tag{2.7}$$

where the first summation describes the diagonal terms (population transfer) and the second summation describes accounts for the decay of the coherences.

For dephasing processes the Lindblad operator reads [50]

$$\begin{aligned}\hat{L}_2(\rho) &= -\frac{1}{2}\sum_{i\neq j}\gamma_{ij}\hat{C}_{ii}\rho\hat{C}_{jj} \\ &= -\frac{1}{2}\sum_{i\neq j}\gamma_{ij}\rho_{ij}|i\rangle\langle j|\end{aligned} \tag{2.8}$$

where $\gamma_{ij} = \gamma_{ji}$ is the dephasing rate on the transition between $|i\rangle$ and $|j\rangle$. Dephasing can for instance arise from relaxation of type T_2 such as spin dephasing, from elastic collisions, or from the modeling of phase or intensity modulation on driving light field. One special case is that of dephasing mechanisms acting on the states, such as elastic collisions. In this case the dephasing process is equivalent to a decay from one level to itself, and $\hat{L}_2(\rho)$ can be written in the same form as the decay Lindblad operator (2.6):

$$\hat{L}_2(\rho) = \sum_i \gamma_i \left(\hat{C}_{ii}\rho\hat{C}_{ii}^\dagger - \frac{1}{2}\left(\hat{C}_{ii}^\dagger\hat{C}_{ii}\rho + \rho\hat{C}_{ii}^\dagger\hat{C}_{ii}\right)\right) \tag{2.9}$$

where γ_i is the dephasing rate of state $|i\rangle$. If only dephasing mechanisms of this form are relevant, the full Lindblad operator $\hat{L}(\rho)$ takes the same form as (2.7), where the dephasing accounted for by the addition of the somewhat unphysical decay from a state to itself with a rate $\Gamma_{ii} = \gamma_i$.

Rotating wave approximation

The electric field for a plane wave propagating in z-direction can be written as

$$\boldsymbol{E}_{\mathrm{L}}(z,t) = E_{\mathrm{L}}(z,t)\underline{\boldsymbol{\epsilon}}_{\mathrm{L}} = \frac{1}{2}\left(E_{0\mathrm{L}}(z,t)e^{i(\omega_{\mathrm{L}}t-k_{\mathrm{L}}z)} + E_{0\mathrm{L}}(z,t)^* e^{-i(\omega_{\mathrm{L}}t-k_{\mathrm{L}}z)}\right)\underline{\boldsymbol{\epsilon}}_{\mathrm{L}} \tag{2.10}$$

where $\underline{\boldsymbol{\epsilon}}_{\mathrm{L}}$ is the unit vector of the polarization, ω_{L} is the angular frequency of the light and $k_{\mathrm{L}} = \omega_{\mathrm{L}}/c$ is the wave number. The amplitude $E_{0\mathrm{L}}$ may be time dependent, but its time evolution is assumed to be much slower than the frequency of the light field. The Hamiltonian accounting for the atom-light interaction thus reads

$$H_{\mathrm{AL}} = -\frac{\hat{\boldsymbol{d}}\cdot\underline{\boldsymbol{\epsilon}}_{\mathrm{L}}}{2}\left(E_{0\mathrm{L}}(z,t)e^{i(\omega_{\mathrm{L}}t-k_{\mathrm{L}}z)} + E_{0\mathrm{L}}(z,t)^* e^{-i(\omega_{\mathrm{L}}t-k_{\mathrm{L}}z)}\right) \tag{2.11}$$

This formulation has the inconvenience that the fast oscillating terms of the light field are present. The time scales of the oscillating terms of the light field are usually very different from those of the atomic dynamics. These time scales can be separated by treating the problem in a frame that is oscillating with the frequency of the light fields, called the rotating frame. The transformation is characterized by the unitary operator U. The general expression for U can be found in [49], and will be given later for the

case of a three-level system, and the atomic system is described in the rotating frame by the new density matrix

$$\tilde{\rho} = U^\dagger \rho U \tag{2.12}$$

Under this transformation, the von Neumann equation governs the evolution of $\tilde{\rho}$ with a new Hamiltonian defined as

$$\tilde{H} = U^\dagger \rho U - i\hbar U^\dagger \frac{\partial U}{\partial t} \tag{2.13}$$

The atom-light Hamiltonian in the rotating frame is given by

$$U^\dagger H_{\mathrm{AL}} U = -\frac{\hat{\boldsymbol{d}} \cdot \underline{\boldsymbol{\epsilon}}_{\mathrm{L}}}{2} \left(E_{0\mathrm{L}}(z,t) + E_{0\mathrm{L}}(z,t)^* e^{-2i(\omega_{\mathrm{L}} t - k_{\mathrm{L}} z)} \right) \tag{2.14}$$

The separation of time scales, known as the rotating wave approximation, is then performed by considering the interaction Hamiltonian averaged over one period of the electric field (denoted here as $\langle \cdot \rangle_{t|\omega_L}$):

$$\tilde{H}_{\mathrm{AL}} = \langle U^\dagger H_{\mathrm{AL}} U \rangle_{t|\omega_L} = -\frac{\hat{\boldsymbol{d}} \cdot \underline{\boldsymbol{\epsilon}}_{\mathrm{L}} E_{0\mathrm{L}}}{2} = \frac{\hbar\hat{\Omega}}{2} \tag{2.15}$$

where $\hbar\hat{\Omega} = \hat{\boldsymbol{d}} \cdot \underline{\boldsymbol{\epsilon}}_{\mathrm{L}} E_{0\mathrm{L}}$ is the Rabi frequency (operator) The Lindblad operator in the rotating frame keeps its form, i.e. it is simply given by $\hat{L}(\tilde{\rho})$. For simplification purposes, only one light field was considered here. The generalization to a larger number of light fields is straightforward and follows the same steps, and is presented explicitly in [49]. The system of equations given by the Liouville-von Neumann equation in the rotating frame with the simplified Hamiltonian $\tilde{H}_{\mathrm{AL}}$ is also known as the "optical Bloch equations".

Back action on the light field

A light field modifies an atomic system in a way governed by the Liouville-von Neumann equation (2.5). The typical processes are the excitation of the atom via the absorption of a photon from the light field, and the de-excitation of the atom via stimulated emission back into the light field. This means that there is a back-action from the atomic system onto the light field, and that the two are eventually coupled systems. We present here the main aspects of this back-action, which allows in the experiments presented here to measure the influence of light fields on the atomic system.

For simplification purposes, we focus here again on a single light field, and assume that it is far off-resonant for all but one transition between levels $|i\rangle$ and $|j\rangle$. The generalization is straightforward and can be found in [49]. In this case $\tilde{H}_{\mathrm{AL}}$ reduces to two terms:

$$\begin{aligned} (\tilde{H}_{\mathrm{AL}})_{ij} = (\tilde{H}_{\mathrm{AL}})^*_{ji} &= -\frac{d_{ij} E_{0\mathrm{L}}}{2} \\ &= \frac{\hbar\Omega_{ij}}{2} \end{aligned} \tag{2.16}$$

where $d_{ij} = \langle i|\hat{\boldsymbol{d}} \cdot \underline{\boldsymbol{\epsilon}}_{\mathrm{L}}|j\rangle$ is the dipole matrix element of the transition.

The light field propagates through the medium formed by the atoms. This medium has a polarization density $P = N\langle d\rangle$, where N is the atomic density and $\langle d\rangle$ is the expectation value of the atomic dipole moment. The polarization density can be rewritten as

$$\begin{aligned} P = N\langle d\rangle &= \mathrm{tr}(\rho \cdot (\hat{\boldsymbol{d}} \cdot \underline{\boldsymbol{\epsilon}}_{\mathrm{L}})) \\ &= \rho_{ij} d_{ji} + \rho_{ji} d_{ij} \\ &= \tilde{\rho}_{ij} d_{ji} e^{i(\omega_{\mathrm{L}} t - k_{\mathrm{L}} z)} + \tilde{\rho}_{ji} d_{ij} e^{-i(\omega_{\mathrm{L}} t - k_{\mathrm{L}} z)} \end{aligned} \tag{2.17}$$

where the usual transformation in the rotating frame U was used, such that the coherences of the density matrix transform as $(U^\dagger \rho U)_{ij} = \tilde{\rho}_{ij} = \rho_{ij} e^{-i(\omega_{\mathrm{L}} t - k_{\mathrm{L}} z)}$ [49].

The electric field is influenced by the polarization density of the medium, following the usual wave equation

$$\left(\frac{\partial^2}{\partial z^2} - \frac{1}{c^2}\frac{\partial^2}{\partial t^2}\right) E_{\mathrm{L}}(z,t) = \frac{1}{\epsilon_0 c^2}\frac{\partial^2}{\partial t^2} P(z,t) \tag{2.18}$$

The polarization density can be written in the form of a plane wave:

$$P(z,t) = \frac{1}{2}\left(P_0(z,t) e^{i(\omega_{\mathrm{L}} t - k_{\mathrm{L}} z)} + P_0(z,t)^* e^{-i(\omega_{\mathrm{L}} t - k_{\mathrm{L}} z)}\right) \tag{2.19}$$

It is practical to apply a transformation into a co-moving reference frame (ζ, τ), defined by $\zeta = z$ and $\tau = t - z/c$. Under the assumption that the envelopes $E_{0\mathrm{L}}(\zeta,\tau)$ and $P_0(\zeta,\tau)$ vary slowly with respect to the oscillating terms[1], equation (2.18) reduces to [48, 49]:

$$\frac{\partial}{\partial \zeta} E_{0\mathrm{L}}(\zeta,\tau) = -\frac{i\omega_{\mathrm{L}}}{2\epsilon_0 c} P_0(\zeta,\tau) \tag{2.20}$$

By combining (2.17), (2.19) and (2.20) one obtains the following equation, coupling the electric field and the density matrix:

$$\frac{\partial}{\partial \zeta} E_{0\mathrm{L}}(\zeta,\tau) = -i\frac{\omega_{\mathrm{L}} N d_{ji}}{\epsilon_0 c} \tilde{\rho}_{ij}(\zeta,\tau) \tag{2.21}$$

The interplay between the light field and the atomic system becomes clearer by rewriting (2.21) in terms of the Rabi frequency $\Omega_{ij} = -d_{ij} E_{0\mathrm{L}}/\hbar$:

$$\frac{\partial}{\partial \zeta} \Omega_{ij}(\zeta,\tau) = i\frac{\omega_{\mathrm{L}} N |d_{ij}|^2}{\hbar \epsilon_0 c} \tilde{\rho}_{ij}(\zeta,\tau) \tag{2.22}$$

For an ensemble of atoms extended in the propagation direction z of the light field, the system (atoms, light) is governed by the Liouville-von Neumann equation (2.5) for the time dependence and equation (2.21) for the spatial dependence. The measured

[1] Note that this assumption was already applied previously for the rotating wave approximation.

quantity in the experiments presented in this is the intensity of the light fields $I = (1/2)c\epsilon_0 E_{0\mathrm{L}} E_{0\mathrm{L}}^*$. The spatial differential equation for the intensity is

$$\begin{aligned}\frac{\partial}{\partial\zeta} I(\zeta,\tau) &= \frac{1}{2} c\epsilon_0 \left(E_{0\mathrm{L}} \frac{\partial E_{0\mathrm{L}}^*}{\partial\zeta} + E_{0\mathrm{L}}^* \frac{\partial E_{0\mathrm{L}}}{\partial\zeta} \right) \\ &= c\epsilon_0 \,\mathrm{Re}\left(E_{0\mathrm{L}}^* \frac{\partial E_{0\mathrm{L}}}{\partial\zeta} \right) \\ &= N\hbar\omega_{\mathrm{L}} \,\mathrm{Re}\left(i\Omega_{ij}(\zeta,\tau)^* \tilde{\rho}_{ij}(\zeta,\tau) \right) \quad \text{using (2.21)} \\ &= -N\hbar\omega_{\mathrm{L}} \,\mathrm{Im}\left(\Omega_{ij}(\zeta,\tau)^* \tilde{\rho}_{ij}(\zeta,\tau) \right) \end{aligned} \tag{2.23}$$

Let us now consider that the ensemble of atoms extends from $\zeta = 0$ to $\zeta = l$. The total change in intensity over the length of the medium is obtained by integrating (2.23) over ζ:

$$I(l,\tau) - I(0,\tau) = -N\hbar\omega_{\mathrm{L}} \int_0^l \mathrm{Im}\left(\Omega_{ij}(\zeta,\tau)^* \tilde{\rho}_{ij}(\zeta,\tau) \right) \mathrm{d}\zeta \tag{2.24}$$

Two boundary cases can be identified:

(i) the intensity varies only slightly along the cell, and

(ii) the steady state in the weak probe limit ($\Omega_{ij} \ll \Gamma$ and $\Omega_{ij}(\zeta,\tau) = \Omega_{ij}(\zeta)$) where the coherence term $\tilde{\rho}_{ij}$ is proportional to the Rabi frequency.

In the first case (i), when the intensity varies only slightly along the medium, this means that propagation effects can be neglected. Then the Rabi frequency and therefore the density matrix $\tilde{\rho}$ are independent of ζ, and the transformation into the original reference frame (t,z)is trivial. Without loss of generality, we can assume that the Rabi frequency is real and positive before interacting with the atoms (i.e. $\Omega_{ij}(\zeta = 0,\tau)$ is real), and equation (2.24) thus reduces to

$$\Delta I(t) = -N\hbar\omega_{\mathrm{L}} l \,\Omega_{ij}(t) \,\mathrm{Im}\left(\tilde{\rho}_{ij}(t) \right) \tag{2.25}$$

In (2.24) we can see that the change in intensity through the medium is essentially given by the imaginary part of the coherence $\tilde{\rho}_{ij}$. This is very practical because the density matrix can often be computed with a suitable theory, and (2.25) allows to compare the experimental and theoretical results directly.

In the second case (ii), i.e. when the Rabi frequency is small compared to the other relevant energy scales, the coherence is proportional to the Rabi frequency [46]

$$\tilde{\rho}_{ij} \propto \Omega_{ij} \tag{2.26}$$

Equation (2.24) then becomes

$$\begin{aligned}\frac{\partial}{\partial\zeta} I(\zeta) &\propto -|\Omega_{ij}(\zeta)|^2 \,\mathrm{Im}\left(\frac{\tilde{\rho}_{ij}(\zeta)}{\Omega_{ij}(\zeta)} \right) \\ &= -\alpha I(\zeta) \end{aligned} \tag{2.27}$$

where α is called the absorption coefficient, and contains the parameters of the atomic system. Note that $\alpha \propto \mathrm{Im}\left(\tilde{\rho}_{ij}(t)\right)$, such that here as well the change in intensity is essentially characterized by the imaginary part of the coherence $\tilde{\rho}_{ij}$. The integration over ζ of (2.27) yields the well-known Lambert-Beer formula

$$I(l) = I(0)\, e^{-\alpha l} \tag{2.28}$$

2.2 Three-level ladder system

In the majority of experiments involving Rydberg states of Alkali atoms, the excitation to the Rydberg state is performed with a two-photon excitation via an intermediate state. Such an excitation combines several advantages, among which the possibility to have light fields in the visible to near-infrared range and relatively large Rabi frequencies. The excitation dynamics of a three-level system remain fairly simple while offering rich new effects such as electromagnetically-induced transparency (EIT).

A typical representation of a three-level ladder system is shown in Figure 2.1. It consists of a ground state $|1\rangle$, an intermediate state $|2\rangle$ and an excited state $|3\rangle$. If we define the basis of the three states as

$$|1\rangle := \begin{pmatrix} 1 \\ 0 \\ 0 \end{pmatrix} \quad |2\rangle := \begin{pmatrix} 0 \\ 1 \\ 0 \end{pmatrix} \quad |3\rangle := \begin{pmatrix} 0 \\ 0 \\ 1 \end{pmatrix}$$

such that the system is described by the density matrix

$$\rho = \begin{pmatrix} \rho_{11} & \rho_{12} & \rho_{13} \\ \rho_{21} & \rho_{22} & \rho_{23} \\ \rho_{31} & \rho_{32} & \rho_{33} \end{pmatrix} \tag{2.29}$$

The transitions from $|1\rangle$ to $|2\rangle$ (also called the probe transition) and from $|2\rangle$ to $|3\rangle$ (also called the coupling transition) are respectively driven by two plane wave light fields with electric fields [2]

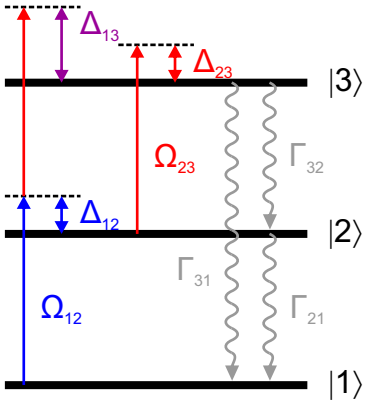

Figure 2.1: Schematic representation of a three-level ladder system

$$\begin{aligned} \boldsymbol{E}_{12}(t) &= E_{12}(t)\underline{\boldsymbol{\epsilon}}_{12} = \frac{1}{2}\left(E_{0,12}(t)e^{i\omega_{\mathrm{L},12}t} + \mathrm{c.c.}\right)\underline{\boldsymbol{\epsilon}}_{12} \\ \boldsymbol{E}_{23}(t) &= E_{23}(t)\underline{\boldsymbol{\epsilon}}_{23} = \frac{1}{2}\left(E_{0,23}(t)e^{i\omega_{\mathrm{L},23}t} + \mathrm{c.c.}\right)\underline{\boldsymbol{\epsilon}}_{23} \end{aligned} \tag{2.30}$$

[2] Without loss of generality, the spatial dependence of the electric field is dropped from here for convenience. Also the notations are slightly modified for this specific case.

The full Hamiltonian for this system is given by

$$\begin{aligned} H &= H_0 + H_{\mathrm{AL}} \\ &= \hbar \begin{pmatrix} \omega_1 & 0 & 0 \\ 0 & \omega_2 & 0 \\ 0 & 0 & \omega_3 \end{pmatrix} + \begin{pmatrix} 0 & -d_{12}E_{12}(t) & 0 \\ -d_{21}E_{12}(t) & 0 & -d_{23}E_{23}(t) \\ 0 & -d_{32}E_{23}(t) & 0 \end{pmatrix} \end{aligned} \tag{2.31}$$

where $d_{ij} = \langle i|\hat{\boldsymbol{d}} \cdot \underline{\boldsymbol{\epsilon}}_{ij}|j\rangle$ is the dipole matrix element of the transition from $|i\rangle$ to $|j\rangle$.

The transformation matrix into the rotating frame is

$$U = \begin{pmatrix} 1 & 0 & 0 \\ 0 & e^{-i\omega_{\mathrm{L},12}t} & 0 \\ 0 & 0 & e^{-i(\omega_{\mathrm{L},12}+\omega_{\mathrm{L},12})t} \end{pmatrix} \tag{2.32}$$

Note that the transformation is now applied with two driving light fields. When we apply an energy offset of $(-\hbar\omega_1)$ to the Hamiltonian, or in other words offset the energy of the ground state to 0, the Hamiltonian the rotating frame reads

$$\tilde{H} = \hbar \begin{pmatrix} 0 & \frac{1}{2}\Omega_{12} & 0 \\ \frac{1}{2}\Omega_{12}^* & -\Delta_{12} & \frac{1}{2}\Omega_{23} \\ 0 & \frac{1}{2}\Omega_{23}^* & -\Delta_{12}-\Delta_{23} \end{pmatrix} = \hbar \begin{pmatrix} 0 & \frac{1}{2}\Omega_{12} & 0 \\ \frac{1}{2}\Omega_{12}^* & -\Delta_{12} & \frac{1}{2}\Omega_{23} \\ 0 & \frac{1}{2}\Omega_{23}^* & -\Delta_{13} \end{pmatrix} \tag{2.33}$$

where $\Omega_{ij} = -d_{ij}E_{0,ij}/\hbar$ are the Rabi frequencies and $\Delta_{12} = \omega_{\mathrm{L},12} - (\omega_2 - \omega_1)$, $\Delta_{23} = \omega_{\mathrm{L},23} - (\omega_3 - \omega_2)$ and $\Delta_{13} = \Delta_{12} + \Delta_{23}$ are the detunings of the light fields with regard to the transition frequencies. Δ_{13} in particular is called the two-photon detuning and is the combined detuning of the two light fields to the excited state $|3\rangle$.

The decays from the intermediate and excited states are pictured in Figure 2.1. From equation (2.6) the Lindblad operator accounting for decay processes has the form

$$\hat{L}_1(\tilde{\rho}) = \begin{pmatrix} \Gamma_{21}\tilde{\rho}_{22} + \Gamma_{31}\tilde{\rho}_{33} & -\frac{1}{2}\Gamma_{21}\tilde{\rho}_{12} & -\frac{1}{2}\Gamma_{31}\tilde{\rho}_{13} \\ -\frac{1}{2}\Gamma_{21}\tilde{\rho}_{21} & -\Gamma_{21}\tilde{\rho}_{22} + \Gamma_{32}\tilde{\rho}_{33} & -\frac{1}{2}(\Gamma_{21}+\Gamma_{31}+\Gamma_{32})\tilde{\rho}_{23} \\ -\frac{1}{2}\Gamma_{31}\tilde{\rho}_{31} & -\frac{1}{2}(\Gamma_{21}+\Gamma_{32}+\Gamma_{31})\tilde{\rho}_{32} & -(\Gamma_{31}+\Gamma_{32})\tilde{\rho}_{33} \end{pmatrix} \tag{2.34}$$

whereas dephasing processes are accounted for by

$$\hat{L}_2(\tilde{\rho}) = \begin{pmatrix} 0 & -\frac{1}{2}\gamma_{12}\tilde{\rho}_{12} & -\frac{1}{2}\gamma_{13}\tilde{\rho}_{13} \\ -\frac{1}{2}\gamma_{21}\tilde{\rho}_{21} & 0 & -\frac{1}{2}\gamma_{23}\tilde{\rho}_{23} \\ -\frac{1}{2}\gamma_{31}\tilde{\rho}_{31} & -\frac{1}{2}\gamma_{32}\tilde{\rho}_{32} & 0 \end{pmatrix} \tag{2.35}$$

The Liouville-von Neumann equation for the three level ladder system can be rewritten

as the optical Bloch equations for the single entries of the density matrix:

$$\begin{aligned}
\frac{\partial}{\partial t}\tilde{\rho}_{11} &= \Gamma_{21}\tilde{\rho}_{22} + \Gamma_{31}\tilde{\rho}_{33} - \mathrm{Im}\left(\tilde{\rho}_{12}\Omega_{12}^{*}\right) \\
\frac{\partial}{\partial t}\tilde{\rho}_{12} &= \left(-\frac{\Gamma_{21}+\gamma_{12}}{2} - i\Delta_{12}\right)\tilde{\rho}_{12} + \frac{i}{2}\left(-\left(\tilde{\rho}_{22}-\tilde{\rho}_{11}\right)\Omega_{12} + \tilde{\rho}_{13}\Omega_{23}^{*}\right) \\
\frac{\partial}{\partial t}\tilde{\rho}_{13} &= \left(-\frac{\Gamma_{32}+\Gamma_{31}+\gamma_{13}}{2} - i\left(\Delta_{12}+\Delta_{23}\right)\right)\tilde{\rho}_{13} + \frac{i}{2}\left(\tilde{\rho}_{12}\Omega_{23} - \tilde{\rho}_{23}\Omega_{12}\right) \\
\frac{\partial}{\partial t}\tilde{\rho}_{22} &= -\Gamma_{21}\tilde{\rho}_{22} + \Gamma_{32}\tilde{\rho}_{33} + \mathrm{Im}\left(\tilde{\rho}_{12}\Omega_{12}^{*}\right) - \mathrm{Im}\left(\tilde{\rho}_{23}\Omega_{23}^{*}\right) \\
\frac{\partial}{\partial t}\tilde{\rho}_{23} &= \left(-\frac{\Gamma_{21}+\Gamma_{32}+\Gamma_{31}+\gamma_{23}}{2} - i\Delta_{23}\right)\tilde{\rho}_{23} + \frac{i}{2}\left(-\left(\tilde{\rho}_{33}-\tilde{\rho}_{22}\right)\Omega_{23} - \tilde{\rho}_{13}\Omega_{12}^{*}\right) \\
\frac{\partial}{\partial t}\tilde{\rho}_{33} &= -(\Gamma_{31}+\Gamma_{32})\tilde{\rho}_{33} + \mathrm{Im}\left(\tilde{\rho}_{23}\Omega_{23}^{*}\right)
\end{aligned} \tag{2.36}$$

Here we have made use of the Hermitian character of the density matrix ($\tilde{\rho}_{ij}^{*} = \tilde{\rho}_{ji}$).

2.3 Adiabatic elimination of the intermediate state

Despite having technical advantages, the excitation of atoms to Rydberg states via a three-level ladder system also present some challenges. First the presence of the intermediate state prevents from reaching the full population in the excited state. Second the Hilbert space of an ensemble of atoms is much bigger than for two-level systems. This becomes critical as the number of atoms gets larger, thus limiting the possibility to compute the response of the system. The usual way to circumvent this issue is to apply a detuning to the intermediate state that is large compared to the Rabi frequencies and the two-photon detuning ($|\Delta_{12}| \gg |\Delta_{13}|, |\Omega_{12}|, |\Omega_{23}|$). By doing so, the population of the intermediate state is neglected and the three-level ladder system can be reduced to an effective two-level system comprising only the ground state and the excited state.

For the derivation of the effective Hamiltonian $\tilde{H}_{\text{eff}}$ for this reduced system, we will follow [52], where it is carried out in the most general manner. Let us consider that the decays to and from the intermediate state are negligible (i.e. $\Gamma_{21} \approx 0$, $\Gamma_{32} \approx 0$), as well as any dephasing mechanism involving the intermediate state (i.e. Γ_{22})[3]. The Hamiltonian in the rotating frame contains one dominant energy scale $-\Delta_{12}$, the energy of the intermediate state. The approximation at the heart of the adiabatic elimination is to neglect the temporal evolution associated with this component of the Hamiltonian. Under this approximation, the evolution of the effective two-level system, described by the reduced density matrix $\tilde{\rho}_{\text{eff}} = \left(\begin{smallmatrix}\tilde{\rho}_{11} & \tilde{\rho}_{13} \\ \tilde{\rho}_{31} & \tilde{\rho}_{33}\end{smallmatrix}\right)$, is governed by the effective Hamiltonian

[3]This assumption is valid for the experiments presented in this thesis. If decay and dephasing mechanisms involving the intermediate state cannot be neglected, some correction terms appear in $\tilde{H}_{\text{eff}}$ and $\hat{L}_{\text{eff}}$ [52].

$\tilde{H}'_{\text{eff}}$

$$\tilde{H}'_{\text{eff}} = \hbar \begin{pmatrix} \frac{|\Omega_{12}|^2}{4\Delta_{12}} & \frac{1}{2}\Omega_{\text{eff}} \\ \frac{1}{2}\Omega^*_{\text{eff}} & -\Delta_{13} - \frac{|\Omega_{23}|^2}{4\Delta_{23}} \end{pmatrix}$$

where additional detuning terms account for the light shifts of the lasers on the ground and excited states, and

$$\Omega_{\text{eff}} = \frac{\Omega_{12}\Omega_{23}}{4\Delta_{12}} - \frac{\Omega_{12}\Omega_{23}}{4\Delta_{23}} \tag{2.37}$$

is the effective Rabi frequency. The Lindblad operator for the effective system is merely the reduction of the one for full system, which under the current assumptions reads

$$\hat{L}_{\text{eff}}(\tilde{\rho}_{\text{eff}}) = \begin{pmatrix} \Gamma_{31}\tilde{\rho}_{33} & -\frac{1}{2}(\Gamma_{31}+\Gamma_{33})\tilde{\rho}_{13} \\ -\frac{1}{2}(\Gamma_{31}+\Gamma_{33})\tilde{\rho}_{31} & -\Gamma_{31}\tilde{\rho}_{33} \end{pmatrix} \tag{2.38}$$

As detailed in [53–55], this usual adiabatic elimination presents a strong limitation, since it is not conserved under the addition of a small overall phase. In other words the effective Hamiltonian is dependent on the point of zero energy. This problem has been studied theoretically [53,55], however under the conditions relevant for the experiments presented here, the energy offset for the ground state $|\Omega_{12}|^2/(4\Delta_{12})$ is small enough to rewrite the effective Hamiltonian as

$$\tilde{H}_{\text{eff}} = \hbar \begin{pmatrix} 0 & \frac{1}{2}\Omega_{\text{eff}} \\ \frac{1}{2}\Omega^*_{\text{eff}} & -\Delta'_{13} \end{pmatrix} \tag{2.39}$$

where Δ'_{13} is the effective two-photon detuning defined as

$$\Delta'_{13} = \Delta_{13} + \frac{|\Omega_{23}|^2}{4\Delta_{23}} + \frac{|\Omega_{12}|^2}{4\Delta_{12}} \tag{2.40}$$

In the optical Bloch equations (2.36), the adiabatic elimination amounts to set the time derivatives of $\tilde{\rho}_{12}$, $\tilde{\rho}_{23}$ and $\tilde{\rho}_{22}$ to zero. It is worth noticing that the relation resulting from setting $(\partial/\partial t)\tilde{\rho}_{12} = 0$ is

$$\rho_{12} = \frac{\Omega_{12}}{2\Delta_{12}}\rho_{11} + \frac{\Omega^*_{23}}{2\Delta_{12}}\rho_{13} \tag{2.41}$$

Moreover, by adapting (2.36) to the effective two-level system we obtain for the time derivative of the excited state population

$$\frac{\partial}{\partial t}\tilde{\rho}_{33} = \text{Im}\left(\tilde{\rho}_{13}\Omega^*_{\text{eff}}\right) \tag{2.42}$$

Combining (2.41) and (2.42) yields

$$\frac{\partial}{\partial t}\tilde{\rho}_{33} = \text{Im}\left(\frac{2\Delta_{12}\Omega^*_{\text{eff}}}{\Omega^*_{23}}\tilde{\rho}_{12}\right) \tag{2.43}$$

where we have used that the population ρ_{11} is real, and assumed that Ω_{12} is also real[4]. This gives a measure for the absorption on the transition between the ground and the intermediate state (2.23), which is proportional to the time derivative of the population of the excited state.

[4]This is valid without loss of generality.

3 Motional Broadening Effects

In section 2.1 we presented the effect of homogeneous decoherence mechanisms on an atomic system, which lead to a broadening of the energy levels with a Lorentzian line shape. Also relevant for this thesis are the effects of the finite temperature T of the gas of Alkali atoms. Associated with the finite temperature is a Maxwell-Boltzmann distributed velocity vector $\boldsymbol{v}$. Various motional effects arise from this finite velocity, most of which are velocity dependent on the microscopic scale. These effects often appear as inhomogeneous broadenings because of the Maxwell-Boltzmann distribution of the velocity vector, which is not an intrinsic property of the atom, and therefore cannot be included in the "electronic" description of the atom.

We will focus here on two motional effects arising from a finite velocity and the finite size of the exciting light field(s) (Gaussian laser beams). Both lead to a broadening of the of the spectroscopic features, and in each case we discuss how to include them in a theoretical model. First we will consider the influence of the Doppler effect, which comes from the component of the velocity vector co-linear to the wave vector of the light field. Then we will examine the situation where the interaction volume between the light and the atoms is finite in size. This, combined to the finite velocity of the atom, leads to a finite interaction time between the atom and the light field.

3.1 Doppler effect

Let us consider an atom in an ideal gas, with a Maxwell-Boltzmann distributed velocity $\boldsymbol{v}$. Due to the Doppler effect, if we shine a light field of frequency ω_{L} and wave vector $\boldsymbol{k}_{\mathrm{L}}$ (in vacuum), the atom will see the light field with a shifted frequency ω'_{L} as

$$\omega_{\mathrm{L,D}} = \omega_{\mathrm{L}} - \boldsymbol{k}_{\mathrm{L}} \cdot \boldsymbol{v} = \omega_{\mathrm{L}} - k_{\mathrm{L}} v_{\parallel}$$

where $v_{\parallel}$ is the component of the velocity vector co-linear to the wave vector. Thus the detuning Δ_{ij} in the Hamiltonian in the rotating frame (2.33) have to be changed to

$$\Delta_{ij,\mathrm{D}} = \Delta_{ij} - k_{\mathrm{L}} v_{\parallel} \tag{3.1}$$

which yields that the response of the atom $\tilde{\rho}(t, v_{\parallel})$ is dependent on its transverse velocity. The average response an ensemble of atoms to the light field will then be given by

$$\langle \tilde{\rho}(t) \rangle_{v_{\parallel}} = \int \tilde{\rho}(t, v_{\parallel}) N(v_{\parallel}) \, \mathrm{d}v_{\parallel} \tag{3.2}$$

where $N(v_\parallel)$ is the Gaussian distribution of the one dimensional velocity component:

$$N(v_\parallel) = \sqrt{\frac{m}{2\pi k_\mathrm{B} T}} e^{-\frac{m v_\parallel^2}{2 k_\mathrm{B} T}} \tag{3.3}$$

If we define the Doppler detuning as $\delta_\mathrm{D} = -k_\mathrm{L} v_\parallel$ we can re-write the previous distribution as a Gaussian distribution of Doppler shifts:

$$N'(\delta_\mathrm{D}) = \sqrt{\frac{m}{2\pi k_\mathrm{B} T}} e^{-\frac{m \delta_\mathrm{D}^2}{2 k_\mathrm{L}^2 k_\mathrm{B} T}} \tag{3.4}$$

which has a full width at half-maximum (FWHM), also known as Doppler width, of

$$\gamma_\mathrm{D} = |k_\mathrm{L}| \sqrt{\frac{8 \ln 2 \; k_\mathrm{B} T}{m}} \tag{3.5}$$

Doppler effect and adiabatic elimination

For a three-level system, the detunings become

$$\Delta_{12,\mathrm{D}} = \Delta_{12} - k_{\mathrm{L},12} v_\parallel$$
$$\Delta_{23,\mathrm{D}} = \Delta_{23} - k_{\mathrm{L},23} v_\parallel$$

using the conventions introduced in section 2.2. In the case where the original intermediate detuning Δ_{12} is large, it would be useful to implement the adiabatic elimination of the intermediate state, as presented in section 2.3. Because the effective Rabi frequency as well as the additional energy offset in (2.39) depend on the detunings to the intermediate state, it also depends on the transverse velocity $v_\parallel$ in case of a moving atom. This includes some complexity to the system, and justify the following examination of the adiabatic elimination with Doppler effect.

To do so, we integrated numerically[1] the master equation (2.5) for the full three-level and for the reduced system. The detunings were changed to $\Delta_{12,\mathrm{D}}$ and $\Delta_{23,\mathrm{D}}$ to include the velocity, even in the effective parameters of the reduced system. The averaging over the velocity distribution was included using equation (3.2). The results of these simulations are shown in Figure 3.1(a)-(b), for parameters corresponding to those relevant in section 4. Noticeably here the detuning to the intermediate state Δ_{12} is the dominant energy scale, but not by orders of magnitude. Under all these considerations, the agreement between the two cases is found to be qualitatively good, especially at small times. As expected, the fast dynamics at short times are not present in the reduced system. Also there is some mismatch developing over time, as if the effective Rabi frequency was overestimated. By varying the parameters in these simulations, we found that this mismatch disappears when Δ_{12} is a more dominant energy scale.

For comparison purposes, we also show in Figure 3.1(c)-(d) the results for a stationary atom (i.e. $\boldsymbol{v} = 0$). Noticeably the fast dynamics are very visible, especially for $\mathrm{Im}(\tilde{\rho}_{12})$.

[1] Using a Runge-Kutta algorithm, also used in [13, 17].

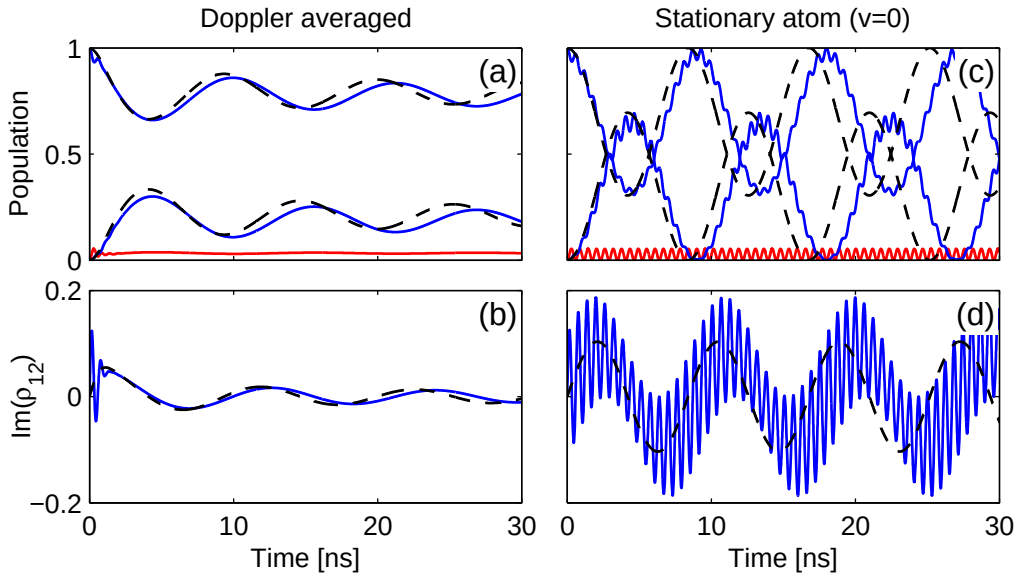

Figure 3.1: Comparison of the effective and full three-level systems, with and without Doppler effect. In (a) we show the populations of the ground and excited state obtained from numerical integration of the master equation for the full three-level system (solid blue line) and for the reduced system after adiabatic elimination of the intermediate state (dashed black line). The results are also averaged over the Doppler velocity distribution (3.2). The curves that start around 1 show the population of the ground state, those that start at 0 show the population of the excited state. Also shown is the population of the intermediate state in the full system (solid red line). In (b) $\mathrm{Im}(\tilde{\rho}_{12})$ is shown for the full three-level system (solid blue line) and for the reduced system after adiabatic elimination of the intermediate state (dashed black line). The results are also averaged over the Doppler velocity distribution. (c) and (d) show the same parameters as (a) and (b) respectively, but for a stationary atom. The parameters used in the simulation were: $\Delta_{12} = 2\pi \times 1500\,\mathrm{MHz}$, $\Delta_{13} = 0$, $\Omega_{12} = 2\pi \times 400\,\mathrm{MHz}$, $\Omega_{23} = 2\pi \times 745\,\mathrm{MHz}$, $\hat{L} = 0$, $k_{\mathrm{L},12} = +2\pi/455\,\mathrm{nm}$, $k_{\mathrm{L},23} = -2\pi/1070\,\mathrm{nm}$, and cesium atoms.

This highlights a damping mechanism of the Doppler averaging. Otherwise the same characteristics are observed with and without Doppler averaging. This justifies the use of the adiabatic elimination in a Doppler broadened ensemble of atoms.

3.2 Transit time broadening

The second effect arising from the motion of atoms is a finite time, called the transit time, during which the atom is present in the region where it can interact with the light field. If we express the typical velocity of the atoms as v and the size of the interaction

volume as D, the interaction time is of the form

$$\tau \sim \frac{D}{v} \tag{3.6}$$

If we consider that the gas of atoms is in thermodynamic equilibrium, each time that an atom leaves the interaction volume, it is replaced by an atom in the ground state. Therefore it appears logical to treat this effect as a decay to the ground state with a rate

$$\Gamma_{\mathrm{TT}} \sim \frac{1}{\tau} \sim \frac{v}{D} \tag{3.7}$$

which can be included in the Lindblad operator (2.7). In order to determine an effective decay rate representing the different velocity classes in a single number Γ_{TT}, one has to consider the time scales and the exact geometry of the system [18].

Small transit time broadening

Let us consider the configuration in which a gas of atoms at room temperature is excited by a laser beam of Gaussian profile. In this case, in contrast to the Doppler effect, the component of the velocity vector transverse with regard to the exciting light field is responsible for the effect. The typical decay rate for alkali atoms is on the order of a few MHz. The typical velocity at room temperature is $v \approx 300\,\mathrm{m.s^{-1}}$. Usually the beam sizes are $D \gtrsim 10\,\mu\mathrm{m}$, such that $\Gamma_{\mathrm{TT}} \lesssim 2\pi \times 5\,\mathrm{MHz}$. Therefore the transit time decay is not the dominant term, and one can consider that the atoms have reached a steady state when they leave the laser beam.

This situation was extensively studied theoretically and experimentally in [56], and it was found that a suitable expression for Γ_{TT} is

$$\Gamma_{\mathrm{TT}} = \frac{1}{w_0\sqrt{2\log(2)}}\sqrt{\frac{8k_{\mathrm{B}}T}{\pi m}} \tag{3.8}$$

where w_0 is the waist of the laser beam. Note also that $\sqrt{8k_{\mathrm{B}}T/(\pi m)}$ is the mean velocity of the particles in an ideal gas.

Part II

Experimental Results

4 Rydberg Aggregates: Strongly Correlated Excitation of Rydberg Atoms

Coherent excitation to Rydberg states and interaction of van-der-Waals type between Rydberg atoms in a vapor cell was previously observed in our group [13, 17, 48, 49]. These results were obtained using a pulsed amplifier system with a repetition rate of only 50 Hz. The experiments in this chapter can be seen as a spin-off of this previous work, using cesium instead of rubidium. Using cesium allows to use an excitation scheme where the need for a pulsed amplifier is eliminated, therefore allowing for a much higher repetition rate of the experiment. Here we worked in a regime where the typical interaction strength is much higher than in reference [17], and were able to observe correlated excitation phenomena, which lead to the formation of so-called Rydberg aggregates.

The first section of this chapter is devoted to describing the experimental procedure. The following section contains the quantitative analysis of the experimental results, showing a universal scaling behavior. Finally these results will be discussed and compared to a theoretical model for Rydberg aggregation [19, 20].

4.1 Experimental procedure

4.1.1 Excitation scheme

The relevant excitation scheme is shown schematically in Figure 4.1(a). The atomic medium, composed of cesium atoms, is excited from the ground state $6S_{1/2}, F = 4$ to the intermediate state $7P_{3/2}, F' = 5$ and then to the (excited) Rydberg state $nS_{1/2}$[1].

The lower transition is driven by a laser[2] at a wavelength of around 455 nm. The Rabi frequency Ω_{12} is varied between 100 and 1000 MHz, and the detuning to the intermediate state is kept constant at $\Delta_{12} = 2\pi \times 1500$ MHz. The stabilization of the laser uses standard techniques, and was previously described in [57]. For the upper

[1] In some cases, we will also show results that were obtained with the excitation scheme $6S_{1/2}, F = 3 \rightarrow 7P_{1/2}, F' = 4 \rightarrow nS_{1/2}$. All the technical considerations were the same in both cases.

[2] The laser is a commercial TA SHG pro system from Toptica.

transition, the driving laser has a wavelength of around 1070 nm. [3] In detail, depending on the principal quantum number of the Rydberg state, the wavelength spans from 1055 nm to 1075 nm. The detuning to the Rydberg state Δ'_{13} (two-photon detuning) is scanned over several GHz, and the Rabi frequency of the second transition Ω_{23} is varied between several hundreds of MHz and 2 GHz. Both lasers have the same linear polarization, and an estimated linewidth below 5 MHz.

4.1.2 Measurement procedure

The experiments described in this chapter study the excitation dynamics to the Rydberg state. In order to obtain excitation dynamics, the laser driving the upper transition was shaped into a pulse using a fast Pockels cell[4]. This Pockels cell actually contains two electro-optic modulators (EOM), each of which is made of an RTP crystal and controlled with a fast high voltage driver[5]. The voltage on each EOM is set for a phase of $\lambda/2$, such that the polarization is rotated by 90°, and is switched on for 1 μs by a TTL pulse. We can set the delay between the two TTL pulses using a delay card[5] with a precision below 1 ns. This configuration of delayed polarization rotation on the two EOMs effectively a rotation of the polarization by 90° for a variable time. After the Pockels cell the beam passes through a polarization analyzer (in practice a polarizing beamsplitter, see Figure 4.2(a)). When the polarization at the entrance of the Pockels cell is perpendicular to the main axis of the analyzer, the output light is a square pulse of variable length (between 1 and 100 ns). Here the pulse length is always set to 100 ns. The rise and fall time of the pulse is below 1.5 ns. The beginning of a 100 ns pulse is shown in Figure 4.1(b), displaying an almost square form. The extinction ratio is less than 1 %, and the efficiency of the system was at the peak of the pulse around 50 %[6]. Further characteristics of the pulse system can be found in [58].

At the heart of the experiment is the self-made glass cell containing the cesium atoms, shown in Figure 4.2(b). The square part is the main part of the cell. It is composed of two quartz optical flats with a thickness of 1 mm and a size of $5 \times 5\,\mathrm{cm}^2$ fused together on the edge with a spacing of 220 μm (defined by the U-shaped spacer). It is connected to the reservoir, a quartz tube which contains a drop of cesium metal. The cell was evacuated to a pressure below 1×10^{-6} mbar. Then the reservoir was filled with the cesium drop and sealed off. The temperature of the main part of the cell is kept constant at 200°C, and the temperature of the reservoir is varied, usually between 60°C and 150°C. The higher temperature in the main part of the cell prevents the cesium from condensing there, and the reservoir temperature sets the vapor pressure

[3] We use a commercial DL100 pro design system from Toptica seeding a self-built tapered amplifier (TA) system, which itself seeds a commercial fiber amplifier from Keopsys (KPS-CUS-BT-YFA-42-SLM-PM-HIP-111-FA-CO). The available power for the experiment is up to 15 W.

[4] From the company Leysop

[5] From the company Bergmann Messgeräte Entwicklung

[6] This efficiency is rather low, but we speculate that the high powers that were used caused the efficiency to deteriorate. Unfortunately the exact efficiency under the usual experimental operations, i.e. at high power, could not be measured exactly. However we also found that the peak power of the pulse scales linearly with the input power.

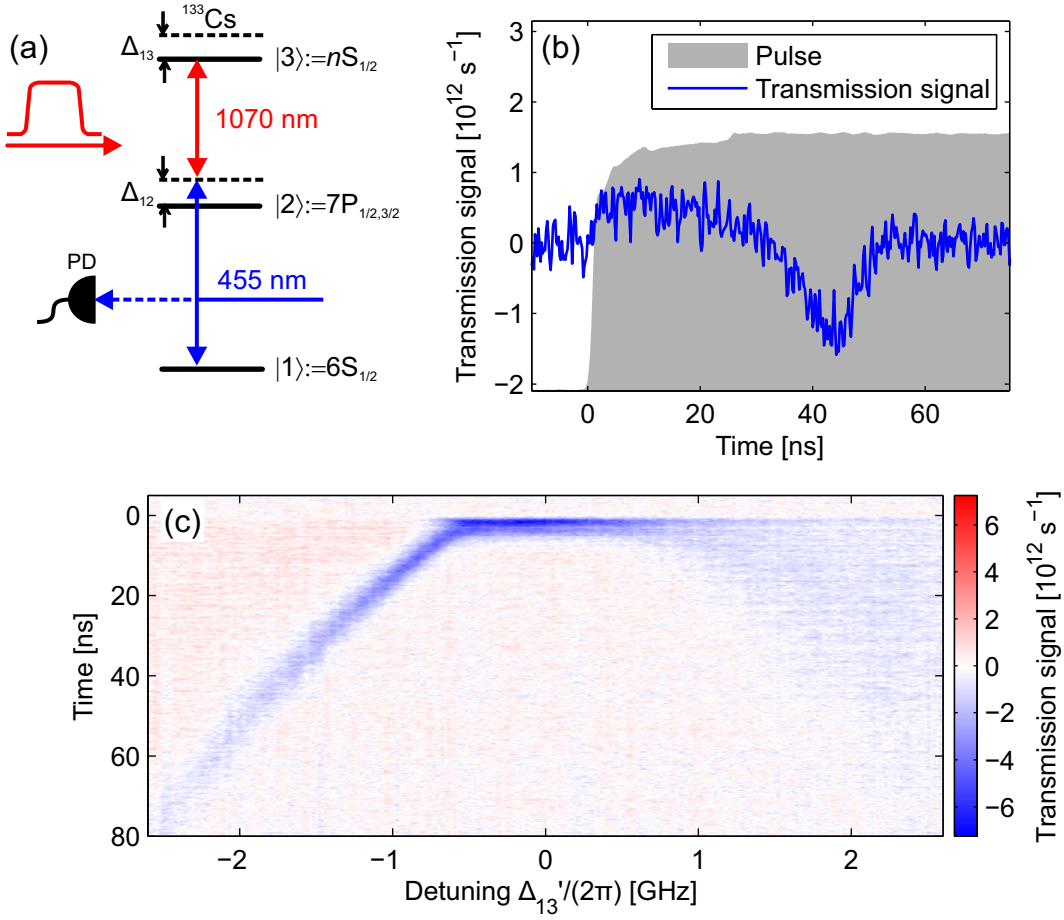

Figure 4.1: (a) Schematic energy level diagram for the excitation of ^{133}Cs atoms to Rydberg states. The detuning to the intermediate state is set to $\Delta_{12} = 2\pi \times 1500\,\mathrm{MHz}$. (b) Transmission change of the blue laser (blue curve) when the infrared pulse is applied (grey-shaded area in the background), as recorded by the oscilloscope, for the parameters are the following: 32S state, $N_\mathrm{g} = 37\,\mu\mathrm{m}^{-3}$, $\Omega_{12} = 2\pi \times 170\,\mathrm{MHz}$, $\Omega_{23} = 2\pi \times 630\,\mathrm{MHz}$ and $\Delta'_{13} = 2\pi \times -2\,\mathrm{GHz}$. The corresponding effective two-photon Rabi frequency (2.37) is $\Omega_\mathrm{eff} = 27\,\mathrm{MHz}$. (c) Density plot of the transmission change of the blue laser as a function of time (vertical axis, from top to bottom) and detuning to the Rydberg state Δ'_{13} (horizontal axis). The other parameters are the same as in (b).

in the whole cell [59]. This configuration allows for a very good control of the atomic density in the ground state N_g, which is related to the vapor pressure by the ideal gas law and the multiplicity of the ground state under consideration.

The optical setup is schematically shown in Figure 4.2(a). The 455 nm beam exits an optical fiber with a diameter of 1.25 mm ($1/e^2$ diameter). It is then focused with a 75 mm lens to a diameter of 35 μm inside the cell. The intensity of the blue beam over the length of the cell is constant since the Rayleigh range of the beam is 2 mm. After passing through the cell a 30 mm lens collimates the beam, before is is focused again onto a circular pinhole with a diameter of 25 μm. The light that is transmitted through the pinhole is then imaged onto an ultra fast photo-detector[7] in a $2f$ configuration. The photo-detector is AC-coupled, and therefore measures the change in transmission of the blue beam. This optical arrangement effectively images the pinhole to a size of 12.5 μm (2:1 telescope) at the position of the focus inside the cell. The near-field diffraction pattern from a 12.5 μm pinhole is well contained to the size of the pinhole over a distance of 110 μm [60]. Thus the pinhole effectively images a region limited to its size if its image is in the middle of the 110 μm-long cell. Additionally, the size of the image of 12.5 μm ensures that the intensity is almost constant in the imaged volume (to approx 75 %). The 1070 nm laser beam comes out of the fiber amplifier with a diameter of 1.3 mm, passes through the Pockels cell and the analyzer. It is then focused with a 30 mm lens to a diameter of 30 μm inside the cell, such that the focal points of the two beams are overlapped in all three directions. The Rayleigh range of the 1070 beam is 0.6 mm, which ensures that the infrared intensity is also constant over the length of the cell. After passing through the cell the infrared beam is collimated by the 75 mm lens. A sample of it is reflected off of a glass plate and focused onto a fast photo-diode[8], in order to measure the shape of the infrared pulse.

In practice the measurement is performed as individual detuning scans, described in the following. The frequency of the infrared beam is scanned very slowly (between 100 and 200 s) over the resonance of the Rydberg state. For each pulse of the Pockels cell, the change in transmission of the blue laser as the infrared laser is switched on is monitored by a fast oscilloscope[9]. At the same time the shape of the infrared pulse, the transmission signal of the infrared laser through a Fabry-Pérot resonator and the signal controlling the frequency of the infrared laser are also monitored. The oscilloscope records a bundle of 100 to 300 of these events, computes the average signal over the bundle and saves only the average. The recording of one bundle lasts a couple of milliseconds, and therefore the frequency of the infrared laser can be considered to be constant over the recording time. In Figure 4.1 a typical transmission signal and infrared pulse are shown. In order to reconstruct a frequency axis for the detuning Δ_{23} we evaluate the signal from the Fabry-Pérot resonator, using the well defined free spectral range of 1.5 GHz. Additionally we measure an EIT signal [57, 61] over the scanning range, which allows to set the position of the resonance from the intermediate to the Rydberg state ($\Delta_{23} = 0$). The determination of the the effective two-photon

[7] The photodiode is a commercial HSA-X-S-1G4-SI from Femto with a bandwidth of 10 kHz − 1.4 GHz
[8] DET02AFC from ThorLabs, with a bandwidth of 1.2 GHz
[9] LeCroy MSO 104MXs-B, with a bandwidth of 1 GHz and a sampling rate of 5 GS/s

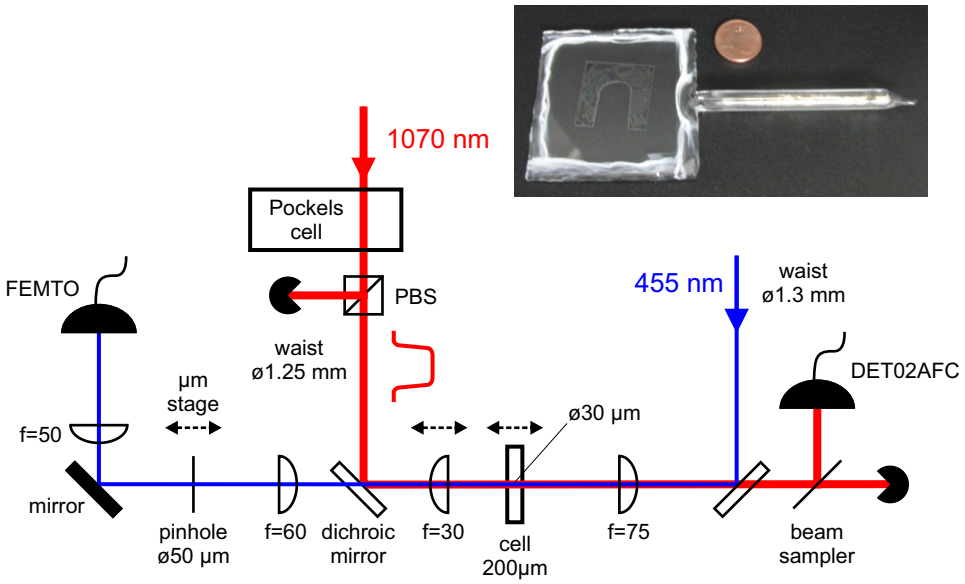

Figure 4.2: Sketch of the experimental setup used for these measurements. Inset: Picture of the glass cell used in the experiment.

detuning Δ'_{13} is in principle given by equation (2.40), which can be rewritten as

$$\Delta'_{13} = \Delta_{12} + \Delta_{23} + \frac{|\Omega_{23}|^2}{4\Delta_{23}} + \frac{|\Omega_{12}|^2}{4\Delta_{12}} \tag{4.1}$$

However of these quantities, only Δ_{23} could be calibrated precisely. The contributions of the two last terms is in the range of $\sim$ 100 MHz for our experimental settings, but cannot be determined exactly because we cannot determine the Rabi frequencies experimentally, as in [13, 17, 48, 49]. Moreover the infrared laser induces an AC Stark shift Δ_{AC} on the ground state [62, 63], and therefore the detuning to the intermediate state Δ_{12} changes when the infrared pulse is shone in. In [60], this AC Stark shift was estimated to $\Delta_{\mathrm{AC}} \approx 2\pi \times -500\,\mathrm{MHz}$. In order to lift this uncertainty, the evaluation of the two-photon detuning axis Δ'_{13} (including all terms) will be performed using the experimental data and discussed later.

Furthermore after each detuning scan, a measurement of the atomic number density N_{g} in the ground state is performed. For this, we measure and evaluate the transmission spectrum of another laser beam at around 852 nm, scanned in frequency across the D2-transition ($6S_{1/2}$ to $6P_{3/2}$). The evaluation follows the method detailed in [64], and was partly detailed in [57]. Note that we take into account a self-broadening term [48,65].

The result of one detuning scan is shown in Figure 4.1(c) as a density plot. The blue curve in Figure 4.1(b) is a cut of 4.1(c) for $\Delta'_{13} = 2\pi \times -2\,\mathrm{GHz}$, such that the absorption peak at $\sim$ 45 ns appears in blue in 4.1(c). The signal that is observed is directly proportional to the imaginary part of the coherence $\tilde{\rho}_{12}$, because the intensity varies only slightly aver the length of the cell (2.25). Since the detuning to the intermediate state is large compared to the Rabi frequencies, the adiabatic elimination of the intermediate state can be applied, as described in section 2.3. As shown in equation (2.43),

the imaginary part of the coherence is also proportional to the time derivative of the Rydberg population. In the present case, this means that the absorption peak at $\sim 45\,\mathrm{ns}$ corresponds to atoms that are transferred to the Rydberg state. For each excited Rydberg atom one photon is removed from the probe resulting in a decrease of the transmission. Therefore the quantity that is plotted in the following is the change in photon rate, or the time derivative of the total number of Rydberg atoms in the sample. This quantity is given the formula

$$S' = \frac{1}{\eta \hbar \omega_{\mathrm{L},12}} \times S \tag{4.2}$$

where S is the actual signal measured from the photodiode, $\hbar\omega_{\mathrm{L},12}$ is the energy of one 455 nm photon and η is the efficiency of the photodiode, which has been characterized to be $\eta \approx 850\,\mathrm{V/W}$.

4.1.3 Discussion

There are several striking features in this signal. First we can see a clear excitation signal to the Rydberg state over more than 5 GHz here (and more than 10 GHz for other experimental parameters). This is a much larger bandwidth than any Rabi frequency in the system. Moreover the excitation seems to become slower as the detuning Δ'_{13} increases, but in a non-interacting two level system, the relevant excitation timescale is $1/\Delta'_{13}$ for large detunings [46, 47].

As can be seen in Figure 4.3, the excitation signal becomes faster for increasing atomic densities. This is in contradiction with equation (2.25), which states that only the signal height should depend (linearly) on the density assuming that there are no interatomic interactions in the system. This strongly hints at the influence of many-body dynamics governing the excitation process.

By integrating the transmission signal over time we obtained the number of photons scattered when the infrared laser is turned on. Under the assumption that one atom is excited to the Rydberg state for each absorbed photon, the number of Rydberg atoms excited in the excitation volume reached approximately 50 000 atoms. This number is roughly constant over a wide range of experimental parameters, suggesting that there is a saturation phenomena. Such a saturation is at the heart of experiments exploiting the Rydberg blockade effect [23]. In the present case it goes beyond the blockade effect (which happens on resonance), as we see the saturation over a wide range of detuning. As discussed before, the volume of interest is the volume imaged by the pinhole inside the cell, essentially a cylinder of diameter $12.5\,\mu\mathrm{m}$ and length $220\,\mu\mathrm{m}$. With this we obtain a saturated density of Rydberg atoms of

$$N_{\mathrm{sat}} = 1.85\,\mu\mathrm{m}^{-3} \tag{4.3}$$

From the theory of three-level atoms one expects a Rydberg population on resonance of around 0.2 (see Figure 3.1). However this saturation density is lower than the ground

state densities in the system by up to two orders of magnitude, again highlighting the saturation effect.

Finally, in connection to the large bandwidth, we observe a very clear Rydberg excitation signal at large negative detunings. Line broadenings, shifts and many body dynamics have been observed with Rydberg S-states [10, 11], but only for positive detunings. These phenomena arose from dipole-dipole interaction between Rydberg atoms, which is repulsive for S-states [39] (see Figure 1.3(a-b)). However at large atomic densities, the mean inter-particle distance is so small that the higher order terms have to be included in the Rydberg-Rydberg interaction potentials. Especially for S-states in cesium, as shown in Figure 1.3 for the 32S state, the dipole-quadrupole interaction induces level crossings and state mixing between neighboring pair states. As a result initially dipole-forbidden pair states with an attractive interaction acquire some admixture of the unperturbed pair state $\varepsilon_{n\mathrm{S},n\mathrm{S}}$ (visible in blue at negative energies in Figures 1.3(d) and 4.9) at short inter-atomic distances due to the dipole-quadrupole interaction. Therefore the Rydberg-Rydberg interaction for S-states in cesium at short distances also feature attractive components (visible in blue at negative energies in Figure 1.3(d)), allowing for us to observe an excitation signal at large red detunings. This will be further discussed in the following sections.

In the following we will mostly examine the signal at negative detunings, where there is a clear absorption feature that can be evaluated. For the analysis we will mostly study the characteristic time delay t_{sat} of the absorption feature associated with the excitation to the Rydberg state (as depicted in Figure 4.3) in order to shed light on the underlying mechanisms and interactions.

4.2 Scalings

As already shown in Figure 4.1(c) and 4.3, the time scale t_{sat} depends on the detuning to the Rydberg state Δ'_{13} and on the atomic ground state density N_{g}. Here we systematically vary experimental parameters independently and evaluate the scaling of t_{sat} in a power law form as a function of them in the form

$$t_{\mathrm{sat}} \propto |\Delta'_{13}|^a (\Omega_{\mathrm{eff}})^b (N_{\mathrm{g}})^c (n^*)^d \tag{4.4}$$

In the following evaluation the parameters of the system will be always such that all but one are kept constant. When not varied the parameters are the same as in Figure 4.3 except when stated otherwise, i.e. 32S state ($n^* = 27.95$), $\Omega_{12} = 2\pi \times 166\,\mathrm{MHz}$, $\Omega_{23} = 2\pi \times 745\,\mathrm{MHz}$, $\Delta'_{13} = 2\pi \times -2.2\,\mathrm{GHz}$ and $N_{\mathrm{g}} = 36\,\mu\mathrm{m}^{-3}$. We determine t_{sat} as the line center of an asymmetrical Lorentz profile fitted to the transmission signals.

Detuning scaling

The dependence of t_{sat} on the detuning is shown in Figure 4.4(a), plotted against the detuning between the intermediate state and the Rydberg state Δ_{23}. We fit to

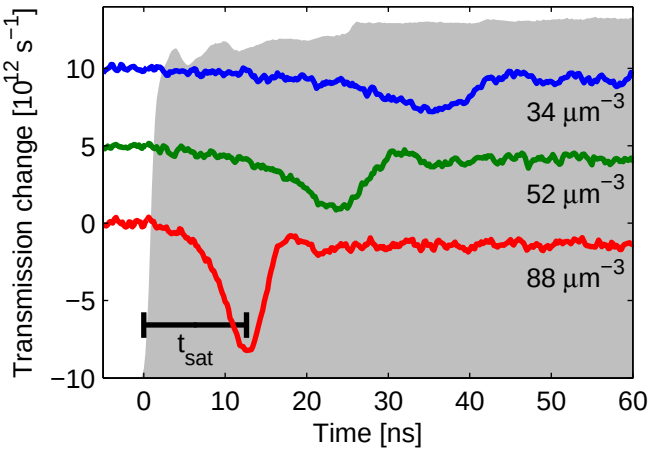

Figure 4.3: Transmission signals at three different atom number densities N_g in a waterfall fashion. The vertical axis has been converted to a photon rate. Also shown is the time delay t_{sat} of the absorption peak used as the characteristic quantity for the quantitative analysis. Here the parameters were: 32S state, $\Omega_{12} = 2\pi \times 166\,\mathrm{MHz}$, $\Omega_{23} = 2\pi \times 745\,\mathrm{MHz}$ and $\Delta'_{13} = 2\pi \times -2.2\,\mathrm{GHz}$, meaning that $\Omega_{\mathrm{eff}} = 50\,\mathrm{MHz}$ (for $\Delta'_{13} = 0$). In comparison to Figure 4.1(b) the averaging was increased by a factor ~ 10. The grey shaded area in the background is the temporal shape of the infrared pulse.

the experimental data a power law function of the form $|\Delta_{23} + \Delta_{23}^{(0)}|^a$, where $\Delta_{23}^{(0)}$ is the detuning of the two-photon resonance. The fit results in $a = 1.99(14)$ and $\Delta_{23}^{(0)} = 2\pi \times 800(170)\,\mathrm{MHz}$, where the uncertainty represent the confidence region of the fit. Note that the fitted value of $\Delta_{23}^{(0)}$ is consistent with the expected AC Stark shift $\Delta_{\mathrm{AC}} \approx 2\pi \times -500\,\mathrm{MHz}$ combined with the small corrections arising from the Rabi frequency in (4.1). In all the following evaluation, the two-photon detuning axis is defined as (note that $\Delta_{23}^{(0)}$ contains the detuning to the intermediate state Δ_{12})

$$\Delta'_{13} = \Delta_{23} + \Delta_{23}^{(0)} \tag{4.5}$$

and the detuning scaling can be re-written as

$$t_{\mathrm{sat}} \propto |\Delta'_{13}|^{1.99(14)} \tag{4.6}$$

Rabi frequency scaling

We can now examine the scaling of the characteristic time against the Rabi frequency. For this we performed detuning scans at various blue Rabi frequencies Ω_{12}. Varying the blue Rabi frequency was chosen so that the AC Stark shift, which depends on the infrared power, remains constant. For each value of the Rabi frequency we measure one detuning scan, and then evaluate t_{sat} at a fixed detuning ($\Delta'_{13} = 2\pi \times -2.2\,\mathrm{GHz}$).

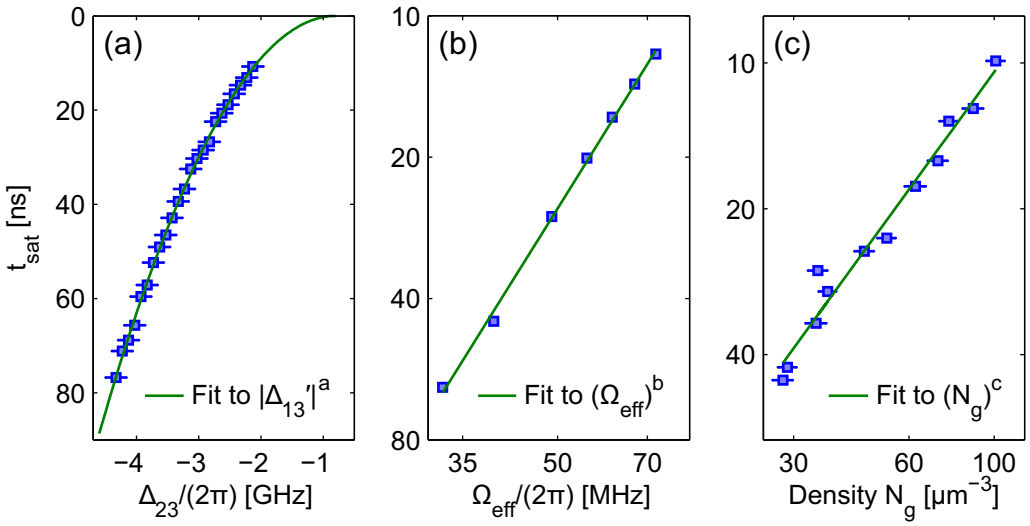

Figure 4.4: Characteristic time t_{sat} as a function of the detuning, Rabi frequency and ground state density. The experimental parameters are: 32S state ($n^* = 27.95$), $\Omega_{12} = 2\pi \times 166\,\mathrm{MHz}$, $\Omega_{23} = 2\pi \times 745\,\mathrm{MHz}$, $\Delta'_{13} = 2\pi \times -2.2\,\mathrm{GHz}$ and $N_{\mathrm{g}} = 36\,\mu\mathrm{m}^{-3}$, all but one kept constant. A power law function is fitted to each set of experimental data. The blue squares represent the experimental data, and the green lines represent the fits to the data. (a) Detuning scaling of t_{sat}. The power law function $|\Delta'_{13}|^a$ is fitted in a linear scale, including the position of the two-photon resonance, to $a = 1.99(14)$ and $\Delta'_{13} = \Delta_{23} + \Delta_{23}^{(0)}$ with $\Delta_{23}^{(0)} = 2\pi \times 800(170)\,\mathrm{MHz}$ (see text for details). The error bars for the experimental data represent the confidence region of the fit of the two photon resonance (i.e. $2\pi \times 170\,\mathrm{MHz}$). (b) Scaling of t_{sat} when the blue Rabi frequency Ω_{12} is varied. The horizontal axis is the effective Rabi frequency Ω_{eff} at the two-photon resonance (see text for details). The fit to the data is performed in a double logarithmic scale, as $(\Omega_{\mathrm{eff}})^b$ with $b = -2.10(5)$. (c) Density dependence of t_{sat}. The error bars for the experimental data represent the confidence region of the density evaluation. The fit to the data is performed in a double logarithmic scale, as $(N_{\mathrm{g}})^c$ with $c = -1.09(6)$.

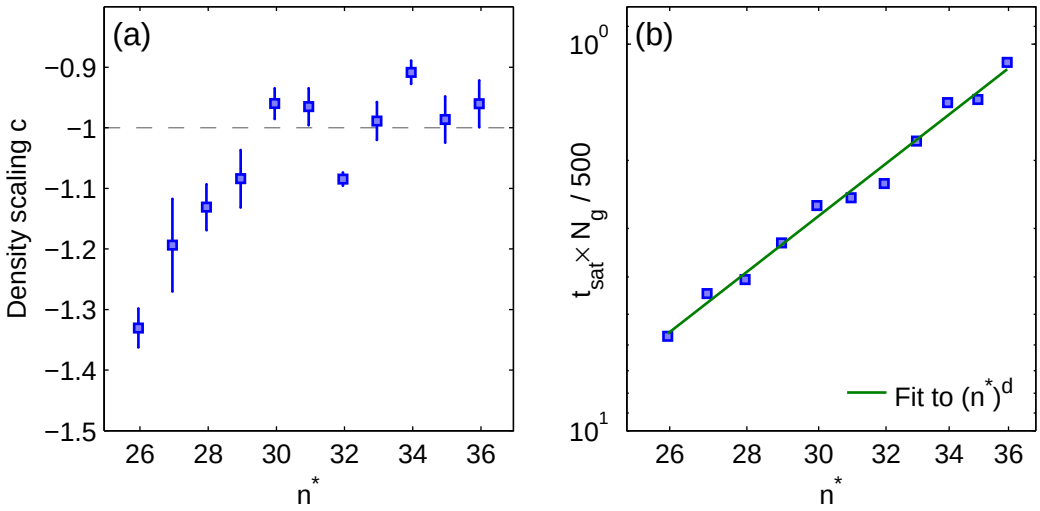

Figure 4.5: Density scaling of t_{sat} for different Rydberg states. The experimental parameters are: 30S to 40S state ($n^* = 25.95 \ldots 35.95$), $\Omega_{12} = 2\pi \times 164\,\mathrm{MHz}$, $\Omega_{23} = 2\pi \times 633\,\mathrm{MHz}$, $\Delta'_{13} = 2\pi \times -2.2\,\mathrm{GHz}$ and $N_{\mathrm{g}} = 17 \ldots 68\,\mu\mathrm{m}^{-3}$. The error bars represent the confidence region of the fits. (a) Power law scaling exponent c (as $t_{\mathrm{sat}} \propto (N_{\mathrm{g}})^c$) for various effective principal quantum number n^* (blue squares). The fitting procedure is the same as in Figure 4.4. The dashed grey is the baseline for the evaluation of the scaling against the quantum number. (b) Amplitude factor of the fit of the data to $t_{\mathrm{sat}} \propto (N_{\mathrm{g}})^{-1}$ (blue squares). The green line is the fit of the amplitude factor to $(n^*)^d$ with $d = -4.8(2)$.

In Figure 4.4(b) t_{sat} is shown as a function of the effective two-photon Rabi frequency Ω_{eff}[10], in a double logarithmic scale. We fit a power law scaling to the data and obtain that

$$t_{\mathrm{sat}} \propto (\Omega_{\mathrm{eff}})^{-2.10(5)} \tag{4.7}$$

Density scaling

As can be seen in Figure 4.3, t_{sat} also depends of the ground state density. The evaluation of t_{sat} as a function of N_{g} is shown in Figure 4.4(c). We find that there is a power law scaling between t_{sat} and the density as

$$t_{\mathrm{sat}} \propto (N_{\mathrm{g}})^{-1.09(6)} \tag{4.8}$$

Quantum number scaling

As discussed previously the dependence of the dynamics on the atomic density suggests that many-body dynamics govern the excitation process, with an underlying interaction

[10] Ω_{eff} is given here at the two-photon resonance, i.e. $\Omega_{\mathrm{eff}} = \frac{\Omega_{12}\Omega_{23}}{2\Delta_{12}}$, because the Rydberg atoms are mostly excited resonantly due to an interaction shift (see section 4.3).

acting on the Rydberg states. The generic form for the energy of such an interaction is (see Table 1.1)

$$V = \frac{C_\alpha}{r^\alpha} = C_\alpha (N_\mathrm{g})^{\frac{\alpha}{3}} \tag{4.9}$$

where r is the inter-particle distance and C_α depends as a power law on the effective quantum number n^*. Thus we have $V \propto (n^*)^\beta (N_\mathrm{g})^{\frac{\alpha}{3}}$, meaning that the excitation dynamics should also depend on the effective quantum number, with a connection to the atomic density.

In order to examine the dependence on n^*, we first examine the density scaling for various Rydberg states. We performed the measurement the density scaling c for nS states with $n = 30 \ldots 40$, each time with the following atomic parameters: $\Omega_{12} = 2\pi \times 164\,\mathrm{MHz}$, $\Omega_{23} = 2\pi \times 633\,\mathrm{MHz}$, $\Delta'_{13} = 2\pi \times -2.2\,\mathrm{GHz}$ and $N_\mathrm{g} = 17 \ldots 68\,\mu\mathrm{m}^{-3}$. The power law density scaling c is shown in Figure 4.5(a) as a function of the effective quantum number n^*. In spite of small deviations at low n^* we find that c is in good agreement with minus unity for all Rydberg states. Since an interaction potential acting on Rydberg states depends on both the density and the quantum number (from equation (4.9)) and $c \approx -1$, we now fit the function $(N_\mathrm{g})^{-1}$ to the data for each Rydberg state. The fitted amplitude factor $t_\mathrm{sat} \times N_\mathrm{g}$ is plotted against n^* in Figure 4.5(b), showing a clear dependence of the excitation dynamics on the effective quantum number as

$$t_\mathrm{sat} \propto (N_\mathrm{g})^{-1} (n^*)^{-4.8(2)} \tag{4.10}$$

4.3 Aggregation of Rydberg excitations

To summarize the experimental results, we have observed many-body excitation dynamics (from the density dependence), with a strong Rydberg dependence (from the n^* scaling). We were able to characterize the effect by measuring power law scalings of the characteristic time scale as a function of several experimental parameters. In this section we will introduce the concept and the theoretical description of Rydberg aggregation (summarized from [19, 20]). We will compare the results of this model to those of our experiment, and discuss the limitations of the model.

4.3.1 Theory of aggregation

Let us consider an ensemble of N atoms which can be reduced to two level atoms. Each atom k has a ground state $|1_k\rangle$ and a Rydberg state $|3_k\rangle$. These atoms are coupled (with light) by a Rabi frequency Ω_{eff}[11], and there is a homogeneous dephasing with a rate of γ_{13}. We also assume that decay processes are negligible. For each atom k the Hamiltonian in the rotating frame and the Lindblad operator are (see section 2.2)

$$\begin{aligned} H^{(k)} &= \hbar \begin{pmatrix} 0 & \frac{1}{2}\Omega_{\text{eff}} \\ \frac{1}{2}\Omega_{\text{eff}} & -\Delta'_{13} \end{pmatrix}_k \\ &= -\Delta'_{13}\hat{C}^{(k)}_{33} + \frac{1}{2}\Omega_{\text{eff}}\left(\hat{C}^{(k)}_{13} + \hat{C}^{(k)}_{31}\right) \end{aligned}$$

and

$$\begin{aligned} \hat{L}^{(k)}(\tilde{\rho}) &= -\frac{1}{2}\gamma_{13}\begin{pmatrix} 0 & \tilde{\rho}_{13} \\ \tilde{\rho}_{31} & 0 \end{pmatrix}_k \\ &= \gamma_{31}\left(\hat{C}^{(k)}_{33}\tilde{\rho}\hat{C}^{\dagger(k)}_{33} - \frac{1}{2}\left(\hat{C}^{\dagger(k)}_{33}\hat{C}^{(k)}_{33}\tilde{\rho} + \tilde{\rho}\hat{C}^{\dagger(k)}_{33}\hat{C}^{(k)}_{33}\right)\right) \end{aligned} \tag{4.11}$$

where $\hat{C}^{(k)}_{ij} = |i_k\rangle\langle j_k|$ is the transition operator (as defined in section 2.1) for the k-th atom. Additionally two atoms k and m excited in the Rydberg state interact with a potential of the form

$$V_{km} = \frac{C_\alpha}{|\boldsymbol{r}_k - \boldsymbol{r}_m|^\alpha} \tag{4.12}$$

where $\boldsymbol{r}_k$ is the position of the k-th atom, and $\alpha = 6$ (3) for van-der-Waals (dipole-dipole) interaction (see section 1.3). Also the detuning is assumed to have the same sign than the interaction potential. The dynamics of the density matrix $\tilde{\rho}$ is governed by the Liouville-von Neumann equation (2.5), where the Hamiltonian and Lindblad operator for the system of N atoms with the interaction take the form [19, 20]

$$\frac{1}{\hbar}H = \frac{1}{2}\Omega_{\text{eff}}\sum_k\left(\hat{C}^{(k)}_{13} + \hat{C}^{(k)}_{31}\right) - \Delta'_{13}\sum_k\hat{C}^{(k)}_{33} + \sum_{k\neq m}V_{km}\hat{C}^{(k)}_{33}\hat{C}^{(m)}_{33}$$

[11] We use the formalism of section 2.3 for convenience here, and assume that Ω_{eff} is real.

and

$$\hat{L}(\tilde{\rho}) = \gamma_{31} \sum_k \left(\hat{C}_{33}^{(k)} \tilde{\rho} \hat{C}_{33}^{(k)} - \frac{1}{2} \left(\hat{C}_{33}^{(k)} \tilde{\rho} + \tilde{\rho} \hat{C}_{33}^{(k)} \right) \right) \tag{4.13}$$

The key assumption now is that the dephasing is strong compared to the coherent dynamics in the system, i.e. $\gamma_{13} \gg \Omega_{\text{eff}}/2$. Under this assumption the coherences of the density matrix dephase exponentially fast (on timescales $\sim \gamma_{13}^{-1}$) and can be eliminated, such that only the populations remain of interest (for the derivation, see [19,20]). The system then reduces effectively to an ensemble of classical spins configurations, much easier to compute, where the states are direct products of the no-interacting single atom eigenstates $\prod_k |i_k\rangle_{i\in\{1,3\}}$. The equation governing the system is a classical rate equation, with a (de-)excitation transition rate for each atom k given by

$$\Gamma_k = \frac{\Omega_{\text{eff}}^2 \gamma_{31}}{\left(\frac{\gamma_{31}}{2}\right)^2 + \left(-\Delta'_{13} + \sum_{m \neq k} V_{km} n_m \right)^2} \tag{4.14}$$

where n_m is the excitation number for atom m, $n_m = 1$ (0) if the atom is in the Rydberg (ground) state. The summation essentially adds to the detuning the interaction induces by all the atoms that are in the Rydberg state. We can define a specific distance, called the facilitation radius

$$r_{\text{fac}} = \left| \frac{C_\alpha}{\Delta'_{13}} \right|^{\frac{1}{\alpha}} \tag{4.15}$$

Assuming that only one atom is in the Rydberg state, r_{fac} for which the second term of the denominator vanishes. There is therefore a maximum in the transition rate at a distance r_{fac} of a Rydberg atom.

The evolution of the system can be computed numerically using a kinetic Monte-Carlo method. The system can be characterized by the total number of Rydberg atoms $N_{\text{ryd}} = \sum_k n_k$. The interaction term V_{km} in (4.13) is an energy shift. Therefore it is not involved in (2.42), which states that the imaginary part of the coherence is proportional to the time derivative of the Rydberg population. So equation (2.42) can be generalized to the imaginary part of the overall coherence $\langle \tilde{\rho}_{13} \rangle$ as [20]

$$\text{Im}(\langle \tilde{\rho}_{13} \rangle) = \sum_k \Gamma_k (1 - 2n_k) \tag{4.16}$$

We can also define the total excitation rate as

$$\Gamma = \sum_k \Gamma_k \tag{4.17}$$

and the local excitation rate at each position

$$\Gamma_{\boldsymbol{r}} = \frac{\Omega_{\text{eff}}^2 \gamma_{31}}{\left(\frac{\gamma_{31}}{2}\right)^2 + \left(-\Delta'_{13} + \sum_m \frac{C_\alpha}{|\boldsymbol{r} - \boldsymbol{r}_m|^\alpha} n_m \right)^2} \tag{4.18}$$

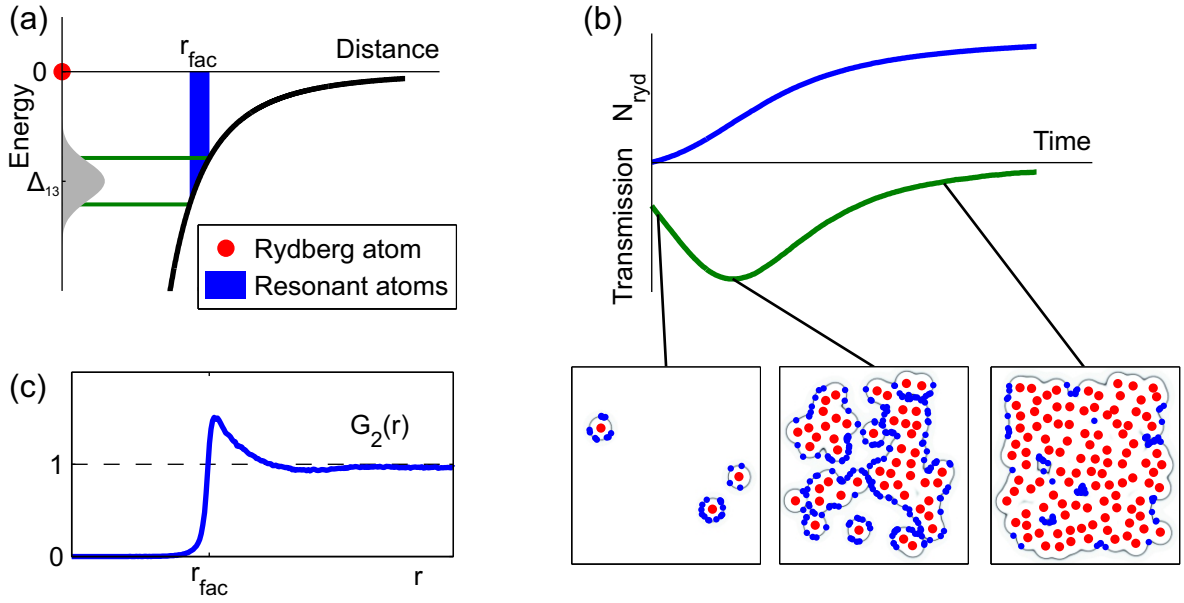

Figure 4.6: Principle of the Rydberg aggregation. (a) Interaction induced level shift. An already excited Rydberg atom (red dot) at the origin produces an energy shift for the neighboring atoms. At the facilitation radius r_{fac}, the atoms are exactly shifted in resonance with the excitation laser, red-detuned by Δ'_{13}. The grey shaded area symbolizes the excitation bandwidth, a Gaussian whose width is given by the dephasing rate γ_{31}. (b) Top: Typical time evolution of the Rydberg population N_{ryd} and of the transmission change of the exciting laser during the aggregation process. Bottom: Snapshots of the aggregation at three different times for a frozen gas in 2D[12]. Red dots correspond to Rydberg atoms. Blue dots correspond to resonant atoms. The spatial distribution of the total excitation rate $\Gamma_{\boldsymbol{r}}$ is plotted as a density plot in the background of each snapshot. The resonant shell, in which the excitation of Rydberg atoms is facilitated, is visible as a dark grey line. (c) Sketch of the density-density correlation function $G_2(r)$ expected for the steady state (corresponding to the snapshot at large time in (b)).

The physics behind this model can be captured as follows. If we consider that the ensemble of atoms is initially in the ground state and that the excitation field is far-detuned ($|\Delta'_{13}| \gg \gamma_{31} \gg \Omega_{\mathrm{eff}}$), each atom has a small probability to be excited. Eventually one atom will be excited to the Rydberg state. The situation then changes to the one shown schematically in Figure 4.6(a). At a certain distance r_{fac} from the Rydberg atom the Rydberg states of the neighboring atoms are shifted exactly in resonance with the detuned excitation fields ($C_\alpha / r_{\mathrm{fac}}^\alpha = \Delta'_{13}$), where the excitation (or de-excitation) is favored. We call the region of space at a distance r_{fac} from a Rydberg atom the resonant shell, whose width is given by the excitation bandwidth (γ_{13}) and the slope of the interaction potential.

In Figure 4.6(b) we show the number of Rydberg atoms and the change in transmission of the exciting lasers $\Delta I \propto -\mathrm{Im}(\langle\tilde{\rho}_{13}\rangle)$ (using (2.25) and (4.16)). Here one can see that

[12]Courtesy of Igor Lesanovsky, University of Nottingham, UK.

the Rydberg population grows increasingly faster as more and more Rydberg atoms are excited and provide the resonance condition at a distance r_{fac} from themselves. At the same time the change in transmission, which is proportional to the overall transition rate, reaches a maximum. Eventually the system is full of Rydberg atoms and the interaction shift becomes too large overall, such that N_{ryd} saturates and the transmission converges back to zero. Also shown in Figure 4.6(b) are snapshots of the aggregation process in a 2D ensemble of atoms. Red dots corresponds to Rydberg atoms and blue dots correspond to ground state atoms that lie in the excitation shell. In the background of each snapshot is a density plot of the local excitation rate $\Gamma_{\boldsymbol{r}}$ (4.18). The dark grey region is the resonant shell, where the excitation rate is large. With the snapshots one can look at the microscopics of the model. At small time, shortly after the atom-light coupling is turned on, only few atoms can be excited off-resonantly (left snapshot). As soon as some atoms are excited, ground state atoms that find themselves inside the resonant shell (blue dots) can be excited very efficiently as they are shifted into resonance by the Rydberg atom. The subsequent excitations tend to occur inside the resonant shell, i.e. at the specific distance r_{fac}, forming aggregates of Rydberg atoms (middle snapshot). As further atoms are excited, the resonant shell grows and it becomes more and more probable to excite Rydberg atoms. This translates to the increase in transmission change. Finally the resonant shell mostly lies outside of the medium and only few atoms are resonant, leading to the saturation of the Rydberg number (right snapshot). Because atoms are preferably excited at a distance r_{fac}, the ensemble of Rydberg atoms exhibit strong spatial correlations. In order to quantify the spatial correlations we use the density-density correlation function [66] defined as

$$G^{(2)}(r) = \frac{N^2}{N_{\text{ryd}}^2} \frac{\sum_{i \neq j} n_i n_j \mathbb{1}_{\text{d}r}(|\boldsymbol{r}_i - \boldsymbol{r}_j| - r)}{\sum_{i \neq j} \mathbb{1}_{\text{d}r}(|\boldsymbol{r}_i - \boldsymbol{r}_j| - r)} \tag{4.19}$$

where $\mathbb{1}_{\text{d}r}$ is the indicator function of an interval of width dr around 0:

$$\mathbb{1}_{\text{d}r}(x) = \begin{cases} 1 & \text{if } |x| \leq \text{d}r/2 \\ 0 & \text{else} \end{cases}$$

The denominator in (4.19) is the number of pairs of atoms at a distance r (in an interval of width dr), while in the numerator is the number of pairs of Rydberg atoms (the $n_i n_j$ term only accounts for the pairs of Rydberg atoms). A typical density-density correlation function for a 3D ensemble is shown in Figure 4.6(c). At small distances there are no pairs excited because of the strong and diverging interaction potential. However a clear peak appears at the facilitation radius, highlighting the spatially correlated excitations. No structure is visible at large distances, meaning that there is no long-range order in the system. The absence of long-range order arise from the isotropic character of the facilitated excitation process, which does not favor the creation of crystalline arrangements.

Such Rydberg aggregates have been observed recently in cold atoms systems [10, 11]. There is currently a strong interest in understanding these types of dissipative many-body systems in atomic physics. The hope is to shed light on the underlying physics,

which could be applied to the field of soft-matter physics. There are also frameworks used to achieve spatially correlated or ordered states [8, 67–70].

4.3.2 Comparison of theory and experiment

The change in transmission from the aggregation theory (green curve in Figure 4.6) is very similar to the signals that are observed in the experiment. At time $t = 0$ it starts around zero, then shows a peak in absorption before converging to zero again. We can also define a time t_{sat} for the theoretical signal as the time of the minimum transmission, and we will compare the scaling law and absolute value of both theory and experiment, again in the form

$$t_{\mathrm{sat}} \propto |\Delta'_{13}|^a (\Omega_{\mathrm{eff}})^b (N_{\mathrm{g}})^c (n^*)^d \tag{4.20}$$

First however we need to verify that our experimental system satisfies the assumptions of the theoretical model for aggregation.

Prerequisites

The very first assumption is that the atoms can be reduced to two-level atoms, and that decay mechanisms are negligible on the timescale of interest. The detuning to the intermediate state is large $\Delta_{12} = 2\pi \times -1500\,\mathrm{MHz}$, such that the adiabatic elimination of the intermediate state can be performed, as shown in section 2.3 and chapter 3. Moreover only the natural decay from the Rydberg state has to be considered in the reduced two-level system, and it is for the states of interest here smaller than 100 kHz, so also negligible. Concerning the transit time decay caused by the finite laser spot size, equation (3.8) gives for the experimental conditions $\Gamma_{\mathrm{TT}} = 2\pi \times 2\,\mathrm{MHz}$, which is also negligible on the time scale of the experiment.

Second the aggregation theory presented above assumes that there is strong dissipation, i.e. $\gamma_{13} \gg \Omega_{\mathrm{eff}}/2$. In the experiment motional effects lead to a very large broadening, both as the Doppler effect and as a transit time broadening arising from the atoms flying through the resonant shell. The Doppler shift δ_{D} of the reduced two-level system is given by the sum of the Doppler shifts on the two transitions of the original three-level system. Therefore the effective wave number for the reduced system is $(k_{\mathrm{L},23} - k_{\mathrm{L},12})$ because the two lasers are aligned in a counter-propagating manner. The two-photon Doppler width is then

$$\gamma_{\mathrm{D}} = |k_{\mathrm{L},23} - k_{\mathrm{L},12}| \sqrt{\frac{8 \ln 2 \; k_{\mathrm{B}} T}{m}} \tag{4.21}$$

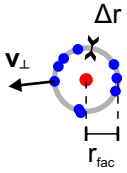

Figure 4.7: A Rydberg atom (red) with ground state atoms (blue) inside the resonant shell (grey line) of width Δr. Resonant atoms move outside of the shell with the perpendicular velocity component $\mathbf{v}_\perp$.

and is the minimum apparent width, since average response of the atoms is integrated over all velocities with the Gaussian weighting distribution (see equation (3.2)). At 200°C in the experiment we have $\gamma_{\mathrm{D}} = 2\pi \times 512\,\mathrm{MHz}$.

A transit time dephasing term also needs to be considered. In Figure 4.7 the atoms that are resonant are shown in blue. Because of their thermal motion, the atoms spend only a small amount of time inside the resonant shell, where they can be excited. The interaction time inside the resonant shell is $\tau = \Delta r/|\mathbf{v}_\perp|$, where Δr is the width of the resonant shell and $\mathbf{v}_\perp$ is the velocity component that is perpendicular to resonant shell. As for the transit time broadening rate, we then take the value given by the formula

$$\gamma_{\mathrm{TT}} = \frac{\langle v_\perp \rangle}{\Delta r} \tag{4.22}$$

where $\langle v_\perp \rangle = \frac{1}{\sqrt{3}}\sqrt{\frac{8k_{\mathrm{B}}T}{\pi m}}$, which is the one dimensional mean atomic velocity in a thermal gas. At the temperature of 200°C in the experiment, this 1D mean velocity is $\langle v_\perp \rangle = 158\,\mathrm{m.s^{-1}}$. Since both broadening mechanisms are Gaussian, the total dephasing rate is given by

$$\gamma_{13} = \sqrt{(\gamma_{\mathrm{D}})^2 + (\gamma_{\mathrm{TT}})^2} \tag{4.23}$$

This amounts to $\gamma_{13} \gtrsim 2\pi \times 500\,\mathrm{MHz}$, which is indeed larger than the Rabi frequencies in the experiment

Implementation

In the aggregation model the density of Rydberg atoms saturates at $N_{\mathrm{sat}} \approx r_{\mathrm{fac}}^{-3}/2$ (see Figure 3 in [19]). Therefore, using the value of N_{sat} determined experimentally (4.3) we estimate the facilitation radius to be

$$r_{\mathrm{fac}} = 0.65\,\mu\mathrm{m} \tag{4.24}$$

The facilitation radius is actually detuning dependent (see equation (4.15)). In order to determine an effective interaction potential we assume a detuning of $\Delta'_{13} = 2\pi \times -1500\,\mathrm{MHz}$. This yields the strength of interaction $C_\alpha = \Delta'_{13} \times r_{\mathrm{fac}}^\alpha$. We consider both the case of van-der-Waals interaction with $C_6 = 2\pi \times -109\,\mathrm{MHz} \cdot \mu\mathrm{m}^6$, and dipole-dipole interaction with $C_3 = 2\pi \times -405\,\mathrm{MHz} \cdot \mu\mathrm{m}^6$. These values are used as input for the simulations of the aggregation model.

Concerning the dephasing rate, it is given by equations (4.22) and (4.23). We also need the width of the resonant shell Δr. Assuming only one Rydberg atom as in Figure 4.7, the excitation rate around this atom is given by

$$\Gamma(r) = \frac{\Omega_{\mathrm{eff}}^2 \gamma_{31}}{\left(\frac{\gamma_{31}}{2}\right)^2 + \left(-\Delta'_{13} + \frac{C_\alpha}{r^\alpha}\right)^2}$$

By solving the equation $\Gamma(r_{\mathrm{fac}} \pm \Delta r/2) = \Gamma(r_{\mathrm{fac}})/2$ we obtain the following expression for Δr:

$$\Delta r = \frac{1}{\alpha} r_{\mathrm{fac}} \frac{\gamma_{13}}{|\Delta'_{13}|} \tag{4.25}$$

	$a\,[\lvert\Delta_{13}\rvert]$	$b\,[\Omega_{\mathrm{eff}}]$	$c\,[N_{\mathrm{g}}]$	$d\,[n^*]$
Experiment	1.99(14)	−2.10(5)	−1.09(6)	−4.8(2)
van-der-Waals	2.15(1)	−2	−0.86(1)	−4.72(5)
dipole-dipole	2.38(0)	−2	−0.74(1)	−2.95(2)

Table 4.1: Power law scalings for the aggregation time scale t_{sat}. The power law scalings from the experiment are those determined in section 4.2. For the other two lines the power law scalings were extracted from simulations in an ensemble of randomly and uniformly distributed atoms with van-der-Waals (ensemble of 10^3 atoms) dipole-dipole interaction (ensemble of 15^3 atoms) respectively, using the parameters from the experiment and the extracted interaction strengths (see text). The dephasing rate was also extracted from the experiment. All uncertainties represent the confidence region of the fits. No uncertainty is given for the exponent of Ω_{eff} in the theory, fixed at -2 as by the assumption of strong dephasing.

Equations (3.8), (4.23) and (4.22) yield the following self-consistent equation for for the motional dephasing rate

$$\frac{\langle v_\perp \rangle}{\gamma_{\mathrm{TT}}} = \frac{1}{\alpha} r_{\mathrm{fac}} \frac{\sqrt{(\gamma_{\mathrm{D}})^2 + (\gamma_{\mathrm{TT}})^2}}{|\Delta'_{13}|} \tag{4.26}$$

Solving equation (4.26) we obtain the following values for the motional dephasing rate, total dephasing rate and width of the resonant shell (at $\Delta'_{13} = 2\pi \times -1500\,\mathrm{MHz}$), for the effective van-der-Waals (with 'vdW' superscript) and dipole dipole interaction (with 'dd' superscript)

$$\begin{aligned} \gamma_{\mathrm{TT}}^{\mathrm{vdW}} &= 2\pi \times 493\,\mathrm{MHz} \\ \gamma_{13}^{\mathrm{vdW}} &= 2\pi \times 711\,\mathrm{MHz} \\ \Delta r^{\mathrm{vdW}} &= 51\,\mathrm{nm} \end{aligned} \qquad \left| \qquad \begin{aligned} \gamma_{\mathrm{TT}}^{\mathrm{dd}} &= 2\pi \times 296\,\mathrm{MHz} \\ \gamma_{13}^{\mathrm{dd}} &= 2\pi \times 591\,\mathrm{MHz} \\ \Delta r^{\mathrm{dd}} &= 85\,\mathrm{nm} \end{aligned} \right.$$

We performed simulations of the aggregation model described above using a kinetic Monte-Carlo algorithm [12, 19][13] with all atoms in the ground state initially. The principle of the algorithm is the following. At every time step the transition rates Γ_k are computed. The (de-)excitation of one atom is randomly selected, with for each atom Γ_k as the transition probability. Then the length of the time step associated with this transition is also randomly chosen and weighted by the total excitation rate Γ. The ensemble of atoms was chosen to be a cube of 10^3 (resp. 15^3) randomly distributed atoms for van-der-Waals (resp. dipole-dipole) interaction, at the same atomic density as in the experiment. The results were averaged over 1000 single realizations of the evolution of the Rydberg number and change in transmission.

We performed the simulations for the same parameter ranges as in the experiment[14], and evaluated the characteristic time scale t_{sat} (maximum of the transmission change).

[13]The Computation was performed by Igor Lesanovsky, University of Nottingham, UK

[14]Varying Δ'_{13}, N_{g} and C_α and making use of $C_6 \propto (n^*)^1 1$ and $C_3 \propto (n^*)^4$ (from Table 1.1).

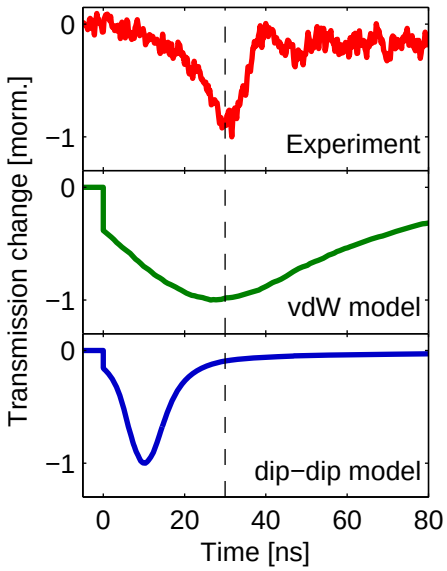

Figure 4.8: Transmission change (normalized) as a function of time in the experiment (top panel) and in the simulation with van-der-Waals (middle panel) and dipole-dipole interaction (bottom panel). The parameters are: 32S state, $\Omega_{12} = 2\pi \times 166\,\mathrm{MHz}$, $\Omega_{23} = 2\pi \times 745\,\mathrm{MHz}$, $\Delta'_{13} = 2\pi \times -2.2\,\mathrm{GHz}$ and $N_\mathrm{g} = 36\,\mu\mathrm{m}^{-3}$. The vertical dashed line shows the position of t_sat in the experimental signal.

We then fitted power law functions as with the experimental data and extracted the power law scalings, which are shown in Table 4.1 together with the experimental scalings. Concerning the scaling versus detuning, the fit was performed in a double logarithmic scale, because the two-photon resonance $\Delta'_{13} = 0$ is well defined in the theory. For the Rabi frequency, the scaling law $t_\mathrm{sat} \propto (\Omega_\mathrm{eff})^{-2}$ is actually exact. Because of the assumption of strong dephasing, $(\Omega_\mathrm{eff})^2$ is only present in the numerator of the transition rate in equation (4.14), and is therefore only a proportionality factor for the time axis.

4.3.3 Discussion

First the very good agreement for the scaling against the Rabi frequency is worth noticing. It validates the assumption of strong dephasing in the system, in spite of the dephasing mechanisms arising from motional effects which are essentially inhomogeneous (see chapter 3), on contrary to the dephasing actually included in the model. As for the absolute value t_sat, a comparison of the experimental signal with the simulated data (both potentials) is shown in Figure 4.8 (the actual shape of the signal will be discussed later). The position of the transmission minimum is well reproduced in the simulation with van-der-Waals interaction[15]. For the simulation with dipole-dipole

[15]This is in contradiction with [28], where these results were published. Here we have corrected a small numerical error in the calculation of the Rabi frequency which made it necessary to rescale the Rabi frequency in the paper.

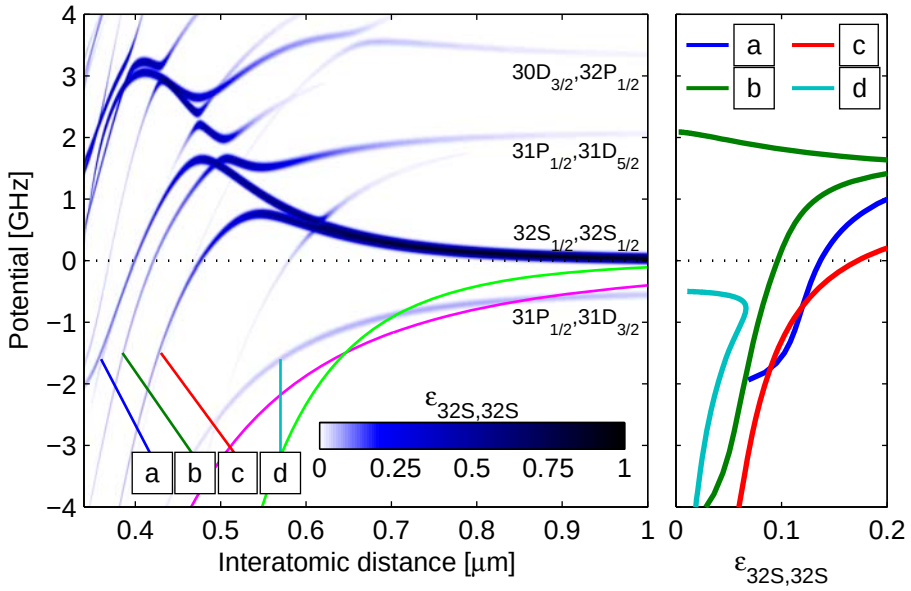

Figure 4.9: Left: Density plot of the 32S,32S admixture $\varepsilon_{32S,32S}$ as a function of the interatomic distance. The molecular quantum number here is $M = 0$ (i.e. $m_{j1} = \pm 1/2$ and $m_{j2} = \mp 1/2$), and interactions up to the quadrupole-quadrupole order are included [45]. The light green (resp. pink) line depicts the extrapolated van-der-Waals (resp. dipole-dipole) pair-state potential used in the simulation. [16] Right: Admixture of the 32S,32S pair state (horizontal axis) as a function of the interaction energy (vertical axis) for the four main potential curves at negative energies, as defined in the left panel. Line a and b correspond to two $30D_{3/2}, 32P_{1/2}$ pair states, line c to one $31P_{1/2}, 31D_{5/2}$ pair state and line d to one $31P_{1/2}, 31D_{3/2}$ pair state.

interaction there is a small discrepancy, as the excitation dynamics seem to be faster than in the experiment. We attribute this discrepancy to the long-range character of the dipole-dipole $1/r^3$ potential. We noticed that there is a dependence of t_{sat} on the system size in this case (the larger the system the faster the dynamics) and we assume that this effect is already present at the system size used here.

Overall the scaling laws and absolute values of t_{sat} in the experiment are compatible with both van-der-Waals and dipole-dipole interaction potentials in the aggregation model (although slightly better with the van-der-Waals interaction). It is also worth noticing that the results from both models differ very little, in spite of the very different scaling laws of the interaction potentials. The simulations therefore suggest a rather weak dependence on the actual shape of the interaction potential and that the basic mechanism of aggregation only relies on the existence of a facilitation radius, i.e. of an interaction potential and detuned interaction. This is *a posteriori* justifying the choice of considering very simplified interaction potentials compared to the actual very complex interaction potentials (see below).

[16] These interaction potentials were kindly provided by Donald Booth and James P. Shaffer, University of Oklahoma.

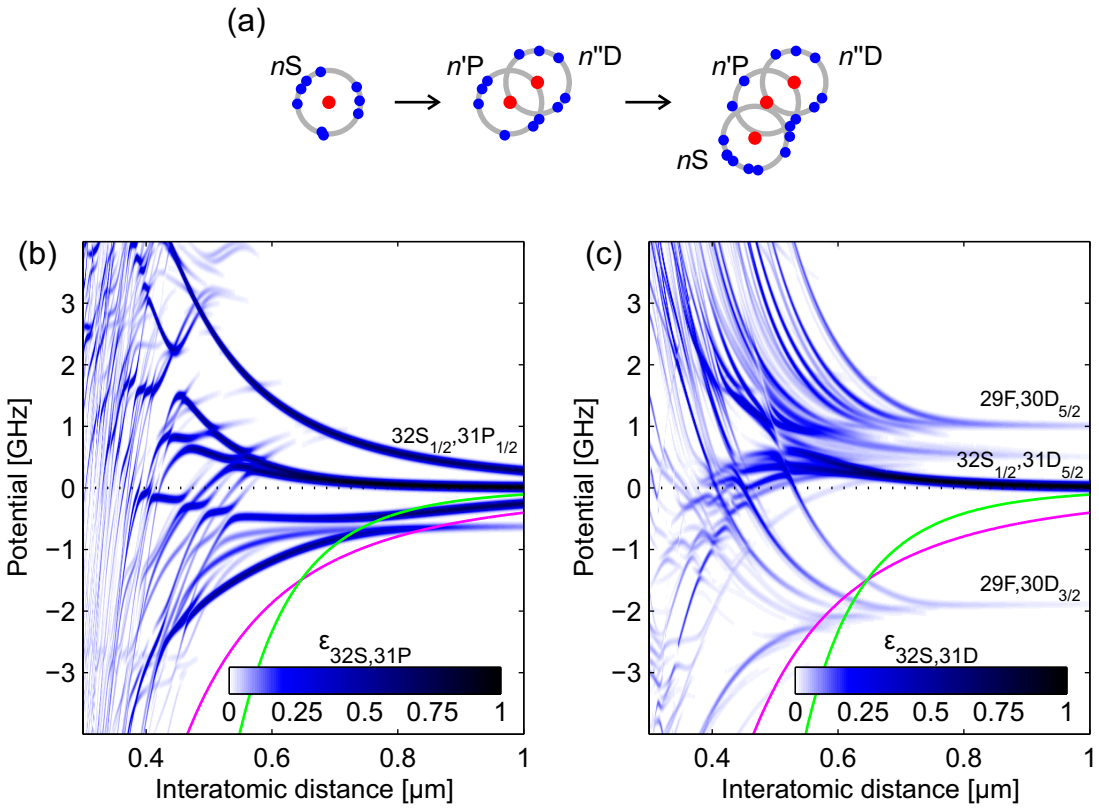

Figure 4.10: (a) Excitation sequence of three atoms, showing first the nS Rydberg atom, then the n'P-n''D pair, and the subsequent nS atom. Red (blue) dots represent Rydberg (resonant ground state) atoms, and the grey circles represent the simplified resonant shells of the individual atoms. (b) Interaction potentials around the $31P_{1/2}, 31D_{3/2}$ pair state. The $31P_{1/2}, 31D_{3/2}$ admixture $\varepsilon_{32S,31P}$ is depicted as a density plot. The molecular quantum number here is $M = 0$ (i.e. $m_{j1} = \pm 1/2$ and $m_{j2} = \mp 1/2$). Interactions up to the dipole-quadrupole order are included. The light green (resp. pink) line depicts the extrapolated van-der-Waals (resp. dipole-dipole) pair-state potential used in the simulation. (c) Same as (b) for the $31P_{1/2}, 31P_{1/2}$ pair.

Interaction potentials

As already mentioned, the observation of an excitation signal at negative detunings is made possible by state mixing with several molecular lines, which lead effectively to an attractive potential. We will focus on the 32S state for the following discussion, and we verified that the situation is similar for other states with principal quantum numbers. The admixture of the 32S,32S pair state $\varepsilon_{32S,32S}$ is shown again as a density plot in Figure 4.9, along with the admixture against the interatomic distance. For comparison purposes the effective interaction potentials used in the simulation are also shown. The agreement between the effective potentials and the real potentials is quite good at least for the $31P_{1/2}, 31D_{3/2}$ line.

The admixture of the 32S-32S pair state onto the molecular lines of pair states of the form n'P-n''D is made possible by the dipole-quadrupole interaction term which is weak but resonant (as discussed in section 1.3). The admixture $\varepsilon_{32S,32S}$ allows for the laser excitation from the $7P_{3/2}$ state, which would otherwise be dipole forbidden. The excitation of such a pair occurs on the basis of an atom in the 32S state. Once such a pair is created, it is actually mainly of the form n'P-n''D, with an amplitude of $1 - \varepsilon^2_{32S,32S} > 0.95$. For the subsequent excitation steps one has to consider the interaction potentials of the 32S state around such a pair. We can reduce this to binary interactions and consider the potentials for the 32S-n'P and 32S-n''D pair states. We have computed these interaction potentials, which are shown in Figure 4.10. The potentials for the S-D pair state shows a lot of state mixing because of the proximity of high angular momentum states. It is mostly repulsive with a rather small van-der-Waals interaction potential ($C_6^{\text{S-D}} \approx 2\pi \times 11\,\text{MHz} \cdot \mu\text{m}^6$), and does show some attractive components due to small state mixing, as for the 32S-32S pair state. For the S-P pair state the situation is quite different. An S-P pair is resonant with its permutation P-S, which is exactly the case of resonant dipole-dipole interaction with an interaction potential of the form C_3/r^3. Here there is one attractive branch with $C_3^{\text{S-P}} \approx 2\pi \times -242\,\text{MHz} \cdot \mu\text{m}^3$, which remains quite clear in spite of strong state mixing on other molecular lines. So for the excitation of the second atom in Figure 4.10(a) the excitation of a 32S-n'P pair is favored because it does not rely solely on the admixture of the 32S state.

It is nearly impossible to exactly include all the relevant states and interaction potentials in the aggregation model presented in section 4.3.1. However we have seen that the results of the model show very little sensitivity to the interaction potential (on the basis of two exemples). Nevertheless one aspect of the complex interactions needs to be discussed. The admixture $\varepsilon_{32S,32S}$ is actually the reducing the transition probability from one 32S atom to a n'P-n''D pair, such that the Rabi frequency should be rescaled by $\varepsilon_{32S,32S}$ exactly on this excitation step. Because of the nature of the aggregates, which enclose previously excited atoms, we can estimate that at most every second excitation is performed via this process. For the other excitation possibilities (direct off-resonant excitation from the ground state or around a 31P atom), the Rabi frequency does not require to be rescaled. An attempt to include these would be to rescale the Rabi frequency by a factor of $(\varepsilon_{32S,32S})^{1/2} \approx 0.3$, and therefore rescale the time axis by $(\varepsilon_{32S,32S})^{-1} \approx 10$ in the simulation results from Figure 4.8. This however does not seem to be necessary. A precise account of the effect of the admixture would require further study.

Signal form

One striking difference between the experimental and simulated results is the shape of the transmission signal, both at small times (the simulated signals show a sharp jump at $t = 0$) and in the temporal width of the signal. The origin of the sharp jump has been identified to be an artifact of the model [20]. The single excitations at small times are independent of the environment because there is no Rydberg interaction yet. Thus

they retain some quantum nature such that the transmission change should start at zero.

Additionally the way in which the dephasing was included in the model may explain the discrepancy in the signal form. The actual broadening in the experiment is caused by the Doppler effect (with a Gaussian profile) and the transit time broadening caused by the motion through the resonant shell. Determining the actual line profile of the transit time broadening is very complex, as it depends on the profile of the resonant region [18] and has to be integrated over the velocity distribution. It is however neither Gaussian nor Lorentzian (as for Γ_k in equation (4.14)). In order to gain some insight into this we modified the model by modifying *ad hoc* the transition rate Γ_k from a Lorentzian shape to a (pseudo-)Voigt profile. For this we first determined a Voigt profile, ensuring that the width of the profile and the integrated profile are the same than the Lorentzian profile. This ensures that the width of the resonant shell and the total rate around a single Rydberg atom are conserved. In order to limit the computational effort the Voigt profile was approximated by a pseudo-Voigt profile (defined as the sum of a Lorentzian and a Gaussian profile). The pseudo-Voigt profile was optimized to the Voigt profile by ensuring the following conditions: the value at large detuning, the center value, the width and the integrated value are the same for the Voigt and pseudo-Voigt profile. Note that this modification of the model is not formally justified to account for the experimental situation in the model.

The results of the simulation with a Lorentzian profile and a pseudo-Voigt profile (for the same parameters and van-der-Waals interaction) are shown in Figure 4.11. There is a clear difference between both line profiles at $t = 0$. The reason is that the signal at small times is essentially given by the excitation rate at large detunings, which is larger with a Lorentz profile because it does not converge to zero as fast as a Voigt profile. Hence the more pronounced jump at $t = 0$. The different line profile however does not seem to provoke a narrowing of the transmission signal.

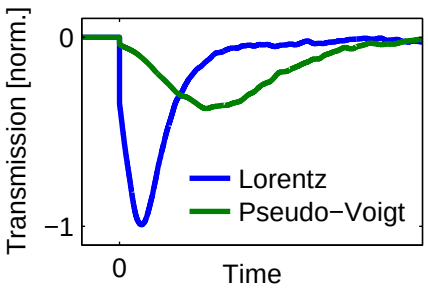

Figure 4.11: Comparison of the model with a Lorentzian and a pseudo-Voigt line profile.

In Figure 4.8 the small overshoot in the experimental signal before the system reached the steady-state (at $t \approx 40\,\mathrm{ns}$) is also not reproduced by the theoretical model. Remnants of coherent Rabi oscillations can be ruled out given the large dephasing rates and large detunings with respect to the single atom resonance.

Overall, explaining all these small discrepancies would require a much more involved theoretical treatment which would have to include the atomic motion, the real interaction potentials and probably the full quantum treatment of the Liouville-von Neumann equation for multiple atoms. It is even remarkable that the rather simple model of a frozen gas presented here can account so well for the physics happening in the rather "dirty" environment of a vapor cell. These results are complementary to the previous

work on Rydberg aggregates in cold atoms [10, 11] as it demonstrates the validity of the theoretical framework over very different range of parameters.

Finally, in the following we will address two aspects that do not prove crucial in the understanding of the physics, but provide some valuable insight.

Spatial correlations

The fundamental takeaway of the comparison between the aggregation theory and the experimental results is that facilitated excitation, as shown in Figure 4.6(a) is occuring. The formation of aggregates with the spatial correlations is a corollary of the facilitated excitation, because the excitations are favored at a specific distance from Rydberg atoms. In a frozen gas of atoms, as is the case in the theoretical model, these aggregates are long-lived. In the experiment however the atoms move around very fast, which makes the spatial correlations vanish.

We can still try to make an estimation of how large aggregates can be before the spatial correlations disappear. For this we consider the situation used for the simulation with van-der-Waals interaction. The time scale defining a "frozen gas" in this situation is the time spent by the atoms inside the resonant shell, given by $t_\mathrm{f} = (\gamma_\mathrm{TT})^{-1} \approx 0.32\,\mathrm{ns}$. In order to estimate the size of the aggregates that can be formed during this time, i.e. the number of subsequent excitations around the same position, or around the same seed atom, we use a simplified model. The experimental parameters are the following: 32S state , $\Omega_{12} = 2\pi \times 166\,\mathrm{MHz}$, $\Omega_{23} = 2\pi \times 745\,\mathrm{MHz}$, $\Delta'_{13} = 2\pi \times -2.2\,\mathrm{GHz}$ and $N_\mathrm{g} = 88\,\mu\mathrm{m}^{-3}$ (as in Figure 4.3). This gives for the aggregation model $C_6 = 2\pi \times -109\,\mathrm{MHz}\cdot\mu\mathrm{m}^6$ and $\gamma_{13}^\mathrm{vdW} = 2\pi \times 711\,\mathrm{MHz}$.

Let us first consider the one seed atom around which the aggregate will be formed. The resonant shell is a sphere of radius $r_\mathrm{fac} = 0.65\,\mu\mathrm{m}$ and width $\Delta r^\mathrm{vdW} = 51\,\mathrm{nm}$, which contains $\nu_{res} = N_\mathrm{g} \times 4\pi r_{fac}^2 \Delta r = 20.7$ atoms in average. As further atoms are excited in an aggregate, the size of the resonant shell grows. If we approximate an aggregate containing n atoms to a sphere whose volume is the volume occupied by n atoms separated by the facilitation radius, the entire shell of the n-atom aggregate contains $n^{2/3} \times \nu_{res}$ atoms. The excitation rate of one atom in the resonant shell is $\Gamma_{r_\mathrm{fac}} = \Omega_\mathrm{eff}^2/\gamma_{13} \approx 2\pi \times 3.5\,\mathrm{MHz}$ and therefore the excitation rate of the (n)-th atom of an aggregate is $\Gamma_n = (n-1)^{2/3} \times \nu_{res}\Gamma_{r_\mathrm{fac}}$. We define the probabilities $P_n(t)$ that aggregates of n atoms has formed around the seed atom at the time t. Under the assumption that the atoms are excited one by one, at each time an n aggregate can be formed from an $(n-1)$-aggregate with a rate $\Gamma_{n-1}P_{n-1}(t)$, and an n-aggregate can become a $(n+1)$-aggregate with a rate $\Gamma_n P_n(t)$, such that the total probability is conserved ($\sum_n P_n = 1$). The probabilities $P_n(t)$ obey the following ensemble of equations:

$$\begin{aligned}\partial_n P_n &= \Gamma_{n-1}P_{n-1} - \Gamma_n P_n \\ &= \nu_{res}\Gamma_{r_\mathrm{fac}}\left((n-1)^{2/3}P_{n-1} - n^{2/3}P_n\right)\end{aligned} \tag{4.27}$$

n	1	2	3	4	5	6
$P_n(t_\mathrm{f})$	0.86	0.12	0.014	0.0014	0.00012	0.000010
η_n	4490	636	72	7.1	0.64	0.054

Table 4.2: Probabilities $P_n(t_\mathrm{f})$ of creating an n-atom aggregate in an interval t_f and typical number of n-atom aggregates η_n for $N_\mathrm{fac} = 5000$ facilitating atoms, similarly to the experimental situation.

This ensemble equations can be solved numerically. In Table 4.2 the probabilities $P_n(t_\mathrm{f})$ of having an aggregate consisting of up to 6 atoms after the flying time t_f of the atom through the shell are listed.

The number of n-atom aggregates that are formed during the time t_f during which the gas can be considered to be frozen is given by $\eta_n = N_\mathrm{fac} \times P_n(t_\mathrm{f})$, where N_fac is the number of Rydberg atoms which can act as seeds. There are eventually 50000 Rydberg atoms excited in our medium. Assuming that these atoms form a sphere of density $N_\mathrm{sat} = r_\mathrm{fac}^{-3}/2$, the outer shell of this sphere contains $N_{fac} \approx 5000$ atoms. The estimation of the number of n-atom aggregates for our experimental configuration η_n is listed in Table 4.2. Here we can see that in each experimental run up to approx. one aggregate consisting of 5 atoms is formed.

These estimations are performed under the most strict assumptions because of the definition of t_f with the width of the resonant shell. In reality the spatial correlations probably tend to decay from a density-density correlation function as shown in Figure 4.6(c) to unity over a longer time. If for instance we define $t_\mathrm{f} = \frac{\langle v_\perp \rangle}{r_\mathrm{fac}/2}$, the time needed for an atom to travel over half the facilitation radius, the spatial correlations would not be completely washed out. For this critical time we obtain that aggregates of up to 10 atoms with somewhat weaker correlations would be formed in the experiment.

Effect of charges

Because of the loose binding energy of the electron in a Rydberg state (see Table 1.1), Rydberg atoms is susceptible to become ionized, for instance through collisions. Collisionnal ionization of Rydberg atoms has been a tool to measure the population of Rydberg states [71], to the expense of additional decoherence on the order of 50 MHz. It was also found that ionization tends can occur as an avalanche process, resulting in the ionization of all Rydberg atoms and the creation of a plasma [72, 73]. Because ionization mechanisms can have such dramatic effects on Rydberg atoms, it is necessary to examine how it can have an influence in the present experiment.

Let us first consider the effect of single charge on the aggregation mechanism. The electric field produced by a single charge (Cs^+ ion or electron) is given by Coulomb's law ($E_\mathrm{C}(r) = e/(4\pi\epsilon_0 r^2)$). At a distance $r_\mathrm{fac} = 0.65\,\mu$m the electric field is $E_\mathrm{C}(r_\mathrm{fac}) = 34\,\mathrm{V/cm}$. As shown in Figure 1.1, at this electric field strength the Stark effect for the

32S state of cesium is still very well described by the quadratic Stark effect. Then the energy shift exerted by the charge onto the Rydberg state is given by

$$\begin{aligned} V_{\mathrm{C}}(r) &= \frac{1}{2}\alpha_{32\mathrm{S}}E(r)^2 \\ &= \frac{\alpha_{32\mathrm{S}}}{2}\left(\frac{e}{4\pi\epsilon_0}\right)\frac{1}{r^4} \end{aligned} \tag{4.28}$$

where r is the distance between the charge and the Rydberg atom and $\alpha_{32\mathrm{S}}$ is the polarizability of the 32S state. $V_{\mathrm{C}}(r)$ is a potential energy shift of the form C_4/r^4 with $C_4 = 2\pi \times -214\,\mathrm{MHz}\cdot\mu\mathrm{m}^4$ and $V_{\mathrm{C}}(r_{\mathrm{fac}}) = 2\pi \times -1190\,\mathrm{MHz}$. This potential shift has a similar form and amplitude to the van-der-Waals and dipole-dipole potentials that were extracted from the experimental data. In other words a charge generates an interaction potential on the Rydberg states that is very similar to the interaction between Rydberg atoms and therefore also allows for facilitated excitation.

If charges would be present in the excitation volume before the infrared laser is shone on, it would allow for direct resonant excitation because of the potential $V_{\mathrm{C}}(r)$. The requirement for off-resonant excitation would be lifted and the excitation dynamics would be very fast [74]. Therefore the number of charges initially is limited.

The full ionization of the Rydberg atoms during the aggregation process can only occur once Rydberg atoms have been excited. From [72] the time scale for the transition of an ensemble of Rydberg atoms to a plasma is approximately 100 ns, i.e. in our experimental conditions at $t \approx t_{\mathrm{sat}} + 100\,\mathrm{ns}$. Therefore it is not a factor in the experiments presented above.

5 Microwave Modulation of Rydberg States

Transitions between Rydberg states have typically very large electric dipole moments. On the other hand is the energy spacing much smaller and therefore are Rydberg atoms very sensitive to DC and AC electric fields. In the special case of oscillating electric field in the radio-frequency (RF) to microwave (MW) range, i.e. from 1 MHz to 100 GHz, spectroscopy of Rydberg atoms can be used to measure the strength of the electric field in a very precise way [30, 31, 75], and is even callibration free as all relevant paramters can be calculated from first principles. If a non-resonant RF field is applied, side bands appear in the atomic spectrum through the interaction between the Rydberg atoms and the electric field, which can be resolved spectroscopically via the measurement of the EIT spectrum in a vapor cell [76]. In the experiments described in this chapter the goal is to make use of the resulting modulation of the amplitude of the excitation light field when passing through a vapor cell, a quantity that is averaged out in previous experiments involving Rydberg atoms in MW electric fields. One goal is to study how the modulation of the Rydberg gas by an RF field leads to side bands in the optical field, similar to the electro-optical effect in an EOM (electro-optical modulator). In addition this method provides a new way to probe the properties of a driven Rydberg gas. A quite special case can be reached when the modulation frequency reaches the classical Kepler frequency of the electron in a Rydberg state (which is the transition frequency between two Rydberg states), new physics might appear, maybe in relation to ponderomotive forces in modulated optical lattices [77]. But this will not be studied here. Overall one might label this section with the question: How fast can a Rydberg atom follow an applied AC-field?

In the first section we describe the theoretical framework for the description of the modulation of a light field by the interaction between Rydberg atoms and an oscillating field. The experimental realization and first measurements are presented in the second section.

5.1 Theoretical aspects

5.1.1 Periodic Hamiltonian

We consider an atom that can be described as a three level system in a ladder configuration, as shown in Figure 5.1, driven by two light fields as described in section 2.2,

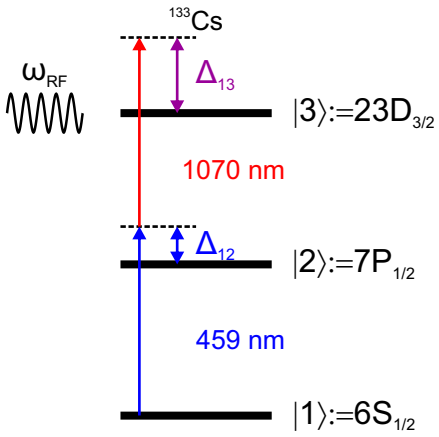

Figure 5.1: Energy level diagram for the excitation to the Rydberg state $|3\rangle$ in the presence of an oscillating electric field of frequency ω_{RF}.

where the excited state is a Rydberg state. An oscillating electric field is applied in the medium, of the form

$$\boldsymbol{E}_{\mathrm{RF}}(t) = E_{\mathrm{RF}}(t)\underline{\boldsymbol{\epsilon}}_{\mathrm{RF}} = E_{0,\mathrm{RF}}\cos(\omega_{\mathrm{RF}}t)\underline{\boldsymbol{\epsilon}}_{\mathrm{RF}} \tag{5.1}$$

where ω_{RF} is the angular frequency, $E_{0,\mathrm{RF}}$ is the electric field amplitude and $\underline{\boldsymbol{\epsilon}}_{\mathrm{RF}}$ is the unit vector of the polarization of the electric field[1]. We assume that the modulation frequency is much smaller than the transition frequencies of any dipole-allowed transition involving the three states. Also the electric field amplitude is supposed to be small enough such that the Stark shift of the excited (Rydberg) state is quadratic. The Stark shift associated with the ground and intermediate state can be neglected because of their very small polarizability. Then, following equation (1.6), the effect of the electric field on the system is a Stark shift of the Rydberg level which is given as

$$\begin{aligned}\mathcal{E}^{(2)}_{|3\rangle} &= \frac{1}{2}\alpha_{|3\rangle}E^2_{0,\mathrm{RF}}\cos^2(\omega_{\mathrm{RF}}t)\\ &= \frac{\Delta_{\mathrm{RF}}}{2} + \frac{\Delta_{\mathrm{RF}}}{2}\cos(2\omega_{\mathrm{RF}}t)\end{aligned} \tag{5.2}$$

where

$$\Delta_{\mathrm{RF}} = \frac{1}{2}\alpha_{|3\rangle}E^2_{0,\mathrm{RF}}$$

Here $\alpha_{|3\rangle}$ is the polarizability of the Rydberg state and Δ_{RF} is the amplitude of the Stark energy shift. Because of this energy shift of the Rydberg state the Hamiltonian of the system changes to

$$\tilde{H}(t) = \hbar\begin{pmatrix} 0 & \frac{1}{2}\Omega_{12} & 0 \\ \frac{1}{2}\Omega^*_{12} & -\Delta_{12} & \frac{1}{2}\Omega_{23} \\ 0 & \frac{1}{2}\Omega^*_{23} & -\Delta_{13} + \frac{\Delta_{\mathrm{RF}}}{2} + \frac{\Delta_{\mathrm{RF}}}{2}\cos(2\omega_{\mathrm{RF}}t)\end{pmatrix} \tag{5.3}$$

[1]In the following the light fields and the oscillating electric field have the same polarization such that the quantization axis is not modified by the electric field.

which is periodic in time, of period $T = \frac{\pi}{\omega_{\mathrm{RF}}}$. As shown in [78], in the presence of decoherence ($\hat{L}(\tilde{\rho}) \neq 0$) the density matrix $\tilde{\rho}(t)$ of this system converges at large time to a periodic pseudo steady state of the same period as the the Hamiltonian

$$\tilde{\rho}(t) \underset{t\to+\infty}{=} \tilde{\rho}(t+T) \tag{5.4}$$

5.1.2 Simulation method

In order to compute the pseudo steady-state of the system we follow the method presented in [78], which we will summarize in the following.

Let us re-write the density matrix as a vector, defined for instance as

$$\boldsymbol{\rho}(t) = \begin{pmatrix} \tilde{\rho}_{11}(t) \\ \tilde{\rho}_{12}(t) \\ \vdots \\ \tilde{\rho}_{33}(t) \end{pmatrix} \tag{5.5}$$

The conservation of the population for $\boldsymbol{\rho}(t)$ is given by

$$\hat{n}\boldsymbol{\rho}(t) = 1 \quad \text{with} \quad \hat{n} = \begin{pmatrix} 1 & 0 & 0 & 0 & 1 & 0 & 0 & 0 & 1 \end{pmatrix} \tag{5.6}$$

The Liouville-von Neumann equation (2.5) is a linear differential equation for the elements of the density matrix. Thus it can be written for $\boldsymbol{\rho}(t)$ as

$$\frac{\partial \boldsymbol{\rho}(t)}{\partial t} = \hat{\Lambda}(t)\boldsymbol{\rho}(t) \tag{5.7}$$

where $\hat{\Lambda}(t)$ is a linear operator, which is determined by $\tilde{H}(t)$ and the Lindblad operator of the system $\hat{L}$. This linear operator is also periodic in time ($\hat{\Lambda}(t) = \hat{\Lambda}(t+T)$). Equation (5.7) is integrable, and the result of the integration can be written in the following general form using the propagator $\hat{A}(t_2, t_1)$, which is determined by $\hat{\Lambda}(t)$:

$$\boldsymbol{\rho}(t_2) = \hat{A}(t_2, t_1)\boldsymbol{\rho}(t_1) \tag{5.8}$$

and in particular

$$\boldsymbol{\rho}(t+T) = \hat{A}(t+T, t)\boldsymbol{\rho}(t) \tag{5.9}$$

At large time $\boldsymbol{\rho}(t)$ is periodic (5.4), so equation (5.9) becomes

$$\boldsymbol{\rho}(t) = \hat{A}(t+T, t)\boldsymbol{\rho}(t) \tag{5.10}$$

In order to determine the propagator, which only needs to be determined over one period, the time interval corresponding to one period $[t_0, t_0 + T]$ is split in N intervals ($t_N = t_0 + N$). The number of intervals is determined so that in each sub-interval

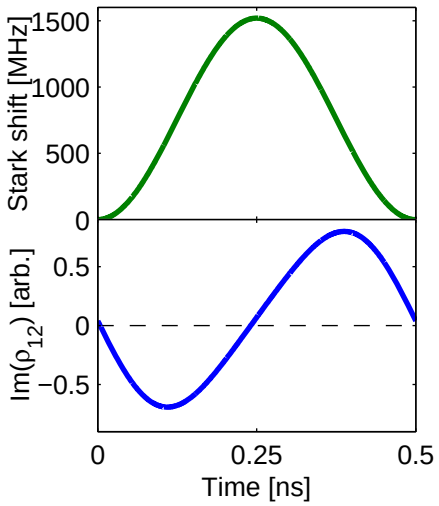

Figure 5.2: Simulation of $\mathrm{Im}(\tilde{\rho}_{12}(t))$ (lower panel) over one period of the electric field modulation ($\mathcal{E}^{(2)}_{|3\rangle}(t)$, upper panel). The modulation is $\omega_{\mathrm{RF}} = 2\pi \times 1000\,\mathrm{MHz}$ and $\Delta_{\mathrm{RF}} = 2\pi \times 1520\,\mathrm{MHz}$. The parameters are $\Omega_{12} = 2\pi \times 12.6\,\mathrm{MHz}$, $\Omega_{23} = 2\pi \times 1240\,\mathrm{MHz}$, $\Delta_{13} = 2\pi \times 0\,\mathrm{GHz}$, $\Gamma_{21} = 2\pi \times 1.18\,\mathrm{MHz}$ and $\Gamma_{\mathrm{TT}} = 2\pi \times 5\,\mathrm{MHz}$.

$[t_{k-1}, t_k]$ the linear operator can be approximated to a constant value $\hat{\Lambda}(t) \approx \hat{\Lambda}(t_{k-1})$. Over each interval the integration of equation (5.7) yields

$$\hat{A}(t_{k-1}, t_k) = e^{(t_k - t_{k-1})\hat{\Lambda}(t_{k-1})}$$

and thus

$$\hat{A}(t_0, t_k) = \prod_{m=1}^{k} e^{(t_m - t_0)\hat{\Lambda}(t_{m-1})} \tag{5.11}$$

which is the propagator over the discretized interval. By solving the system of equations (5.6)-(5.9) at any t_0 and using equations (5.8) and (5.11) one can determine the full density matrix of the pseudo steady state.

5.1.3 Simulation results

In Figure 5.2 we show the result of the numerical computation of the pseudo steady state of the imaginary part of the coherence $\tilde{\rho}_{12}(t)$ (observable in the experiment). This atomic response is essentially a sinusoidal signal with a frequency $2\omega_{\mathrm{RF}}$. In the following we will consider only the complex valued amplitude of the Fourier component at the frequency $2\omega_{\mathrm{RF}}$, defined as

$$s(2\omega_{\mathrm{RF}}) = 2 \int_{t_0}^{t_0+T} \mathrm{Im}(\tilde{\rho}_{12}(t)) e^{-2\omega_{\mathrm{RF}} i t}\, \mathrm{d}t \tag{5.12}$$

The experiment that will be described below in more detail is performed in a vapor cell at room temperature. Thus the averaging over the Doppler velocity classes has to

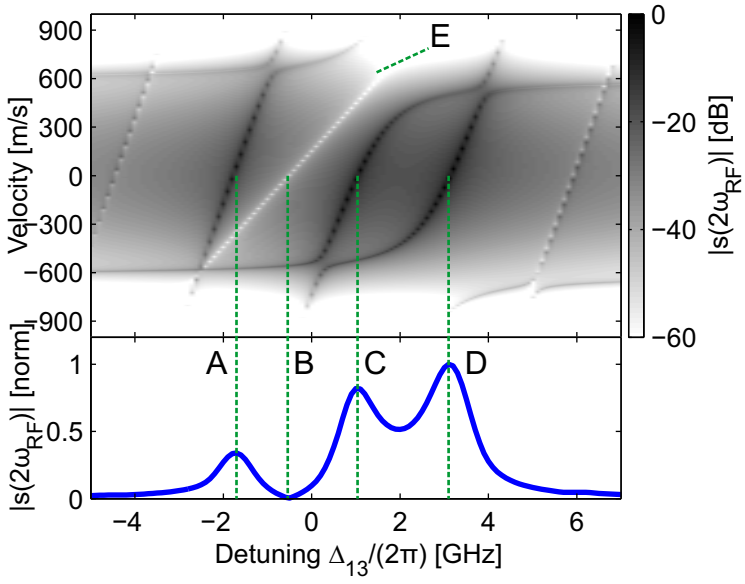

Figure 5.3: Amplitude of the Fourier component at $2\omega_{\mathrm{RF}}$. The upper panel shows the amplitude $|s(2\omega_{\mathrm{RF}})|$ (normalized to the maximum value) as a density plot against the detuning and the parallel velocity of the atoms $v_{\parallel}$. The lower panel is the integration over the Doppler velocity distribution. The parameters for the simulation are: $\omega_{\mathrm{RF}} = 2\pi \times 1318\,\mathrm{MHz}$, $\Delta_{\mathrm{RF}} = 2\pi \times 1520\,\mathrm{MHz}$, $\Omega_{12} = 2\pi \times 12.6\,\mathrm{MHz}$, $\Omega_{23} = 2\pi \times 1240\,\mathrm{MHz}$, $\Gamma_{21} = 2\pi \times 1.18\,\mathrm{MHz}$ and $\Gamma_{\mathrm{TT}} = 2\pi \times 5\,\mathrm{MHz}$. The wave vectors of the light fields are $k_{\mathrm{L},12} = +2\pi/459\,\mathrm{nm}$, $k_{\mathrm{L},23} = -2\pi/1070\,\mathrm{nm}$. The labels and the green dashed lines highlight features that are discussed in the main text.

be performed. In Figure 5.3 the absolute value of the Fourier component $s(2\omega_{\mathrm{RF}})$ is shown when the detuning to the Rydberg state is varied, against the atomic velocity and integrated over the atomic velocity. Three peaks of modulation can be seen at $\Delta_{13} \approx 2\pi \times -1700\,\mathrm{MHz}$ (labeled A), $2\pi \times 1000\,\mathrm{MHz}$ (labeled C) and $2\pi \times 3100\,\mathrm{MHz}$ (labeled D). In the density plot these peaks correspond to resonances that show an almost linear dependence between Δ_{13} and $v_{\parallel}$ with a slope of $(k_{\mathrm{L},12} + k_{\mathrm{L},23})^{-1}$. This linear behavior corresponds exactly to the additional two-photon detuning due to the Doppler effect given by: $(k_{\mathrm{L},12} + k_{\mathrm{L},23})v_{\parallel}$ (see section 3). The separation between these three resonances is consistent with $2\omega_{\mathrm{RF}} = 2\pi \times 2636\,\mathrm{MHz}$.

The avoided crossing visible at $\Delta_{13} \approx 2\pi \times 1500\,\mathrm{MHz}$ and $v_{\parallel} \approx 600\,\mathrm{m/s}$ (labeled E) arises from the coupling between the one photon resonance on the lower transition ($v_{\parallel} = \Delta_{12}/k_{\mathrm{L},12}$) and the two-photon resonance between the ground state and the Rydberg state.

Moreover the amplitude of the modulation vanishes at $\Delta_{13} \approx 2\pi \times -500\,\mathrm{MHz}$ (labeled B). This feature is visible in the density plot also with a linear behavior with a slope of $(2k_{\mathrm{L},12} + k_{\mathrm{L},23})^{-1}$.

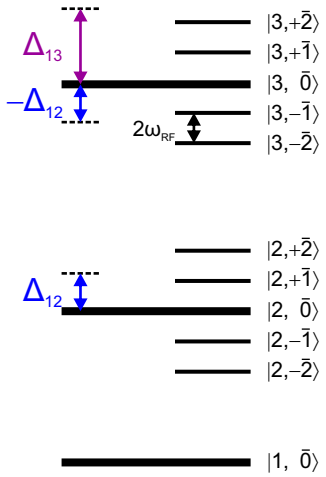

Figure 5.4: Schematic representation of the Floquet manifolds $|i, \bar{n}\rangle$, where i represents the unperturbed atomic state and $\bar{n}$ represents the number of RF photon pairs dressing the atomic state.

Floquet transitions

In order to explain the three modulation peaks and the point where the amplitude vanishes one needs to introduce a new theoretical framework where the RF electric field dresses the atomic levels in terms of so-called Floquet states. Since the Hamiltonian is periodic in time the solution of the Schrödinger equation can be expressed as a linear combination of periodic pseudo eigen-solutions. This is called the Fourier-Floquet method [79–82]. The system can be described in an basis of pseudo eigenstates called Floquet states $|i, \bar{n}\rangle$ in a similar manner than dressed states in the quantum electrodynamics formalism, where the for the same i the states $|i, \bar{n}\rangle$ are separated by $2\omega_{\mathrm{RF}}$. $\bar{n}$ can be seen as the number of RF photon pairs exchanged with the oscillating electric field. The relevant Floquet states are shown schematically in Figure 5.4.

In the present case the detuning to the intermediate state is fixed. The two outer peaks of the signal in Figure 5.3 represent the resonant two-photon transitions to a Floquet state with a non-vanishing number of photon pairs $|1, \bar{0}\rangle \rightarrow |2, \bar{n}\rangle \rightarrow |3, -\bar{1}\rangle$ (at $\Delta_{13} \approx 2\pi \times -1700\,\mathrm{MHz}$, labeled A) and $|1, \bar{0}\rangle \rightarrow |2, \bar{n}\rangle \rightarrow |3, +\bar{1}\rangle$ (at $\Delta_{13} \approx 2\pi \times 3100\,\mathrm{MHz}$, labeled D). In those cases there is a net detuning of $\pm 2\omega_{\mathrm{RF}}$ which is compensated by the absorption or emission of a pair of RF photons from the oscillating electric field. Including the velocity component, the resonance condition here yields $v = (\Delta_{13} \pm 2\omega_{\mathrm{RF}})/(k_{\mathrm{L},12} + k_{\mathrm{L},23})$. This fits to the slope observed in the density plot of Figure 5.3.

The central modulation feature in Figure 5.3 (labeled C) sits at an almost vanishing two-photon detuning to the Rydberg state. The qualitative explanation is the following. Due to the non-vanishing detuning to the intermediate state (assumed positive here) the transition $|1, \bar{0}\rangle \rightarrow |2, +\bar{1}\rangle \rightarrow |3, \bar{0}\rangle$ is favored with regard to $|1, \bar{0}\rangle \rightarrow |2, -\bar{1}\rangle \rightarrow |3, \bar{0}\rangle$

because both single transitions are closer to resonance. This favored transition includes the exchange of a pair of photons, and therefore a modulation on the light field. The two-photon resonance condition yields here $v = \Delta_{13}/(k_{\mathrm{L},12} + k_{\mathrm{L},23})$, which also matches the slope of the feature at $\Delta_{13} = 2\pi \times 1000\,\mathrm{MHz}$ and $v = 0$ in Figure 5.3 (labeled C).

Finally the vanishing modulation (labeled B) happens when the condition $\Delta_{13} = -\Delta_{12}$. Here two two-photon transitions need to be considered.

- $|1, \bar{0}\rangle \rightarrow |2, \bar{0}\rangle \rightarrow |3, -\bar{1}\rangle$ with a detuning Δ_{12} on the lower transition and a two-photon detuning of $2\omega_{\mathrm{RF}} - \Delta_{12}$
- $|1, \bar{0}\rangle \rightarrow |2, +\bar{1}\rangle \rightarrow |3, \bar{0}\rangle$ with a detuning $-2\omega_{\mathrm{RF}} + \Delta_{12}$ on the lower transition and a two-photon detuning of $-\Delta_{12}$

These transitions have exact opposite detunings, therefore the phase factor associated to them oscillates with opposite phase and the modulation of the light field due to these two transitions interferes destructively. Alternatively, these transitions involve $+\bar{1}$ and $-\bar{1}$ pairs of RF photons, which cancel each other.

This qualitative argumentation does not take into account the coupling of the light fields on the original unperturbed atomic levels, which give rise to the avoided crossings in Figure 5.3 (as at label E). These avoided crossings explain the slight deviation of the position of the peaks from being exactly separated by $\pm 2\omega_{\mathrm{RF}}$. A more careful treatment of the system in the Floquet basis allows to take these couplings into account. It also gives a better explanation for the central peak which arises from state mixing between Floquet states caused by the light fields and the oscillating electric field. More details about this can be found in [79–82].

5.2 Experimental realization

In this section we first show how the RF electric field is applied to the atoms confined in a millimeter-sized vapor cell. Then we discuss how the data is obtained. Finally we present the experimental results, which are compared with results from the simulation, and discuss in the end the prospects of this approach to electro-optics via Rydberg states for future work.

5.2.1 RF Modulation

The scope of the experiments presented in this chapter is to study the back-action on the light field from the high frequency electric field modulation of Rydberg states. Here high frequency refers to at least several GHz. At a frequency of 1 GHz, the vacuum wavelength is already as small as 30 cm, which is on the order of the size of the experimental setup presented here. At such high frequencies extra care has to be taken in the design of the electrical circuits guiding the RF electric field to avoid damping and reflections.

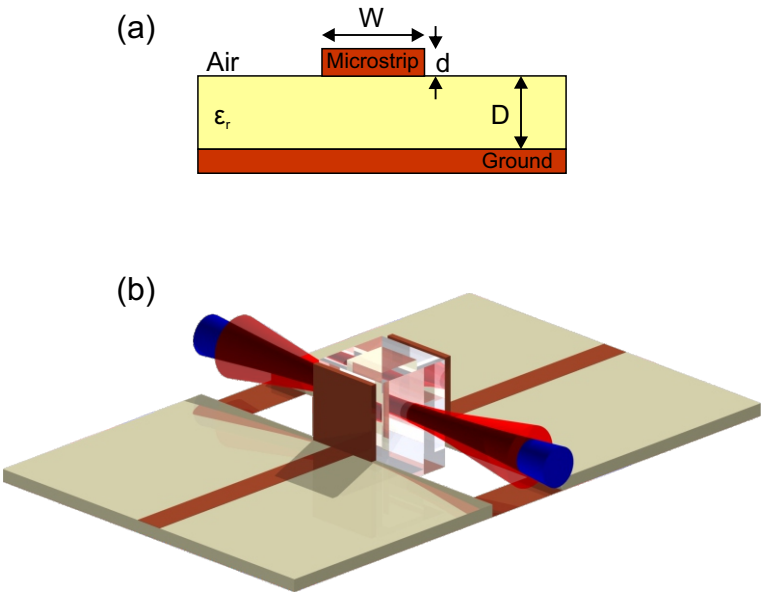

Figure 5.5: (a) Definitions of dimensions of a microstrip waveguide. The dielectric in the middle has a relative permittivity ε_r. (b) Sketch of the PCB with the glass cell, as simulated. The laser beams are shown for illustrative purposes.

Applying a electric field to a certain region of space is usually performed by a pair of electrodes, one of which receiving a electromagnetic (voltage) signal while the other is electrically grounded. The pair of electrodes amounts to a capacitor with a capacity C and the impedance of this capacitor is given by $Z = 1/iC\omega$, where ω is the frequency of the electric field applied. If ω or C are small enough the signal is fully reflected at the electrode, ensuring a maximal potential difference and electric field amplitude between the electrodes. The second requirement for a maximal electric field amplitude is that the signal is fully transferred from the source (with its internal impedance, here $Z_0 = 50\,\Omega$) to the electrode. For this the impedance of the transmission lines has to be matched to that of the source, which ensures maximal transmission of the electromagnetic signal, very much like index matching in the optical domain.

PCB board

The goal here is to apply an oscillating electric field with a frequency of up so several GHz from the outside of a glass cell. The glass cell used here has an outer section of $5.7\,\mathrm{mm} \times 5.7\,\mathrm{mm}$ and an inner section of $3\,\mathrm{mm} \times 3\,\mathrm{mm}$. The glass cell is positioned between two square electrodes with a section of approx. $5\,\mathrm{mm} \times 5\,\mathrm{mm}$ separated by a distance $a = 6\,\mathrm{mm}$, made out of $200\,\mu$m-thick copper sheets. One electrode is grounded with a matched $50\,\Omega$ termination. For maximal transmission from the source of the RF electromagnetic field to the electrodes, the source is connected to the electrodes via a microstrip waveguide printed circuit board (PCB) (see Figure 5.5(a)) which is designed with a characteristic impedance Z_PCB of $50\,\Omega$. A view of the PCB, with the electrodes and the glass cell in-between, is shown in Figure 5.5(b). The PCB with the

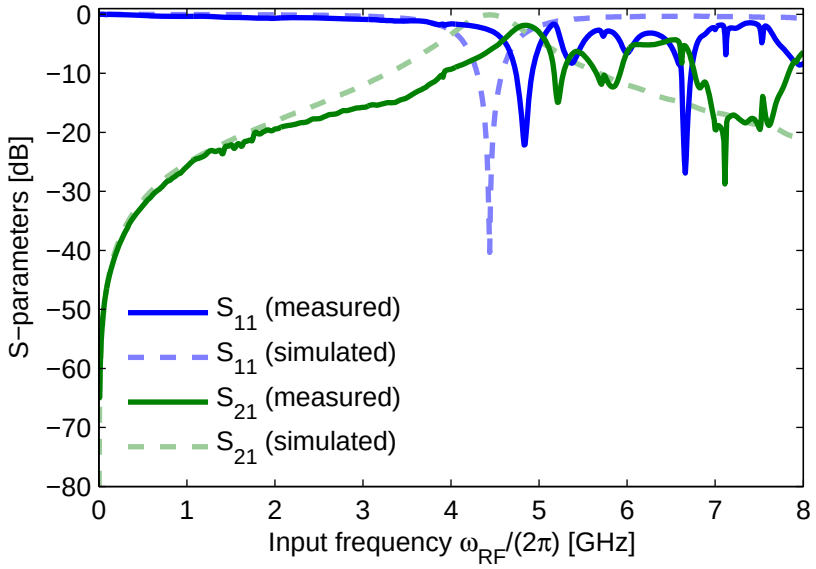

Figure 5.6: S-parameters for the input used in the experiment, measured and simulated.

simple microstrip waveguide is cut in the middle, where the cell is placed. The two electrodes are connected (in practice soldered) to each stripline end on both sides of the cell. The PCB was etched from a substrate with a copper layer of thickness $d = 17\,\mu$m on both sides of a dielectric material of thickness $D = 0.81\,$mm and relative dielectric permittivity $\varepsilon_\mathrm{r} = 3.38$. The outer dimensions of the PCB are $30\,\mathrm{mm} \times 25\,\mathrm{mm}$. SMA connectors are connected to the two outer ends of the microstrip.

The characteristic impedance Z_PCB of the microstrip waveguide is a complex function of d, D, ε_r and the width of the stripline W (as defined in Figure 5.5(a)) [83, 84]. In order to characterize Z_PCB and the properties of the response of the PCB was simulated in the program CST Studio Suite. The 3D model is exactly the one depicted in Figure 5.5(b), that is including a cut-out section of the glass cell. The characteristic impedance computed by CST is $Z_\mathrm{PCB} = 50.3\,\Omega$, in very good agreement with the design impedance of $50\,\Omega$.

Additionally the standard set of quantities to be measured is called the S-parameters. Here our PCB has two so-called ports, one at each end of the microstrip waveguide, in which a signal can be sent or received. The S-parameters describe the returned signal on each port when a signal is sent into one of the ports, i.e. S_{ij} is the ratio of the signal received at the port i by the signal sent at port j. For our PCB with two ports 1 and 2 with port 2 having a matched termination, S_{11} is the fraction of the signal that is reflected back to port 1, and S_{21} is the fraction of the signal that is transmitted from port 1 to port 2. These S-parameters can be simulated in CST and measured with a vector network analyzer[2] in the actual experimental configuration. The simulated and measured S_{11} and S_{21} are shown in Figure 5.6. The agreement between measurement and simulation is very good at rather low frequency, up to a transmission resonance

[2]Rohde & Schwarz ZVL13

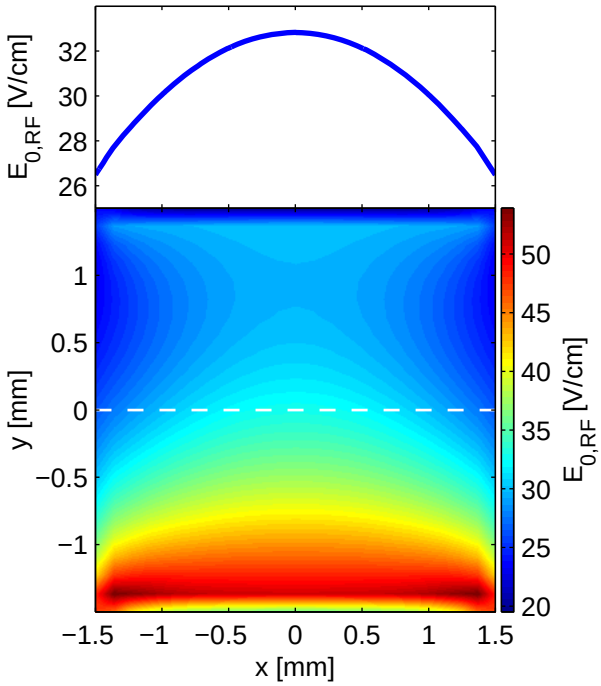

Figure 5.7: Simulated distribution of the amplitude of the electric field $E_{0,\mathrm{RF}}$ inside the cell as a 2D density plot (lower panel) and as a cut in the middle of the cell (upper panel), where the laser field passes through (white dashed line in the density plot). Over the path of a laser through the cell, the electric field variation is sufficiently flat to be considered constant. The frequency of the RF field is $\omega_{\mathrm{RF}} = 2\pi \times 100\,\mathrm{MHz}$.

visible at $\omega_{\mathrm{RF}} = 2\pi \times 4.8\,\mathrm{GHz}$. In particular S_{11} being close to unity and S_{21} very small corroborates the fact that the electromagnetic wave is reflected at the first electrode. In the simulation the position of this resonance depends on the outer dimensions of the PCB. Above this frequency the wavelength become smaller than the size of the PCB, inducing unwanted geometry constrained resonance effects.

Electric field generation

The RF electric field is generated by a signal generator (Rohde & Schwarz SMY02 or Windfreak SynthUSBII) connected to a high power amplifier (Mini-Circuits ZHL-1-2W+ or ZHL-5W-422+). The maximum frequency for these components is 4.4 GHz. The output power of the amplifier is set to 1 W with an uncertainty of $\sim 0.3\,\mathrm{W}$ by measuring in with a Spectrum Analyzer (Hameg HMS3000 or Anritsu MS2668C). The amplifier is connected to the PCB via a 1 m long low-loss coaxial cable. Because there is full reflexion at the electrode, the transmission line from the amplifier to the electrode has an open end. In this case the voltage at the open end is given by [83]

$$V_{\mathrm{E}} = 2V_{\mathrm{A}} \cos\left(\frac{\omega_{\mathrm{RF}} l}{v}\right) \tag{5.13}$$

where l is the length of the transmission line v is the propagation velocity of the electromagnetic wave in the transmission line and V_{A} is the output voltage of the amplifier. Therefore the maximum voltage at the electrode is only obtained for $\omega_{\mathrm{RF}} = \frac{2\pi n v}{l}$, where n is an integer. The propagation velocity is complex to determine, but the set of RF frequencies for which the voltage at the plate is maximum could be determined by maximizing two quantities: (i) the radiated power from the transmission line and (ii) the measured modulation signal.

For a power of 1 W the output voltage of the amplifier is of the form $V_{\mathrm{E}} = V_0 \cos(\omega_{\mathrm{RF}} t)$ with $V_0 = 10\,\mathrm{V}$. Using the equation above and the amplitude of the oscillating electric field between the electrodes is roughly given by

$$E_{0,\mathrm{RF}} \approx \frac{2V_0}{a} = 33\,\mathrm{V/cm} \tag{5.14}$$

where $a = 6\,\mathrm{mm}$ is the distance between the electrodes. The actual spatial distribution of the electric field can be obtained from CST, and is shown in Figure 5.7 for the inner part of the cell, at a frequency of $\omega_{\mathrm{RF}} = 2\pi \times 100\,\mathrm{MHz}$. In the middle of the cell, where the lasers are adjusted, is in very good agreement with the rough estimation. The small discrepancy arises from the finite size of the electrodes. It is also interesting to note that the electric fields exceeds the estimated values at other positions. This is a consequency of having the back plane of the PCB, which is grounded, very close to the electrodes which increases the electric field. The presence of the glass cell also has an influence on the electric field distribution because of the high relative dielectric permittivity $\varepsilon_{\mathrm{r}} = 3.8$, which tends to localize the electric field. Because the electric field is not constant over the cell and the alignment of the beams cannot be guarantied to pass through the cell at the middle point, the estimated value for the electric field amplitude $E_{0,\mathrm{RF}} \approx 33\,\mathrm{V/cm}$ is a good approximation.

Moreover we found through simulations that the electric field amplitude becomes smaller at larger frequency, up to a factor 5 at 4 GHz. We also found that the voltage difference between the electrodes becomes smaller, which means that the electromagnetic wave is not perfectly reflected at the electrode at large frequencies. One possible explanation for this is that the electrodes behave more and more as antennas as the wavelength becomes on the order of their dimension, thus reducing the optimal reflection of the electromagnetic wave. Nevertheless we will first neglect this effect in the following simulations, and then discuss its possible implications.

Overall this type of printed circuit board allows for applying RF fields with a frequency of up to $\omega_{\mathrm{RF}} = 2\pi \times 4.5\,\mathrm{GHz}$. Improvements in the bandwidth could be obtained by adding an impedance matching of $50\,\Omega$ very close to the electrodes. This would possibly reduce the parasite resonances visible in Figure 5.6. It would also allow for a perfect transmission of the electromagnetic wave to the electrode; and the electrode would effectively perform a measurement of the voltage at the impedance matching. The influence of the back plane could also be reduced by etching the metallic layer before the electrode, possibly improving the electric field homogeneity. And finally possible antenna-like behavior may be reduced by using smaller geometries.

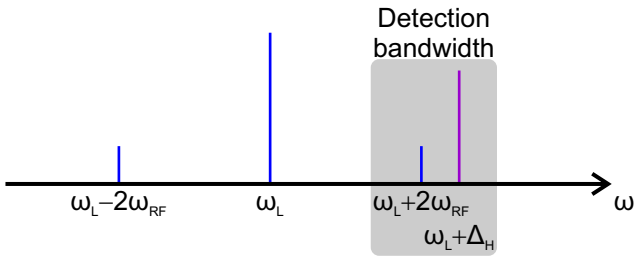

Figure 5.8: Schematic power spectrum against frequency of the modulated light (in blue) and of the heterodyne beam (in violet). The bandwidth of the detector only allows for the detection of the beating between the two components on the right.

5.2.2 Measurement scheme

Heterodyne detection

As discussed in section 5.1 the theory predicts that the imaginary part of the coherence $\tilde{\rho}_{12}$ contains oscillating components with frequencies that are multiples of $2\omega_{\mathrm{RF}}$ (we will focus exclusively on the $2\omega_{\mathrm{RF}}$ component). From equations (2.21) and (2.25) the electric field of the laser driving the lower transition carries the same modulation after passing through the cell. Because of the limitations of the PCB, the uppermost frequency of the modulation on the amplitude of the light field is $2\omega_{\mathrm{RF}} = 2\pi \times 9\,\mathrm{GHz}$. As we want also to detect very small modulations at very large frequencies we cannot just rely on ordinary photo-diodes.

In order to circumvent this limitation we use a second laser that has a well defined frequency detuning Δ_{H} with regard to the modulated light field of frequency ω_{L}. Such a measurement method is called heterodyning, and is a very common technique in quantum optics to measure small electric field amplitudes. The frequency detuning is chosen such that $|\Delta_{\mathrm{H}} - 2\omega_{\mathrm{RF}}|$ is smaller than the bandwidth of the detector. The signal that is detected then contains modulation terms only associated to the mixing between one modulation side band and the heterodyne light field, and is background-free. The power spectrum of the modulated light field with the two modulation side bands is shown schematically in Figure 5.8, together with the power spectrum of the heterodyne laser.

More formally the electric fields of the modulated lasers can be written as

$$\begin{aligned} \boldsymbol{E}_{\mathrm{L}}(t) &= E_{\mathrm{L}}(t)\underline{\boldsymbol{\epsilon}}_{\mathrm{L}} = E_{0\mathrm{L}}\left[1 + A_{\mathrm{mod}}\cos\left[2\omega_{\mathrm{RF}}t\right]\right]\cos\left[\omega_{\mathrm{L}}t\right]\underline{\boldsymbol{\epsilon}}_{\mathrm{L}} \\ \boldsymbol{E}_{\mathrm{H}}(t) &= E_{\mathrm{H}}(t)\underline{\boldsymbol{\epsilon}}_{\mathrm{H}} = E_{0\mathrm{H}}\cos\left[(\omega_{\mathrm{L}} + \Delta_{\mathrm{H}})t\right]\underline{\boldsymbol{\epsilon}}_{\mathrm{H}} \end{aligned} \tag{5.15}$$

where A_{mod} is the strength of the modulation. By ensuring that the two light fields have the same polarization, the signal detected by the photo detector is proportional

to the square of the sums of the electric fields, which is given by

$$\begin{aligned}(E_{\mathrm{L}}(t)+E_{\mathrm{H}}(t))^2 = \frac{1}{2}\Big\{ & E_{0\mathrm{L}}^2 + E_{0\mathrm{L}}^2 A_{\mathrm{mod}}^2 + E_{0\mathrm{H}}^2 \\ & + 2E_{0\mathrm{L}}^2 A_{\mathrm{mod}} \cos\left[2\omega_{\mathrm{RF}} t\right] + E_{0\mathrm{L}} E_{0\mathrm{H}} \cos\left[\Delta_{\mathrm{H}} t\right] \\ & + E_{0\mathrm{L}} A_{\mathrm{mod}} E_{0\mathrm{H}} \left[\cos\left[(\Delta_{\mathrm{H}} + 2\omega_{\mathrm{RF}})t\right] + \cos\left[(\Delta_{\mathrm{H}} - 2\omega_{\mathrm{RF}})t\right]\right] \\ & + E_{0\mathrm{L}}^2 A_{\mathrm{mod}}^2 \cos\left[4\omega_{\mathrm{RF}} t\right] + \text{fast oscillating terms} \Big\} \end{aligned} \tag{5.16}$$

where the fast oscillating terms are oscillating with multiples of the optical frequency ω_{L}. Considering the small bandwidth of the photodetector, only the following terms remain:

$$\begin{aligned}(E_{\mathrm{L}}(t)+E_{\mathrm{H}}(t))^2 \,|_{\mathrm{PD}} = \frac{1}{2}\Big\{ & E_{0\mathrm{L}}^2 + E_{0\mathrm{L}}^2 A_{\mathrm{mod}}^2 + E_{0\mathrm{H}}^2 \\ & + E_{0\mathrm{L}} A_{\mathrm{mod}} E_{0\mathrm{H}} \cos\left[(\Delta_{\mathrm{H}} - 2\omega_{\mathrm{RF}})t\right] \Big\} \end{aligned} \tag{5.17}$$

where the only oscillating component is the beating between one side band and the heterodyne light field.

Besides this frequency conversion of the modulation, the other advantage of the heterodyne detection method is that the measured signal is isolated from cross-talk parasite signals of the oscillating electric field on the photodetector.

Experimental setup and measurement procedure

The lasers and the frequency stabilization and calibration methods used for the experiment described in this section are the same as in section 4.1.

For the experiment described here the excitation scheme is shown in Figure 5.1. The ground state is the $6\mathrm{S}_{1/2}, \mathrm{F} = 3$ state and the intermediate state $7\mathrm{P}_{1/2}, \mathrm{F}' = 4$. The Rydberg state is $23\mathrm{D}_{3/2}$, in order to make use of the polarizability of D-states, which is much larger than for S-states (see Figure 1.1(c)). The choice of the $7\mathrm{P}_{1/2}$ intermediate state has the advantage of greatly simplifying the level structure of the Rydberg state: only the level with $J = 3/2$ can be optically addressed and the two $|m_j|$ sublevels have polarizabilities of the same sign. Because both lasers are linearly polarized, the larger coupling from the ground state occurs to the sublevels of the Rydberg state with $|m_j| = 1/2$. Therefore we will restrict ourselves to these sublevels, whose polarizability is $\alpha_{23D3/2,1/2} = 2.79\,\mathrm{MHz/(V/cm)^2}$. The amplitude of the energy shift with 1 W of input RF power is (using equation (5.2))

$$\Delta_{\mathrm{RF}} = 2\pi \times 1520\,\mathrm{MHz} \tag{5.18}$$

The detuning of the blue laser (at 459 nm) is kept constant at $\Delta_{12} = 2\pi \times 1300\,\mathrm{MHz}$, and its Rabi frequency is set to $\Omega_{12} = 2\pi \times 12.6\,\mathrm{MHz}$. The detuning to the Rydberg

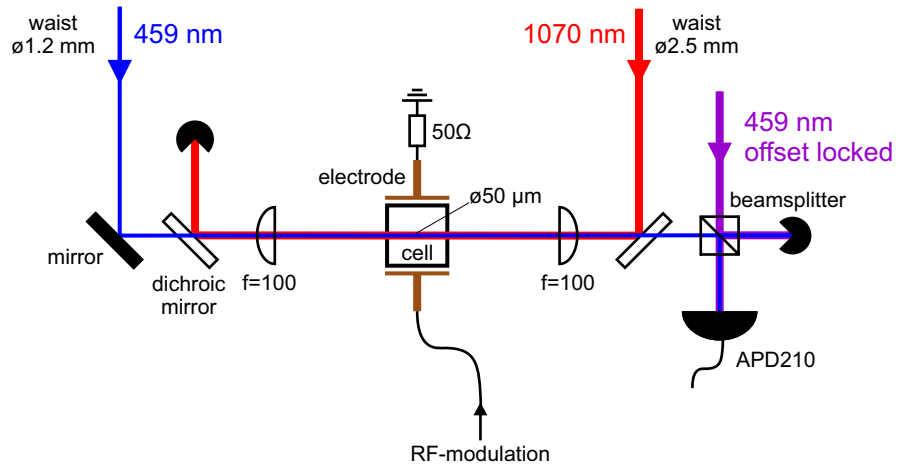

Figure 5.9: Schematic representation of the optical setup. The cell is quadratic with a inside width of 3 mm.

state Δ_{13} is scanned over approx. 15 GHz around the resonance, and the Rabi frequency of this laser is $\Omega_{23} = 2\pi \times 1240\,\mathrm{MHz}$.

A schematic representation of the optical setup is shown in Figure 5.9. The blue laser is collimated to a diameter of 1.2 mm ($1/e^2$ diameter), and the infrared to a diameter of $\sim 2.5\,\mathrm{mm}$. Both lasers are overlapped in a counter-propagating manner with dichroic mirrors and focused with 100 mm lenses to a diameter of $50\,\mu\mathrm{m}$. The Rayleigh rage of the infrared beam is 1.8 mm, which ensures an almost homogeneous longitudinal profile of the laser beams at the focus within the cell. Both lasers are horizontally polarized. The blue beam is then sent to the photodetector after passing through a non-polarizing beamsplitter. The photodetector[3] is an avalanche photodiode amplified with an effective gain of $2.5 \times 10^4\,\mathrm{V/W}$ at 459 nm and a 3 dB upper bandwidth of 1 GHz.

The heterodyne laser is a self built[4] diode laser in an external cavity configuration. Both lasers are sent onto a fast photodiode (8 GHz bandwidth), and the beat signal of the two lasers is digitally phase locked to a reference signal [85]. The detuning of the heterodyne laser to the original blue laser Δ_H can be as large as 7.2 GHz. It is set such that $|\Delta_\mathrm{H} - 2\omega_\mathrm{RF}| = 2\pi \times 100\,\mathrm{MHz}$, which is inside the bandwidth of the photodetector.

The cell that is used in the experiment is 3 mm long[5] and connected to a cylindrical reservoir where a drop of metallic cesium sits. It was fabricated similarly to the cell described in section 4.1. It is surrounded by the PCB placed at the focus such that the electric field between the electrodes is perpendicular to the laser beams. In this configuration the polarization of the laser beams is the same as the one of the RF field,

[3] APD210 from Menlo Systems
[4] The diode laser is a Nichia NDBA116T.
[5] 101.015-QS from Hellma Analytics

which simplifies the definition of the quantization axis. Both the PCB and the cell are placed inside an oven heated at 160°C to ensure that there is no cesium condensation in the cell. The reservoir is heated separately to a temperature of 120°C (except when mentioned differently), such that the ground state density[6] is $N_g = 22\,\mu\text{m}^{-3}$.

The measurement was performed as follows. First the RF frequency is set, as well as the corresponding detuning of the heterodyne laser such that $\Delta_{12} = 2\pi \times 1300\,\text{MHz}$. The infrared laser is scanned very slowly (100 s) over the resonance to the Rydberg state. As the infrared laser is scanning, a fast oscilloscope records multiple snapshots of the the beatnote signal (from equation (5.17)) for $1\,\mu$s with a sampling rate of $5\,\text{GS/s}$ and a bandwidth of 200 MHz. Additionally an independent EIT signal to the Rydberg state, the signal controlling the detuning ramp and the signal of the infrared through a Fabry-Pérot resonator are recorded.

The frequency axis is calibrated using the signal from the Fabry-Pérot resonator, and the resonance position of the upper transition ($\Delta_{23} = 0$) is determined from the EIT signal to obtain the values for Δ_{23}. The two-photon detuning is here simply determined as $\Delta_{13} = \Delta_{12} + \Delta_{23}$. The amplitude of the modulation $s(2\omega_{\text{RF}})$, the observable in this experiment, is performed by performing a Fourier transformation of every $1\,\mu$s long beatnote signal around the frequency $|\Delta_{\text{H}} - 2\omega_{\text{RF}}| = 2\pi \times 100\,\text{MHz}$ ($\pm 10\,\text{MHz}$) and averaged. It can be seen for one set of parameters in Figure 5.10(b). Note that the background signal at ~ 0.75 is the noise floor of the signal, caused by the photon shot noise on the photodetector.

5.2.3 Results and interpretation

The results of the measurements at various modulation frequencies are shown in Figure 5.10. First the maximum modulation frequency at which a modulation signal could be observed is $\omega_{\text{RF}} = 2\pi \times 3.6\,\text{GHz}$. This maximum value corresponds roughly to all the maximum bandwidths of the electronics in the setup (heterodyne lock, RF generation/amplification and PCB).

The amplitude of the intensity modulation on the blue laser is found to be in the range of $10^{-6} - 10^{-4}$, depending on the modulation frequency. The modulation amplitude expected from the simulations and equation (2.25) is supposed to be around 500 times larger[7].

[6] Here the density is estimated from the vapor pressure [59]. An accurate measurement in the experimental conditions is not necessary as no quantitative analysis involving the density will be performed.

[7] Note that in previous work on time-resolved excitation of Rydberg atoms in vapor cells [13, 17], although the shape of the signal matched the theoretical expectations, the amplitude of the transmitted signal was a fit parameter and no quantitative comparison was performed between theory and experiment. There is therefore no baseline measurement on the amplitude of the transmitted signal that verifies the theoretical prediction from equation (2.25).

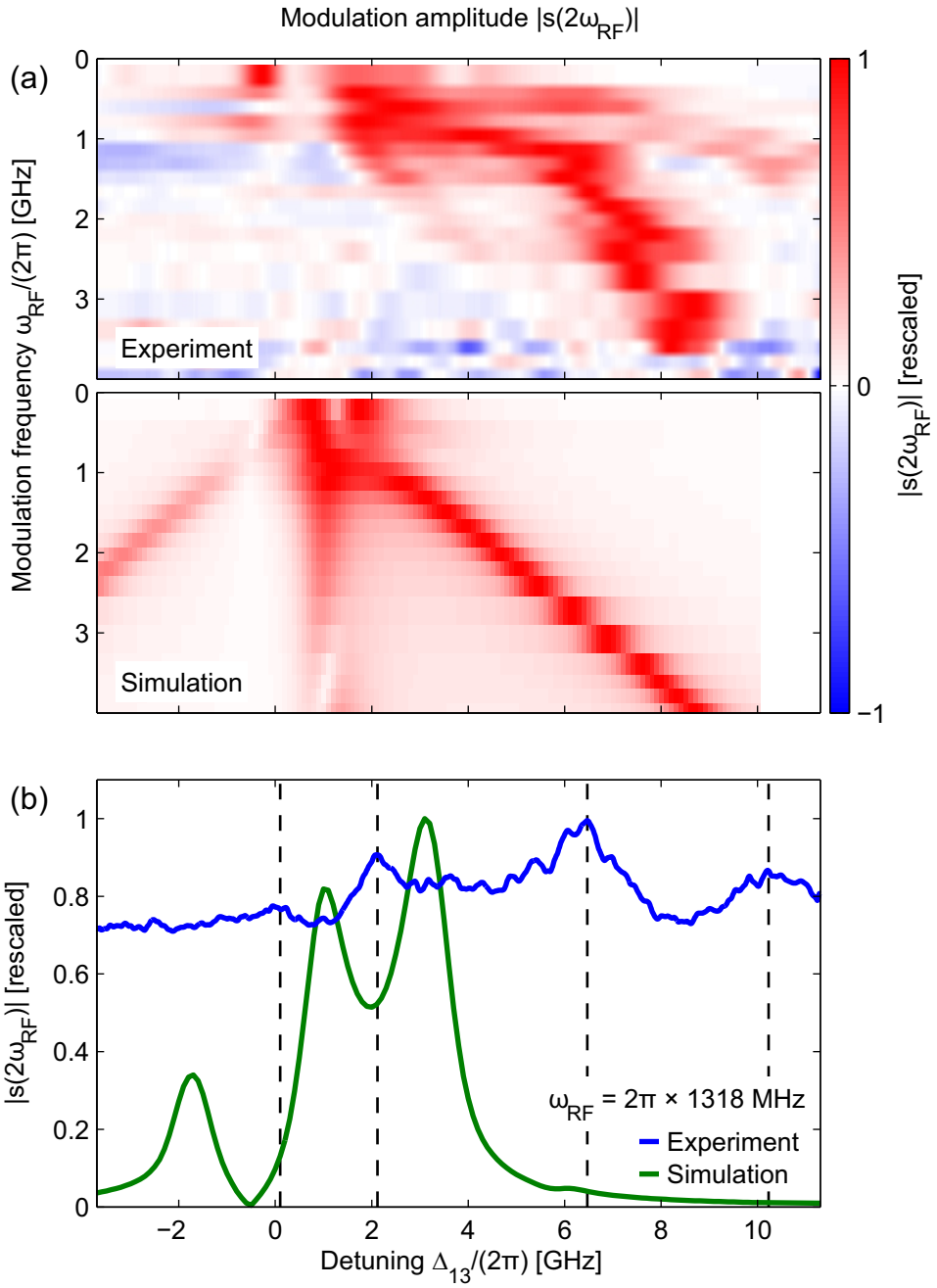

Figure 5.10: (a) Density plots of the modulation amplitude of the transmission of the blue laser $|s(2\omega_{\mathrm{RF}})|$ as a function of the modulation frequency ω_{RF} and the two-photon detuning Δ_{13}, measured (top) and simulated (bottom). The data is rescaled to the maximum of the signal for each detuning scan, and the noise floor is substracted. The parameters are: $\Delta_{12} = 2\pi \times 1300\,\mathrm{MHz}$, $\Omega_{12} = 2\pi \times 12.6\,\mathrm{MHz}$, $\Omega_{23} = 2\pi \times 1240\,\mathrm{MHz}$, $\Delta_{\mathrm{RF}} = 2\pi \times 1520\,\mathrm{MHz}$, $N_{\mathrm{g}} = 22\,\mu\mathrm{m}^{-3}$. (b) Modulation amplitude at $\omega_{\mathrm{RF}} = 2\pi \times 1318\,\mathrm{MHz}$, measured and simulated. Both traces are rescaled to their maximum signal. The black dashed lines in the background highlight the positions of modulation maxima in the measured signal.

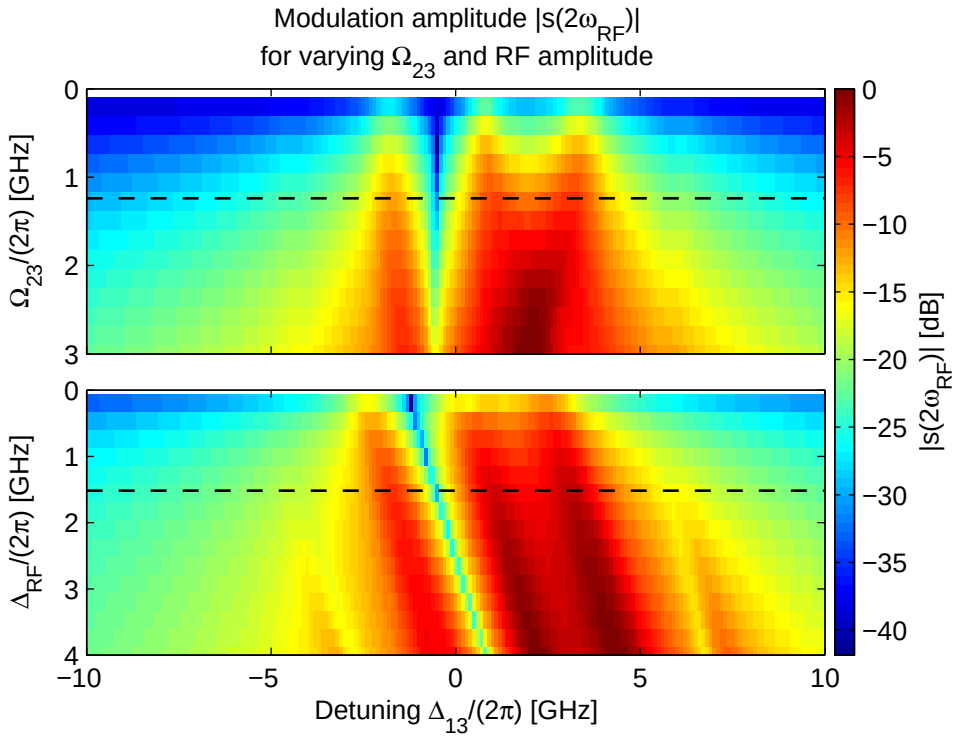

Figure 5.11: Density plots of the simulated modulation amplitude $|s(2\omega_r mRF)|$ as a function of the two-photon detuning Δ_{13} and the Rabi frequency of the upper transition Ω_{23} (top) and the amplitude of the energy shift Δ_{RF}. The data is rescaled to the maximum of the signal for each detuning scan and the color scale is logarithmic. The black dashed lines display the position of the signal in Figure 5.10(b). The parameters for the simulation are: $\Delta_{12} = 2\pi \times 1300\,\mathrm{MHz}$, $\Omega_{12} = 2\pi \times 12.6\,\mathrm{MHz}$, $\Omega_{23} = 2\pi \times 1240\,\mathrm{MHz}$ (except for the upper panel), $\Delta_{\mathrm{RF}} = 2\pi \times 1520\,\mathrm{MHz}$ (except for the lower panel), $\Gamma_{21} = 2\pi \times 1.18\,\mathrm{MHz}$ and $\Gamma_{\mathrm{TT}} = 2\pi \times 5\,\mathrm{MHz}$.

Regarding the detuning dependence of the signal, it is clear that the simulation do not match the results of the experiment, but several features can be highlighted. In Figure 5.10(a) there is one dominant branch of modulation maxima in both the experiment and the simulation. Their detuning position increase with the modulation frequency, although not linearly in the experiment. Several satellite feature can be identified in the measured signal, but it is not possible to match them to the satellite maxima from the simulation. The modulation amplitudes are plotted for $\omega_{\mathrm{RF}} = 2\pi \times 1318\,\mathrm{MHz}$ in Figure 5.10(b), where it is clear that the positions of the signal maxima in the experiment do not match the expected positions from the simulation. Moreover the spacings between these maxima is not consistent with $2\omega_{\mathrm{RF}}$, as the simulations predict (see section 5.1). Overall there seems to be some kind of an inhomogeneous shift and distortion of the signal in the experiment.

Let us now analyze possible explanations for these discrepancies. Because of the Gaussian profile of the laser beams, the Rabi frequencies are not constant inside the cell. In order to gain insight into the influence of this, we performed simulations at various

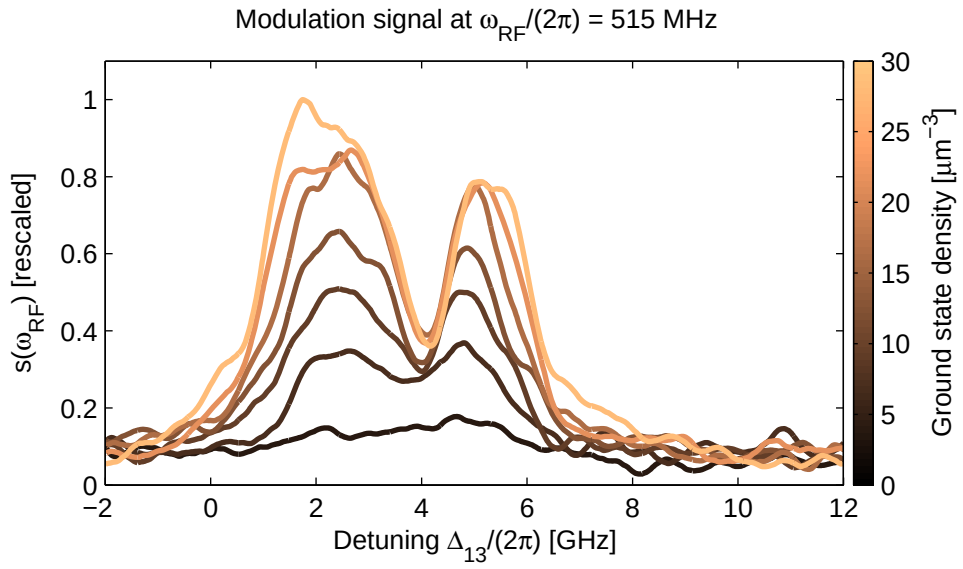

Figure 5.12: Modulation amplitude at different ground state atomic densities N_g. The color code of each curve depicts the value of the ground state density. The parameters are $\omega_{RF} = 2\pi \times 515\,\mathrm{MHz}$, $\Delta_{12} = 2\pi \times 1300\,\mathrm{MHz}$, $\Omega_{12} = 2\pi \times 12.6\,\mathrm{MHz}$, $\Omega_{23} = 2\pi \times 1240\,\mathrm{MHz}$, $\Delta_{RF} = 2\pi \times 1520\,\mathrm{MHz}$.

Rabi frequencies of the infrared laser Ω_{23} (see Figure 5.11). We find that the shape of the modulation signal only varies slightly and at Rabi frequencies that are significantly larger than the experimental value. Also no significant shift of the signal is observed. Then, as seen in Figure 5.7 the electric field is not homogeneous inside the cell. In order to understand the possible influence of this inhomogeneity we carried out simulations for different values of the Stark energy shift Δ_{RF} (see Figure 5.11). The modulation signal is overall shifted as $\Delta_{RF}/2$, which is due to the quadratic Stark shift in equation (5.2). Additionally for higher electric fields two satellite modulation maxima appear at large positive and negative detunings, which might explain why mostly more than three features are visible in Figure 5.10. However the spacings between the peaks always remains constant at approx. $2\omega_{RF}$, hence the distortions observed cannot be explained by inhomogeneities of the electric field alone.

The maximum population of the Rydberg state is approx. 1 % in the simulation for the parameters of Figure 5.10(b). Combined with the ground state density, the estimated density of Rydberg atoms is $N_{ryd} = 0.22\,\mu\mathrm{m}^{-3}$. At such high densities an intrinsic optical bistability arises due to inter-atomic interactions [27, 86]. Although the origin of the underlying interaction remains unknown, it has necessarily a repulsive component in the present case. Indeed van-der-Waals interaction for D-states is mostly repulsive [39], dipole-dipole interaction has both repulsive and attractive components (see section 1.3), the polarizability is positive for D-states (for the interaction between Rydberg atoms and charges, see sections 1.2 and 4.3). The distortions and shifts that we observe in the modulation signal are to larger detunings, which fits to a repulsive interaction. The intrinsic optical bistability, as an interaction effect between the atoms, in strongly dependent on the atomic density. We performed a series of

measurements at various atomic densities. The results are shown in Figure 5.12. We found that the modulation increases almost linearly with the density, as expected from equation (2.25). Interestingly, apart from a small modification of the ratio between the two peaks, there is no significant distortion or shift of the signal as the density is increased.

Finally if some interaction effect due to the presence of charges is relevant here, it is possible that the motion of the free electrons in the oscillating electric field needs to be taken into account. Much like a plasma, the effect of the motion of the electrons would be frequency-dependent and might lead to the distortions that we observe, and to a shielding, which explains the amplitude of the modulation being much smaller than expected from the simulations. A full understanding of these effects in our system will require further investigation.

Summary and Outlook

Summary and outlook

The work discussed in this thesis describes two separate experiments, both of them concerning the excitation of cesium atoms to Rydberg states in a vapor cell above room temperature. A common point was to explore the excitation dynamics in ranges of parameters that remained unexplored to date. In particular the choice of the atomic species combined with the unusual excitation scheme allowed for driving atomic transitions with continuous wave lasers and still achieving high Rabi frequencies. This is necessary in order to counteract the broadening induced by the Doppler effect, and in our case to achieve densities of Rydberg atoms that are relatively large. In one experiment we made use of the strong and very complex interactions between Rydberg atoms, which allowed for correlated excitation dynamics at large detunings. In the second experiment the Rydberg excitation was performed in the presence of a high-frequency oscillating electric field. By making use of the sensitivity of Rydberg atoms to external fields, the modulated energy shift of the Rydberg state induced by the electric field could be mapped on the intensity of a transmitted light field.

Overall the use of vapor cells allowed for the observation of already known phenomena, but in an environment that is small and offers a potential for integration [14,87]. These specific experimental conditions offered new insight into the physics of the excitation of Rydberg atoms at large bandwidth.

Let us now for each the experiments described in this thesis summarize the results and discuss future prospects.

Rydberg aggregation

Time-resolved measurement of the excitation dynamics to Rydberg states were performed in a vapor cell, using a two-photon excitation scheme with a large detuning to the intermediate state. The atomic densities N_g ranging from $10\,\mu\text{m}^{-3}$ to $500\,\mu\text{m}^{-3}$ much larger compared to previous results in thermal vapor [17, 27, 88] and non-BEC cold atomic gases [10,11,89]. At large detunings (above 1 GHz) to red from the Rydberg state we observed excitation dynamics to the Rydberg state that are inconsistent with a model for non-interacting atoms. Moreover a saturation behavior of the maximum density of Rydberg atoms was extrapolated from the data, with a constant saturated density over a wide range of experimental parameters. A characteristic time scale for the excitation process was extracted, and found to depend on all experimentally accessible parameters (Rabi frequency, detuning, atomic density and principal quantum number). In particular the dynamics became faster when the atomic density was

increased, which, combine with the saturation behavior, suggested that many-body excitation dynamics took place. The characteristic time scale also depended on the Rydberg state that was chosen in the experiment, which hinted at the crucial influence of interactions involving Rydberg atoms. The experimental data was analyzed by evaluating power law scaling behavior of the characteristic time scale on all relevant experimental parameters independently.

In order to understand these experimental results, a theoretical model for the aggregation of Rydberg excitations was introduced [19, 20]. The idea of this model is that when Rydberg atoms are excited off-resonantly and that there is strong dephasing noise, the interaction from a Rydberg atom onto the Rydberg states of surrounding atoms shifts these Rydberg states towards resonance with the laser. It results in a strongly facilitated excitation of Rydberg atoms at a specific distance which depends on the interaction potential and the detuning. The subsequent excitations therefore happen inside a "resonant shell" at a fixed distance from already excited Rydberg atoms, such that the excitations are spatially correlated. The large dephasing noise controls the width of the "resonant shell", ensuring that there are indeed atoms for which the excitation is facilitated. Formally the large dephasing noise allows for a reduction of the equation governing the excitation of an ensemble of atoms in these conditions to a master equation for an ensemble of classical quasi spin-1/2 particles.

The crucial parameters for the theoretical model could be extracted from the experiment. In particular the large dephasing noise in the experiment was attributed to the thermal atomic motion as a combination of Doppler broadening and transit-time broadening. The interaction potentials were extracted directly from the saturated density of Rydberg atoms. Using a kinetic Monte-Carlo algorithm simulations of the model were performed for the parameters of the experiment, and two simplified implementations of the interaction potentials. The resulting excitation dynamics showed a similar shape to what was observed experimentally. As for the experimental data a characteristic time scale for the excitation dynamics was extracted from the simulation, which revealed power law scaling behaviors as a function of the experimental parameters. The power law exponents were in very good agreement with those of the experimental data. Furthermore the characteristic time scales of the experiment and the simulations were similar in absolute value, which in combination with the power laws demonstrated that the excitation dynamics observed in the experiment is indeed facilitated excitation.

There were significant fundamental differences between the experimental situation and the theoretical model, such as the considerable simplification of the interaction potentials in the model. Furthermore the ensemble of atoms in the model were a frozen gas. The consequences of the atomic motion being crucial in the experiment are two-fold. First, as mentioned before, the dephasing mechanism is complex and inhomogeneous. Second the spatial correlations only exist for very short time intervals. Yet the agreement between the experimental results and the simulation results are very good, which is a testimony of the robustness of the underlying physics. In other words the only requirement for facilitated excitation and the formation of aggregates are (i) that there is some interaction potential, and (ii) that the dephasing noise (whatever its nature) is strong. Overall it is remarkable that strong interaction effects and collective excitation

dynamics of Rydberg atoms can be observed in the rather "dirty" environment. This is promising for future work in our group focusing on making use of the interaction between Rydberg atoms for the realization of a single-photon source.

Outlook

The spatial correlations resulting from the facilitated excitation (see Figure 4.6(c)) draw comparisons between Rydberg aggregation and soft-matter system. Since the motion of the atoms is so prominent in our experiment however, it is not possible for us to observe the short-range order. One way to make use of the spatially correlated excitation would be to imprint extrinsically some spatial order and study how the excitation dynamics are modified. In practice this could be realized by having one of the excitation laser to be either in a 3D-lattice configuration, or in a 2D array of addressed spots [90]. In such a configuration the excitation of Rydberg atoms can only happen at specific positions in space. Facilitated excitation in such a system can only happen if its characteristic distance matches the distance of the imprinted order, and thus probes the ordered structure imprinted by the laser. Because of the atomic motion in a thermal gas, the atoms would continuously fly through spots where they can be excited, hence inducing a competition of time scales between the excitation rate and the motional decay rate through the spots. A theoretical study in this conditions showed promising possibilities for the observation and study of non-equilibrium phase transitions [21].

A second potential application of these results is the probing of local interactions between Rydberg atoms and their environment because the aggregation is so dependent on the interaction potentials. If the excitation is performed close to a surface and that the surface interacts with the Rydberg atoms there will be instantaneous facilitated excitation close to the surface, thus removing the need for slow off-resonant excitation. The excitation signal would be greatly altered by the surface, which could be used to characterize the interaction between Rydberg atoms and the surface.

Modulation of Rydberg states

The second experiment presented in this thesis consisted in the modulation of the amplitude of a transmitted light field. Cesium atoms in a vapor cell were excited to a Rydberg state with a two-photon excitation scheme. The vapor cell was placed inside the electric field produced by a pair of electrodes. A radio frequency signal was applied to the electrode to create the potential difference. The electrodes were positioned on a printed circuit board designed using high frequency technologies, which is crucial to ensure impedance matching along the transmission line and paves the way for a possible future miniaturization and integration of the system.

A heterodyne measurement technique was used to improve the sensitivity to amplitude modulations of the light field that are small and at high frequencies (several GHz). A second light field with a frequency offset close the modulation frequency was sent at the same time to the photodetector, whose bandwidth was smaller than the modulation frequency but which offered a large gain. The mixing of the two light fields by the measurement of the intensity converted the frequency of the modulation signal to a value detectable by the detector.

The goal was to reach modulation frequencies as high as possible. We were able to observe modulation of the light field up to a frequency of the electric field of 3.6 GHz. Because of the quadratic Stark shift this means that the side bands on the light field were actually at frequencies up to 7.2 GHz. This maximum frequency roughly corresponds to the bandwidth of all the electronic elements involved in the measurement, and is thus an absolute limit for the current setup.

Simulations were performed for three-level atoms and a periodic energy shift of the Rydberg state. The results of the simulations could be characterized using the framework of the Floquet theory, in which the atomic levels are dressed by the oscillating field. The comparison of the experimental results to the simulations yielded only some limited qualitative agreement and understanding. In particular the amplitude of the modulation signal is expected to be much larger. Moreover the distortions of the experimental modulation signal suggests that interaction effects might play a role and calls for further investigation.

Outlook

As the modulation frequency reached the technical limits of the detection method, we have not discovered any fundamental frequency limitations for this scheme. In order to reach higher modulation frequencies, several technical barriers need to be lifted. First, a detailed understanding of geometry effects for the PCB and the electrodes is necessary. Especially the resonance at 4.8 GHz needs to be understood and the design modified as to push it to larger frequencies. There a miniaturization of the cell might be necessary. Performing the experiment in a hollow-core fiber would also be an option [87, 91]. The other barrier is in the detection scheme. The maximum

frequency offset allowed by the digital phase lock was reached. In order to detect higher modulation frequencies a new scheme needs to be implemented. A possible solution would be to use a cascade of several phase locked lasers. As for the generation of the oscillating electric field, the fundamental limit in the current setup is set by the RF amplifier, which has a bandwidth of 4.5 GHz. The amplifier was required in order to reach 1 W of power. For the same Stark shift, higher lying Rydberg state would require less power because of their increased polarizability. However one would also need to ensure that no disturbing interaction effects perturb the measurement. Finally the influence of charges in vapor cells with Rydberg atoms has to be further understood, as electrons are strongly influenced by oscillating electric fields.

Erklärung

Hiermit erkläre ich, dass ich diese Arbeit selbständig verfasst und keine anderen als die von mir angegebenen Quellen und Hilfsmittel verwendet habe.

Stuttgart, 21. März 2016

Alban Urvoy

Bibliography

[1] Abrikosov, A.A., Nobel Lecture: Type-II superconductors and the vortex lattice, *Reviews of Modern Physics* **76**, 975–979 (2004).

[2] Sachdev, S., Quantum magnetism and criticality, *Nature Physics* **4**, 173–185 (2008).

[3] Binder, K. and Kob, W., *Glassy Materials and Disordered Solids (World Scientific)*, World Scientific, Singapore (2011).

[4] Bloch, I. and Zwerger, W., Many-body physics with ultracold gases, *Reviews of Modern Physics* **80**, 885–964 (2008).

[5] Islam, R., Senko, C., Campbell, W.C., Korenblit, S., Smith, J., Lee, A., Edwards, E.E., Wang, C.C.J., Freericks, J.K., and Monroe, C., Emergence and frustration of magnetism with variable-range interactions in a quantum simulator., *Science (New York, N.Y.)* **340**, 583–7 (2013).

[6] Madison, K., Chevy, F., Wohlleben, W., and Dalibard, J., Vortex formation in a stirred bose-einstein condensate, *Physical review letters* **84**, 806–9 (2000).

[7] Hadzibabic, Z., Krüger, P., Cheneau, M., Battelier, B., and Dalibard, J., Berezinskii-Kosterlitz-Thouless crossover in a trapped atomic gas., *Nature* **441**, 1118–21 (2006).

[8] Schauß, P., Cheneau, M., Endres, M., Fukuhara, T., Hild, S., Omran, A., Pohl, T., Gross, C., Kuhr, S., and Bloch, I., Observation of spatially ordered structures in a two-dimensional Rydberg gas, *Nature* **491**, 87–91 (2012).

[9] Labuhn, H., Barredo, D., Ravets, S., de Léséleuc, S., Macrì, T., Lahaye, T., and Browaeys, A., A highly-tunable quantum simulator of spin systems using two-dimensional arrays of single Rydberg atoms, *arXiv:1509.04543* (2015).

[10] Schempp, H., Günter, G., Robert-De-Saint-Vincent, M., Hofmann, C.S., Breyel, D., Komnik, A., Schönleber, D.W., Gärttner, M., Evers, J., Whitlock, S., and Weidemüller, M., Full counting statistics of laser excited Rydberg aggregates in a one-dimensional geometry, *Physical Review Letters* **112**, 013002 (2014).

[11] Malossi, N., Valado, M.M., Scotto, S., Huillery, P., Pillet, P., Ciampini, D., Arimondo, E., and Morsch, O., Full counting statistics and phase diagram of a dissipative rydberg gas, *Physical Review Letters* **113**, 023006 (2014).

[12] Lesanovsky, I. and Garrahan, J.P., Kinetic constraints, hierarchical relaxation, and onset of glassiness in strongly interacting and dissipative Rydberg gases., *Physical review letters* **111**, 215305 (2013).

[13] Huber, B., Baluktsian, T., Schlagmüller, M., Kölle, A., Kübler, H., Löw, R., and Pfau, T., GHz Rabi flopping to Rydberg states in hot atomic vapor cells, *Physical Review Letters* **107**, 243001 (2011).

[14] Baluktsian, T., Urban, C., Bublat, T., Giessen, H., Löw, R., and Pfau, T., Fabrication method for microscopic vapor cells for alkali atoms., *Optics letters* **35**, 1950–2 (2010).

[15] Huber, B., Kölle, A., and Pfau, T., Motion-induced signal revival in pulsed Rydberg four-wave mixing beyond the frozen-gas limit, *Physical Review A* **90**, 053806 (2014).

[16] Chen, Y.H., Ripka, F., Löw, R., and Pfau, T., Pulsed Rydberg four-wave mixing with motion-induced dephasing in a thermal vapor, *Applied Physics B* **122**, 18 (2016).

[17] Baluktsian, T., Huber, B., Löw, R., and Pfau, T., Evidence for strong van der Waals type Rydberg-Rydberg interaction in a thermal vapor, *Physical Review Letters* **110**, 123001 (2013).

[18] Demtröder, W., *Laser Spectroscopy: Vol. 1: Basic Principles*, Laser Spectroscopy, Springer Berlin Heidelberg (2008).

[19] Lesanovsky, I. and Garrahan, J.P., Out-of-equilibrium structures in strongly interacting Rydberg gases with dissipation, *Physical Review A - Atomic, Molecular, and Optical Physics* **90**, 011603(R) (2014).

[20] Marcuzzi, M., Schick, J., Olmos, B., and Lesanovsky, I., Effective dynamics of strongly dissipative Rydberg gases, *Journal of Physics A: Mathematical and Theoretical* **47**, 482001 (2014).

[21] Everest, B., Marcuzzi, M., and Lesanovsky, I., Atomic loss and gain as a resource for nonequilibrium phase transitions in optical lattices, *Physical Review A* **93**, 023409 (2016).

[22] Monz, T., Schindler, P., Barreiro, J.T., Chwalla, M., Nigg, D., Coish, W.A., Harlander, M., Hänsel, W., Hennrich, M., and Blatt, R., 14-Qubit entanglement: creation and coherence., *Physical Review Letters* **106**, 130506 (2011).

[23] Saffman, M., Walker, T.G., and Mølmer, K., Quantum information with Rydberg atoms, *Reviews of Modern Physics* **82**, 2313–2363 (2010).

[24] Gaëtan, A., Miroshnychenko, Y., Wilk, T., Chotia, A., Viteau, M., Comparat, D., Pillet, P., Browaeys, A., and Grangier, P., Observation of collective excitation of two individual atoms in the Rydberg blockade regime, *Nature Physics* **5**, 115–118 (2009).

[25] Weimer, H., Löw, R., Pfau, T., and Büchler, H.P., Quantum Critical Behavior in Strongly Interacting Rydberg Gases, *Physical Review Letters* **101**, 250601 (2008).

[26] Weimer, H., Müller, M., Lesanovsky, I., Zoller, P., and Büchler, H.P., A Rydberg quantum simulator, *Nature Physics* **6**, 382 – 388 (2010).

[27] Carr, C., Ritter, R., Wade, C.G., Adams, C.S., and Weatherill, K.J., Nonequilibrium phase transition in a dilute rydberg ensemble, *Physical Review Letters* **111**, 113901 (2013).

[28] Urvoy, A., Ripka, F., Lesanovsky, I., Booth, D., Shaffer, J.P., Pfau, T., and Löw, R., Strongly correlated growth of Rydberg aggregates in a vapour cell, *Physical Review Letters* **114**, 203002 (2015).

[29] Sedlacek, J.A., Schwettmann, A., Kübler, H., Löw, R., Pfau, T., and Shaffer, J.P., Microwave electrometry with Rydberg atoms in a vapour cell using bright atomic resonances, *Nature Physics* **8**, 819–824 (2012).

[30] Anderson, D., Miller, S., Raithel, G., Gordon, J., Butler, M., and Holloway, C., Optical Measurements of Strong Microwave Fields with Rydberg Atoms in a Vapor Cell, *Physical Review Applied* **5**, 034003 (2016).

[31] Miller, S.A., Anderson, D.A., and Raithel, G., Radio-frequency-modulated Rydberg states in a vapor cell, *arXiv:1601.06840* (2016).

[32] Kübler, H., Shaffer, J.P., Baluktsian, T., Löw, R., and Pfau, T., Coherent Excitation of Rydberg Atoms in Thermal Vapor Microcells, *Nature Photonics* **4**, 112 (2010).

[33] Gallagher, T.F., Rydberg atoms, *Reports on Progress in Physics* **51**, 143–188 (1988).

[34] Lorenzen, C.J. and Niemax, K., Precise quantum defects of nS, nP and nD Levels in Cs I, *Zeitschrift für Physik A Atoms and Nuclei* **133**, 127–133 (1984).

[35] Butscher, B., *A Rydberg Interferometer: From coherent formation of ultralong-range Rydberg Molecules to state tomography of Rydberg atoms*, PhD Thesis, Universität Stuttgart (2011).

[36] Vasilyev, A.A., Savukov, I.M., Safronova, M.S., and Berry, H.G., Measurement of the $6s$-$7p$ transition probabilities in atomic cesium and a revised value for the weak charge Q_W, *Physical Review A* **66**, 020101 (2002).

[37] Gallagher, T.F., *Rydberg atoms*, volume 51 of *Cambridge Monographs on Atomic, Molecular and Chemical Physics*, Cambridge University Press (1999).

[38] Flannery, M.R., Vrinceanu, D., and Ostrovsky, V.N., Long-range interaction between polar Rydberg atoms, *Journal of Physics B: Atomic, Molecular and Optical Physics* **38**, S279–S293 (2005).

[39] Singer, K., Stanojevic, J., Weidemüller, M., and Côté, R., Long-range interactions between alkali Rydberg atom pairs correlated to the ns-ns, $np$$np$ and nd-nd asymptotes, *Journal of Physics B: Atomic, Molecular and Optical Physics* **38**, S295–S307 (2005).

[40] Le Roy, R.J., Long-Range Potential Coefficients From RKR Turning Points: C_6 and C_8 for $B(3\Pi_{Ou}{}^+)$-State Cl_2, Br_2, and I_2, *Canadian Journal of Physics* **52**, 246–256 (1974).

[41] Reinhard, A., Liebisch, T.C., Knuffman, B., and Raithel, G., Level shifts of rubidium Rydberg states due to binary interactions, *Physical Review A* **75**, 032712 (2007).

[42] Béguin, L., Vernier, A., Chicireanu, R., Lahaye, T., and Browaeys, A., Direct Measurement of the van der Waals Interaction between Two Rydberg Atoms, *Physical Review Letters* **110**, 263201 (2013).

[43] Ravets, S., Labuhn, H., Barredo, D., Béguin, L., Lahaye, T., and Browaeys, A., Coherent dipole-dipole coupling between two single Rydberg atoms at an electrically-tuned Förster resonance, *Nature Physics* **10**, 914–917 (2014).

[44] Deiglmayr, J., Saßmannshausen, H., Pillet, P., and Merkt, F., Observation of dipole-quadrupole interaction in an ultracold gas of Rydberg atoms., *Physical review letters* **113**, 193001 (2014).

[45] Schwettmann, A., Crawford, J., Overstreet, K.R., and Shaffer, J.P., Cold Cs Rydberg-gas interactions, *Physical Review A* **74**, 020701 (2006).

[46] Claude Cohen-Tannoudji, Dupont-Roc, J., and Grynberg, G., *Atom-Photon Interactions*, John Wiley & Sons, Inc. (2004).

[47] Foot, C.J., *Atomic Physics*, Oxford Master Series in Physics, Oxford University Press (2004).

[48] Baluktsian, T., *Rydberg interaction between thermal atoms: Van der Waals-type Rydberg-Rydberg interaction in a vapor cell experiment*, PhD Thesis, Universität Stuttgart (2013).

[49] Huber, B., *Coherent Rydberg dynamics and interaction above room temperature: The frozen gas regime and beyond*, PhD Thesis, Universität Stuttgart (2014).

[50] Molmer, K., Castin, Y., and Dalibard, J., Monte Carlo wave-function method in quantum optics, *Journal of the Optical Society of America B* **10**, 524–538 (1993).

[51] Lindblad, G., On the generators of quantum dynamical semigroups, *Communications in Mathematical Physics* **48**, 119–130 (1976).

[52] Reiter, F. and Sørensen, A.S., Effective operator formalism for open quantum systems, *Physical Review A* **85**, 032111 (2012).

[53] Brion, E., Pedersen, L.H., and Mølmer, K., Adiabatic elimination in a lambda system, *Journal of Physics A: Mathematical and Theoretical* **40**, 1033–1043 (2007).

[54] Fewell, M., Adiabatic elimination, the rotating-wave approximation and two-photon transitions, *Optics Communications* **253**, 125–137 (2005).

[55] Paulisch, V., Rui, H., Ng, H.K., and Englert, B.G., Beyond adiabatic elimination: A hierarchy of approximations for multi-photon processes, *The European Physical Journal Plus* **129**, 12 (2014).

[56] Sagle, J., Namiotka, R.K., and Huennekens, J., Measurement and modelling of intensity dependent absorption and transit relaxation on the cesium line, *Journal of Physics B: Atomic, Molecular and Optical Physics* **29**, 2629–2643 (1999).

[57] Urvoy, A., *Set-up of a laser system for precision spectroscopy of highly excited caesium atoms*, Diploma Thesis, Universität Stuttgart (2011).

[58] Kleiner, T., *Aufbau und Charakterisierung einer Pockelszelle zur Erzeugung kurzer Lichtpulse*, Bachelor Thesis, Universität Stuttgart (2011).

[59] Steck, D.A. *Cesium D Line Data.* available online at `http://http://steck.us/alkalidata/` (revision 2.1.4, 23 December 2010)).

[60] Ripka, F., *Time-resolved coherent excitation dynamics of Rydberg states in thermal vapors*, Master Thesis, Universität Stuttgart (2013).

[61] Kübler, H., *Kohärente Rydberg-Spektroskopie in einer Rubidium Mikrozelle*, PhD Thesis, Universität Stuttgart (2012).

[62] Bakos, J., AC stark effect and multiphoton processes in atoms, *Physics Reports* **31**, 209–235 (1977).

[63] Grimm, R., Weidemüller, M., and Ovchinnikov, Y.B., Optical Dipole Traps for Neutral Atoms, *Advances In Atomic, Molecular, and Optical Physics* **42**, 95–170 (2000).

[64] Siddons, P., Adams, C.S., Ge, C., and Hughes, I.G., Absolute absorption on rubidium D lines: comparison between theory and experiment, *Journal of Physics B: Atomic, Molecular and Optical Physics* **41**, 155004 (2008).

[65] Weller, L., Bettles, R.J., Siddons, P., Adams, C.S., and Hughes, I.G., Absolute absorption on the rubidium D1 line including resonant dipole-dipole interactions., *Journal of Physics B: Atomic, Molecular and Optical Physics* **44**, 195006 (2011).

[66] Gärttner, M., *Many-Body Effects in Rydberg Gases - Coherent Dynamics of Strongly Interacting Two-Level Atoms and Nonlinear Optical Response of a Rydberg Gas in EIT Configuration*, PhD Thesis, Universität Heidelberg (2013).

[67] Pohl, T., Demler, E., and Lukin, M.D., Dynamical Crystallization in the Dipole Blockade of Ultracold Atoms, *Physical Review Letters* **104**, 043002 (2010).

[68] Cinti, F., Jain, P., Boninsegni, M., Micheli, A., Zoller, P., and Pupillo, G., Supersolid droplet crystal in a dipole-blockaded gas, *Physical Review Letters* **105**, 135301 (2010).

[69] van Bijnen, R.M.W., Smit, S., van Leeuwen, K.A.H., Vredenbregt, E.J.D., and Kokkelmans, S.J.J.M.F., Adiabatic formation of Rydberg crystals with chirped laser pulses, *Journal of Physics B: Atomic, Molecular and Optical Physics* **44**, 184008 (2011).

[70] Schauß, P., Zeiher, J., Fukuhara, T., Hild, S., Cheneau, M., Macrì, T., Pohl, T., Bloch, I., and Gross, C., Crystallization in Ising quantum magnets, *Science* **347**, 1455–1458 (2015).

[71] Barredo, D., Kübler, H., Daschner, R., Löw, R., and Pfau, T., Electrical readout for coherent phenomena involving Rydberg atoms in thermal vapor cells, *Physical Review Letters* **110**, 123002 (2013).

[72] Vitrant, G., Raimond, J.M., Gross, M., and Haroche, S., Rydberg to plasma evolution in a dense gas of very excited atoms, *Journal of Physics B: Atomic and Molecular Physics* **15**, L49–L55 (1982).

[73] Robert-de Saint-Vincent, M., Hofmann, C.S., Schempp, H., Günter, G., Whitlock, S., and Weidemüller, M., Spontaneous avalanche ionization of a strongly blockaded Rydberg gas., *Physical review letters* **110**, 045004 (2013).

[74] Simonelli, C., Valado, M.M., Masella, G., Asteria, L., Arimondo, E., Ciampini, D., and Morsch, O., Seeded excitation avalanches in off-resonantly driven Rydberg gases, *arXiv:1602.01257* (2016).

[75] Fan, H., Kumar, S., Sedlacek, J., Kübler, H., Karimkashi, S., and Shaffer, J.P., Atom based RF electric field sensing, *Journal of Physics B: Atomic, Molecular and Optical Physics* **48**, 202001 (2015).

[76] Mohapatra, A.K., Jackson, T.R., and Adams, C.S., Coherent Optical Detection of Highly Excited Rydberg States Using Electromagnetically Induced Transparency, *Physical Review Letters* **98**, 113003 (2007).

[77] Anderson, S.E., Younge, K.C., and Raithel, G., Trapping Rydberg atoms in an optical lattice., *Physical review letters* **107**, 263001 (2011).

[78] Yudin, V.I., Taichenachev, A.V., and Basalaev, M.Y., Dynamic steady state of periodically driven quantum systems, *Physical Review A* **93**, 013820 (2016).

[79] Tanasittikosol, M., *Rydberg dark states in external fields*, PhD Thesis, University of Durham (2011).

[80] Shirley, J.H., Solution of the Schrödinger Equation with a Hamiltonian Periodic in Time, *Physical Review* **138**, B979–B987 (1965).

[81] Barone, S.R., Narcowich, M.A., and Narcowich, F.J., Floquet theory and applications, *Physical Review A* **15**, 1109–1125 (1977).

[82] Son, S.K., Han, S., and Chu, S.I., Floquet formulation for the investigation of multiphoton quantum interference in a superconducting qubit driven by a strong ac field, *Physical Review A* **79**, 032301 (2009).

[83] Pozar, D.M., *Microwave Engineering*, John Wiley & Sons, Inc. (2012), Fourth edition.

[84] Wheeler, H.A., Transmission-Line Properties of a Strip on a Dielectric Sheet on a Plane, *IEEE Transactions on Microwave Theory and Techniques* **25**, 631–647 (1977).

[85] Appel, J., MacRae, A., and Lvovsky, A.I., A versatile digital GHz phase lock for external cavity diode lasers, *Measurement Science and Technology* **20**, 055302 (2009).

[86] de Melo, N.R., Wade, C.G., Sibalic, N., Kondo, J.M., Adams, C.S., and Weatherill, K.J., Intrinsic Optical Bistability in a Strongly-Driven Rydberg Ensemble, *arXiv:1603.01449* (2016).

[87] Epple, G., Kleinbach, K.S., Euser, T.G., Joly, N.Y., Pfau, T., Russell, P.S.J., and Löw, R., Rydberg atoms in hollow-core photonic crystal fibres., *Nature communications* **5**, 4132 (2014).

[88] Raimond, J.M., Vitrant, G., and Haroche, S., Spectral line broadening due to the interaction between very excited atoms: 'the dense Rydberg gas', *Journal of Physics B: Atomic and Molecular Physics* **14**, L655–L660 (1981).

[89] Heidemann, R., Raitzsch, U., Bendkowsky, V., Butscher, B., Löw, R., Santos, L., and Pfau, T., Evidence for Coherent Collective Rydberg Excitation in the Strong Blockade Regime, *Physical Review Letters* **99**, 163601 (2007).

[90] Nogrette, F., Labuhn, H., Ravets, S., Barredo, D., Béguin, L., Vernier, A., Lahaye, T., and Browaeys, A., Single-Atom Trapping in Holographic 2D Arrays of Microtraps with Arbitrary Geometries, *Physical Review X* **4**, 021034 (2014).

[91] Veit, C., *Rf Dressing of Rydberg States in Hollow-Core Fibers*, Master Thesis, Universität Stuttgart (2015).

Danksagung

An dieser Stelle möchte ich mir noch bei ein paar Leuten für den Verlauf, das Vertrauen und die Unterstützung bedanken. Alles davon hat dazu geführt, dass diese Doktorarbeit eine großartige Erfahrung war.

Zunächst möchte ich mich bei Tilman Pfau bedanken. Durch deine freundliche Betreuung entsteht eine super Arbeitsatmosphäre am Institut. Bemerkenswert ist auch die erstklassige Ausstattung, welche die Laborarbeit stark vereinfacht, sowie der große Wert, den du auf Langzeitperspektiven legst.

Herrn Prof. Peter Michler danke ich für die freundliche Übernahme des Mitberichts, und Frau Prof. Daghofer für die freundliche Übernahme des Prüfungsvorsitzes.

Mein besonderer Dank geht an Robert Löw. Direkt nachdem ich in Stuttgart angekommen bin, saß ich in deiner Vorlesung "Fortgeschrittene Atomphysik", und es hat mein Interesse an der Atomphysik geweckt. Dank deiner entspannten Betreuung und deinem Vertrauen seit fast 6 Jahren, hat es mir sehr viel Spaß gemacht, die Geheimnisse der wechselwirkende Zäsium Atome zu lüften. Auch vielen Dank für das zügige Korrekturlesen.

Im Laufe dieser vielen Jahren habe ich die Möglicheit gehabt, mit vielen guten Physikern direkt arbeiten zu dürfen. Als erster Fabian Ripka, der mit mir als Masterstudent während dem wichtigsten Teil im Labor (der Kampf um das Verständnis!) gearbeitet hat und bei vielen Ergebnissen in dieser Arbeit eine große Rolle gespielt hat. Vielen Dank für dein Engagement und die interessanten Diskussionen. Auch Christian Veit und Andy Rico haben mitgemacht. Es war mir eine Ehre und es hat Spaß gemacht, mit euch zu arbeiten. Viel Erfolg euch dreien für das Weitere! Ein großer Dank geht an Igor Lesanovsky. Dein Input hat es ermöglicht, unsere Daten endlich zu verstehen. Vielen Dank dafür und für die zahlreiche nette und bereichernde Diskussionen. Ich durfte auch an einem Projekt mit Chris Carr und Ralf Ritter arbeiten. Vielen Dank für die gute Stimmung bei der Zusammenarbeit.

Im "dritten Stock" hat zwar jeder sein eigenes Projekt, allerdings gibt es viel Kooperation und eine entspannte Arbeitsatmosphäre, die dafür sorgen, dass wir das "MicCell" Team sind. Insbesondere ist Harald Kübler zu danken. Deine stetige Hilfsbereitschaft und gute Laune sind einfach großartig. Vielen Dank auch für das Korrekturlesen von dieser Arbeit. Vielen Dank auch an alle anderen "MicCell" Kameraden: Balu, Bernhard, Andi, Paul, Georg, Daniel B., Daniel W., Renate, Johannes, Marga, Michael (die Liste ist nicht vollständig!). Ich bin froh, so viel von euch gelernt zu haben!

Vielen Dank an das gesamte PI5 für die tolle Stimmung und die außergewöhnliche Hilfsbereitschaft. Das Verwaltungspersonal bekommt auch ein großes Danke von mir:

Beatrice, Karin O., Karin H., Astrid, Oliver, Nadine, Susan, Katrin. Ihr macht unser Leben einfach durch die Übernahme von des Kontakts mit der Uni-Verwaltung, wie zum Beispiel bei Dientreiseabrechnungen.

Abschließend möchte ich mich bei meinen Freunden für deren Unterstützung bedanken und für die Möglichkeit, an etwas anderes als Physik zu denken. Und natürlich geht mein größtes “Danke!” an meine Familie, deren Unterstützung alles ermöglicht hat.